Topics in Geophysical Fluid Dynamics

by

Jared P. Whitehead

A dissertation submitted in partial fulfillment
of the requirements for the degree of
Doctor of Philosophy
(Applied and Interdisciplinary Mathematics)
in The University of Michigan
2012

Doctoral Committee:

Professor Charles R. Doering, Co-chair
Professor Richard B. Rood, Co-chair
Professor Jeffrey B. Rauch
Associate Professor Divakar Viswanath
Assistant Professor Christiane Jablonowski

To Samantha, Joshua, Abby, and Bree

ACKNOWLEDGEMENTS

The saying goes that raising a child takes an entire village. There should be a similar statement for an individual seeking a PhD. There are many who I owe thanks to, and will likely forget to mention. First and foremost I need to thank my wife Samantha for being there when I really needed it. I would like to thank some of the fellow Math department students I associated with over the past few years: Matt Elsey, Ashley (Selegue) Holland, Pete Bossler, and many others as well as those from AOSS, Physics, and other various and sundry departments. A special thanks to James Kent, Benson Muite and Evelyn Lunasin for listening to my crazy ideas on occasion and critiquing me when necessary. My gratitude would be incomplete without thanking the many professors I had opportunity to take courses from while in Ann Arbor, as well as those who were willing to talk with me outside of the classroom including Joel Smoller, Smadar Karni, Marc Perlin, Divakar Viswanath, and Peter van Keken. I owe a special thanks to Jeffrey Rauch who through many conversations, pointed me in the direction where most of my results came from. I would like to thank Christiane Jablonowski for her many suggestions, guidance and instruction. Lastly I would like to thank Ricky Rood and Charlie Doering for their willingness to take a chance on me as an unproven beginning student, and for their careful tutelage and instruction.

TABLE OF CONTENTS

LIST OF FIGURES

Figure

LIST OF APPENDICES

Appendix

CHAPTER I

Introduction

From stirring cream into a cup of coffee, to the global circulation of the atmosphere and the transport of heat by the earth's oceans, the motion of fluids play a fundamental role in modern society. The accurate representation and study of the dynamical properties of fluid flow is an active area of research in many scientific fields. In most cases the interesting dynamics occur when the flow is turbulent, i.e., chaotic particle trajectories and small scale eddies develop simultaneously with the large scale structure of the flow. In addition to the mathematically relevant question of regularity to the Navier-Stokes equations thought to describe fluid flow (see Fefferman (2002)), turbulence presents a host of unanswered questions to the scientific community. Some of these issues are fundamental, i.e., how to measure the transport of various quantities by the fluid, and some are applicable to policy considerations such as the effect of various pollutants on the atmospheric circulation and weather patterns in a regional area.

Studies of turbulence have led to advances in statistics, probabilistic methods, variational calculus, asymptotic methods, and significant developments in numerical analysis. Each of these tools is used to comprehend the nature of the partial differential equations that model fluid flow. In addition to these mathematical tools,

physicists and engineers have performed careful experiments to measure different properties of a fluid and its flow. The careful scientist considers results of these experiments as well as developments provided by the mathematical constructs listed above before drawing any conclusions about the nature of turbulence. It is for this reason that fluid dynamics is by nature an interdisciplinary subject, creating the need for open communication across often opaque barriers in academic circles.

The study of a fluid constrained to a rotating sphere is referred to as geophysical fluid dynamics. This situation is of particular interest for applications in oceanography, atmospheric and the meteorological sciences, dynamics of the earth's mantle, and planetary astrophysics. The effect of adding rotation to the equations of motion generically leads to a stratified vertical density profile for the fluid. In some circumstances this effectively reduces the dimension of the large scale flow from three to two (see Pedlosky (1987); Holton (2004)). While this and other simplifying assumptions are acceptable for large scale circulations in the atmosphere and oceans, there is little guidance for accurately representing the effect of smaller scales on these assumptions and their impact on large scale structures (see Ottino (1989) for a discussion on the effects of mixing at small scales and Andrews and McIntyre (1978) for a proposed theory to quantify this scale interaction).

Constructing a model meant to simulate the dynamic evolution of the earth's climate requires maintaining a delicate balance between finite computational resources and the need to resolve and understand the interactions of the fluid at varying scales. For instance, some waves in the atmosphere may be on scales as small as meters and vary temporally in seconds while affecting the general circulation and climate of the globe considered over hundreds of years. Modern computational architectures are centuries away from resolving all of these scales, and so simplifying assumptions are

required. Even with reasonable reduced models such as the hydrostatically balanced assumption, sub-grid and unresolved scales affect the 'big picture' results. This means that the model must model (parameterize) these scales to capture their effects. These small scale structures cascade to scales below that of the grid resolution, building up energy at unresolved scales, leading to dynamical and numerical instabilities. Dissipation is needed to remove these small scales before such instabilities develop.

Therefore as climate models continue to evolve it is essential to keep in mind numerical considerations, accuracy of asymptotic and simplifying assumptions on large-scale flow, and results from turbulence theory. Without a fundamental grasp on the underlying advances in turbulence, adequate modeling of the sub-grid processes will be retarded unnecessarily. This thesis contributes to both the small and large picture aspects of this problem. In Chapters II,III, and IV we consider the fundamentally important problem of convective turbulence and estimates on the transport of heat in idealized situations. Chapters V, and VI directly address some of the numerical dissipative processes in some of the current General Circulation Models (GCM) built to model the dynamics of earth's atmosphere, in an effort to quantify the effects of added dissipation on the model's output.

1.1 Convection

The simplest description of convection is simply the familiar notion that 'hot air rises'. Heating a fluid from below puts less dense warm fluid below a dense cool fluid, an unstable stratification. When the temperature difference is significant the buoyancy induces turbulent motion. This situation appears in the earth's atmosphere, predominantly in the boundary layer near the surface of the planet, but in

concert with the effects of moisture, can be the dominating force for vertical mixing and transport in meteorological scales of significant importance to climate (see Emmanuel (1994)). The mathematical treatment of natural convection was pioneered by Lord Rayleigh in Rayleigh (1916). The fluid is contained in a horizontally periodic box constrained between two plates h units apart with appropriate boundary conditions at the top and bottom. Using the Boussinesq approximation, i.e., density variations appear only in the buoyancy term, the partial differential equations governing the Rayleigh-Bénard system are given by

$$\frac{\partial \boldsymbol{u}}{\partial t} + \boldsymbol{u} \cdot \nabla \boldsymbol{u} + \frac{1}{\rho}\nabla p = \nu \Delta \boldsymbol{u} + g\alpha \mathrm{T} \tag{1.1}$$

$$\nabla \cdot \boldsymbol{u} = 0 \tag{1.2}$$

$$\frac{\partial \mathrm{T}}{\partial t} + \boldsymbol{u} \cdot \nabla \mathrm{T} = \kappa \Delta \mathrm{T} \tag{1.3}$$

with specified initial data and appropriate boundary conditions in the vertical. The dynamic variables are the velocity vector field $\boldsymbol{u}$, temperature T, and pressure p. ρ is the mean density, ν the kinematic viscosity, g the gravitational force, α the thermal expansion coefficient, and κ the thermal diffusivity. Typically a driving force is added to the system through the boundary conditions, i.e., $\mathrm{T}|_{z=0} = \delta\mathrm{T} + \mathrm{T}|_{z=h}$, although there is interest in other types of forcing as explained in Chapter II.

1.1.1 Stability of the Conductive Solution

In Rayleigh (1916) Rayleigh computes the linear stability of the conductive solution when the heat is conducted via molecular diffusion from the bottom to the top plate. Rayleigh shows that for 2 dimensional convection with stress-free boundaries (see Chapter III for more details regarding this situation) the purely conductive solution $\mathrm{T}(x, y, z, t) = \mathrm{T}|_{z=h} + \delta\mathrm{T}\left(1 - \frac{z}{h}\right)$ is stable so long as $\frac{g\alpha\delta T h^3}{\nu\kappa}$ is less than some critical value. This non-dimensional combination of parameters has since become

known as the Rayleigh number Ra, and can be considered a measure of the effective forcing placed on the system via the enforced temperature gradient. The numerical value of the critical Rayleigh number depends on the type of boundary condition specified in the vertical, indicating the dependency of convection on the boundary conditions for laminar flow.

Lord Rayleigh showed that stability of the base conductive state is independent of the Prandtl number $\mathrm{Pr} = \frac{\nu}{\kappa}$. To see how this occurs, consider rescaling (1.1), (1.2), and (1.3) with a temporal scale of $\frac{h^2}{\kappa}$, spatial scale of h, and temperature scale of δT. The non-dimensional set of equations is then

$$\frac{1}{\mathrm{Pr}}\left(\frac{\partial \boldsymbol{u}}{\partial t} + \boldsymbol{u}\cdot\nabla\boldsymbol{u}\right) + \nabla p = \Delta \boldsymbol{u} + \mathrm{RaT} \tag{1.4}$$

$$\nabla \cdot \boldsymbol{u} = 0 \tag{1.5}$$

$$\frac{\partial \mathrm{T}}{\partial t} + \boldsymbol{u}\cdot\nabla\mathrm{T} = \Delta\mathrm{T} \tag{1.6}$$

where now the plates are a unit distance apart and the temperature is given by $\mathrm{T} = 0$ at the top, and $\mathrm{T} = 1$ at the bottom. Linear stability ignores the nonlinear terms, and for a time-independent state such as the conductive profile, also avoids issues arising from the time derivatives of the velocity and temperature. The conductive profile $\mathrm{T}(x, y, z, t) = \tau(z) = 1 - z$ is linearly stable below a specific critical Rayleigh number Ra_c, and linearly unstable for $\mathrm{Ra} > \mathrm{Ra}_c$. Because linear instability is a sufficient condition for instability this indicates that convection sets in for all flows such that $\mathrm{Ra} > \mathrm{Ra}_c$. Energy stability can be used to show that the conductive profile is indeed nonlinearly stable for $\mathrm{Ra} < \mathrm{Ra}_c$, indicating that the only stable solution (regardless of initial data) for these Rayleigh numbers is conduction. It is illustrative to consider the energy stability of the conduction solution.

Let $\theta(x, y, z, t)$ be temperature fluctuations about the conductive state, i.e., $\mathrm{T}(x, y, z, t) =$

$\theta(x,y,z,t)+\tau(z)$ so that (1.6) becomes

$$\frac{\partial\theta}{\partial t}+\boldsymbol{u}\cdot\nabla\theta=\Delta\theta+\tau''-w\tau' \tag{1.7}$$

where $\boldsymbol{u}=(u,v,w)^T$ and $\tau'(z)=\frac{d\tau}{dz}$. Multiplying (1.32) by θ and integrating throughout the entire domain, using the boundary conditions for integrations by parts we see that

$$\frac{d}{dt}\frac{1}{2}\int_V|\theta|^2d\boldsymbol{x} = -\int_V|\nabla\theta|^2d\boldsymbol{x}+\int_V\tau''\theta d\boldsymbol{x}-\int_V\tau' w\theta d\boldsymbol{x} \tag{1.8}$$

$$= -\int_V|\nabla\theta|^2d\boldsymbol{x}+\int_V w\theta d\boldsymbol{x}. \tag{1.9}$$

Similarly multiplying (1.4) by $\boldsymbol{u}$ and integrating we arrive at

$$\frac{d}{dt}\frac{1}{2\,\mathrm{Pr}}\int_V|\boldsymbol{u}|^2d\boldsymbol{x}=-\int_V|\nabla\boldsymbol{u}|^2d\boldsymbol{x}+\mathrm{Ra}\int_V w\theta d\boldsymbol{x}. \tag{1.10}$$

Adding (1.9) and $\frac{1}{\mathrm{Ra}}\times$(1.10) we see that the fluctuations about the conductive state satisfy

(1.11)
$$\frac{d}{dt}\frac{1}{2}\int_V\left[|\theta|^2+\frac{1}{\mathrm{Pr}\,\mathrm{Ra}}|\boldsymbol{u}|^2\right]d\boldsymbol{x}=-\int_V\left[|\nabla\theta|^2+\frac{|\nabla\boldsymbol{u}|^2}{\mathrm{Ra}}-2w\theta\right]d\boldsymbol{x}=-\mathcal{Q}(\boldsymbol{u},\theta).$$

This can be rewritten as

$$\frac{d}{dt}\mathcal{E}=-\left[\frac{\mathcal{Q}}{\mathcal{E}}\right]\mathcal{E} \tag{1.12}$$

so that if we can show that $\mathcal{Q}/\mathcal{E}\geq 0$ for all $\boldsymbol{u}$ and θ satisfying (1.5), $\mathcal{E}(t)$ is a decreasing function of time, implying that $\tau(z)$ is asymptotically and nonlinearly stable. This is called energy stability because we are showing that an 'energy' of the perturbation is decreasing with time.

Verifying that $\mathcal{Q}/\mathcal{E}$ is positive definite can be considered a minimization problem by showing that $\min_{\boldsymbol{u},\theta}[\mathcal{Q}/\mathcal{E}]\geq 0$. Because both $\mathcal{Q}$ and $\mathcal{E}$ are quadratic functionals

of $\boldsymbol{u}$ and θ we will consider this minimization over $\boldsymbol{u}$ and θ such that $\mathcal{E} = 1$ and (1.5) is satisfied, so that we are looking to minimize

$$\mathcal{G}(\boldsymbol{u}, \theta) = \mathcal{Q}(\boldsymbol{u}, \theta) - 2\lambda\mathcal{E}(\boldsymbol{u}, \theta) - \frac{2}{\mathrm{Ra}} \int_V p(\boldsymbol{x}) \nabla \cdot \boldsymbol{u} d\boldsymbol{x} \tag{1.13}$$

where λ and $p(\boldsymbol{x})$ are the Lagrange multipliers enforcing $\mathcal{E} = 1$ and (1.5) respectively. The Euler-Lagrange equations for this problem are

$$-\frac{\lambda}{\mathrm{Pr}\,\mathrm{Ra}}\boldsymbol{u} + \frac{1}{\mathrm{Ra}}\nabla p = \frac{1}{\mathrm{Ra}}\Delta\boldsymbol{u} + \theta\hat{\boldsymbol{k}} \tag{1.14}$$

$$-\lambda\theta - w = \Delta\theta. \tag{1.15}$$

Supposing that we have a velocity field $\boldsymbol{u}$ and temperature fluctuation θ that is the minimizer, we can multiply (1.14) with $\boldsymbol{u}$, and (1.15) with θ and adding the two together and integrating across the domain,

$$-\frac{\lambda}{\mathrm{Pr}\,\mathrm{Ra}} \int_V |\boldsymbol{u}|^2 d\boldsymbol{x} - \lambda \int_V |\theta|^2 d\boldsymbol{x} - \int_V w\theta d\boldsymbol{x} \tag{1.16}$$

$$= -\frac{1}{\mathrm{Ra}} \int_V |\nabla \boldsymbol{u}|^2 d\boldsymbol{x} + \int_V w\theta d\boldsymbol{x} - \int_V |\nabla\theta|^2 d\boldsymbol{x} \tag{1.17}$$

$$\Rightarrow \int_V \left[\frac{1}{\mathrm{Ra}}|\nabla\boldsymbol{u}|^2 + |\nabla\theta|^2 - 2\theta\right] d\boldsymbol{x} = \lambda \int_V \left[\frac{1}{\mathrm{Pr}\,\mathrm{Ra}}|\boldsymbol{u}|^2 + |\theta|^2\right] d\boldsymbol{x}. \tag{1.18}$$

This is equivalent to $\mathcal{Q} \geq 2\lambda\mathcal{E}$ so that (1.12) (for the minimizer) becomes

$$\frac{d}{dt}\mathcal{E} \leq -2\lambda\mathcal{E}. \tag{1.19}$$

Hence, maintaining $\lambda > 0$ in (1.14) and (1.15) is sufficient to ensure that the fluctuating terms $\boldsymbol{u}$ and θ will die off exponentially fast.

Applying the curl operator $\nabla\times$ to (1.14) repeatedly and using incompressibility results in

$$\left(\frac{\lambda}{\mathrm{Pr}} + \Delta\right)\Delta w = -\mathrm{Ra}\left(\Delta - \frac{\partial^2}{\partial z^2}\right)\theta. \tag{1.20}$$

Solving (1.15) for w and substituting this into the above yields an equation in terms of θ only

$$\mathrm{Ra}\left(\Delta - \frac{\partial^2}{\partial z^2}\right)\theta = \left(\frac{\lambda}{\mathrm{Pr}} + \Delta\right)(\lambda + \Delta)\,\Delta\theta. \tag{1.21}$$

Applying the horizontal Fourier transform, imposing periodic horizontal boundaries as in Rayleigh (1916), in terms of the Fourier coefficients of θ this becomes for each wave-number $\mathbf{k}$:

$$\mathrm{Ra}k^2\theta_{\mathbf{k}}(z) = \left(\frac{\lambda}{\mathrm{Pr}} + D^2 - k^2\right)\left(\lambda + D^2 - k^2\right)\left(D^2 - k^2\right)\theta_{\mathbf{k}}(z) \tag{1.22}$$

where $D = \frac{d}{dz}$ and $k = |\mathbf{k}|$. Vanishing temperature fluctuations and vertical velocity at the boundaries forces $\theta_{\mathbf{k}}$ and $D^2\theta_{\mathbf{k}}$ to vanish at $z = 0, 1$. If we consider stress-free velocity boundary conditions we can show (via (1.15)) that $D^4\theta_{\mathbf{k}}$ also vanishes at the boundaries. This indicates that solutions to (1.22) are given by

$$\theta_{\mathbf{k}}(z) = C\sin(n\pi z) \tag{1.23}$$

for $n \in \mathbb{N}$. Plugging this back into (1.22) leads to

$$\mathrm{Ra}k^2 \;=\; \left(\frac{\lambda}{\mathrm{Pr}} - n^2\pi^2 - k^2\right)\left(\lambda - n^2\pi^2 - k^2\right)\left(-n^2\pi^2 - k^2\right). \tag{1.24}$$

Marginal stability will occur when $\lambda = 0$. This yields the critical Rayleigh number

$$\mathrm{Ra} = \frac{(n^2\pi^2 + k^2)^3}{k^2} \tag{1.25}$$

which can be optimized over k and n to obtain $\mathrm{Ra}_c = \frac{27\pi^4}{4}$. A similar calculation can be performed for other combinations of boundary conditions, yielding different critical Rayleigh numbers. Note that the integrations by parts and other arguments used to reach (1.22) do not depend on the choice of vertical boundary condition for the velocity (other than vanishing of w at the vertical plates), so the only differences due to different velocity boundary conditions will be in the solution of (1.22).

1.1.2 Bounds on Heat Transport

The energy stability carried out in the previous section can be considered for more general 'background' temperature profiles $\tau(z)$. Although stability cannot be extracted for $\tau(z) \neq 1 - z$ the construction of quadratic forms produces a framework to consider bounds on interesting statistical properties of the flow. The most interesting characteristic of turbulent convection is the increased transport of heat. Defining $\langle f \rangle$ to be the long-time temporal and spatial average of a function f, the Nusselt number is defined as the ratio of heat transported to that transported via the pure conduction solution (in dimensionless variables the conductive solution has unit transport of heat)

$$\mathrm{Nu} = 1 + \langle w\mathrm{T} \rangle \tag{1.26}$$

where $\langle \cdot \rangle$ represents the spatial and temporal average. One can see immediately that the conductive solution yields $\mathrm{Nu} = 1$. It can be shown that Nu has the following equivalent definitions (see Otero (2002))

$$= \langle |\nabla \mathrm{T}|^2 \rangle \tag{1.27}$$

$$\mathrm{Nu} = 1 + \frac{1}{\mathrm{Ra}} \langle |\nabla \boldsymbol{u}|^2 \rangle \tag{1.28}$$

implying that $\mathrm{Nu} \geq 1$ for all non-conducting solutions.

To formulate a rigorous estimate on Nu, consider specifying a background temperature profile $\tau(z)$ satisfying the appropriate boundary conditions on T so that, following the derivation in the previous section, we can show that the temperature fluctuation $\theta(x, y, z, t)$ satisfies (1.8). Multiplying (1.8) by θ, and the momentum equation by $b\boldsymbol{u}$ (for a constant b) and averaging, using the fact (not proved here) that long time averages of relevant bounded quantities vanish, we can rearrange to

find that

$$\mathrm{Nu} = \langle |\nabla \mathrm{T}|^2 \rangle = \frac{1}{1-b} \int_0^2 \left(\tau'(z)\right)^2 dz - \frac{b}{1-b} - \mathcal{Q} \tag{1.29}$$

where

$$\mathcal{Q}(\boldsymbol{u}, \theta) = \frac{1}{1-b} \int_V |\nabla \theta|^2 d\boldsymbol{x} + \frac{b}{\mathrm{Ra}(1-b)} \int_V |\nabla \boldsymbol{u}|^2 d\boldsymbol{x} + \frac{2}{1-b} \int_V \tau' w \theta d\boldsymbol{x}. \tag{1.30}$$

Choosing $\tau(z)$ then immediately gives an upper bound on Nu provided we can show that $\mathcal{Q}$ is positive definite. The trick is to pick an optimal $\tau(z)$ so that demonstrating the positivity of $\mathcal{Q}$ can be accomplished rigorously.

Each of chapters II, III, and IV apply this method to different problems with either stress-free (as referred to in the previous subsection) or no-slip velocity boundary conditions, to estimate the enhanced heat transport in the presence of strong turbulence. Chapter II addresses the case of internal heating driven convection with no-slip boundaries at infinite Prandtl number where the physically important quantity is the temporally and spatially averaged temperature instead of Nu. Chapter III considers the effects of a stress-free boundary on the 2 dimensional problem considered by Lord Rayleigh and on 2 dimensional internal heating driven convection, both at finite Pr. Chapter IV develops the same bounds obtained in Chapter V but for 3 dimensions and $\mathrm{Pr} = \infty$.

1.2 Climate Modeling

Since the first efforts of Richardson to perform numerical weather prediction (see Richardson (1922); Lynch (2008)), computational resources have increased astronomically and consequently increasingly complicated models have been implemented. Increases in complexity do not however guarantee increases in accuracy or reliability. The weather and climate prediction communities have encouraged the validation of

developing models via a host of numerical and physical test cases that are meant to indicate the increasing ability of the models to simulate meteorologically important phenomena. While modeling groups move towards a transparent set of test cases meant to illustrate the strengths (and consequently downfalls) of each model, it is vital to also be transparent in the engineering practices used in model design. For instance, Jablonowski and Williamson (2011) discusses various dissipative mechanisms that several models implement to maintain stability of the algorithm. As discussed in Chapter V, these ad-hoc forms of dissipation must be considered carefully. Evaluation of models must include a quantification of the effects of this dissipation on the models' output.

Dissipative mechanisms in climate models are essential to maintain algorithmic and numerical stability because even with today's massively parallel computational machinery, resolution of small scale features important to climate is impossible. Instead these features are relegated to a 'sub-grid' distribution that must be modeled. Some of these features are cast into 'parameterizations', greatly simplified routines meant to capture the bulk dynamical integration of distinct physical processes. Improvements in these so called physics routines can greatly affect the model forecast, regardless of the type of discretization used to integrate the underlying partial differential equations describing the fluid evolution. While the impact of the physics can likely not be over-exaggerated, we focus on the dissipative sub-grid mechanisms inherent to the dynamical core (numerical integration of the equations of motion) of a climate model.

1.2.1 Prognostic Equations

Richardson's initial attempt at numerical integration of equations modeling atmospheric motion was deemed a failure because an unstable time-step led to an

unrealistic increase in pressure over central Europe that did not occur. The importance of choosing a stable time-step was illustrated less than a decade later in the seminal paper of Courant, Friedrichs and Lewy (Courant et al. (1928)) and the field of numerical analysis was born. In the 1940s the invention of the modern computer and the blooming field of numerical analysis were used by John von Neumann to simulate explosions and hydrodynamics. von Neumann' success in these areas caused him to revisit Richardson's original attempt at numerical weather prediction. Under von Neumann's guidance, Jule Gregory Charney attacked the problem of simulating atmospheric motion and developed a successful numerical weather model (see Charney et al. (1950)). In addition to the mathematical clarity provided by advances in numerical methods, and the advent of modern computing, one of Charney's fundamental contributions to the field of numerical weather prediction was the realization that simplified, filtered sets of equations may yield accurate and computationally feasible results.

In Charney et al. (1950) the authors expressed the desire to integrate the fully compressible Euler equations, but acknowledge that in light of the CFL (Courant-Friedrichs-Lewy Courant et al. (1928)) condition, such an undertaking would not be feasible with the available computational resources of the time. As outlined in Charney (1948, 1949) a simplified equation set was considered, providing a realistic model for numerics to be applied. Since that time, a hierarchy of equations have been simulated, dependent on the desired level of accuracy and computational resources. Before considering the numerical treatment of these equations, and the need for added dissipation, it is useful to discuss the various equation sets used in practice.

The prognostic equations for motion of the earth's atmosphere are

$$\frac{\partial \rho}{\partial t} + \nabla \cdot (\rho \boldsymbol{u}) = 0 \tag{1.31}$$

$$\frac{\partial \theta}{\partial t} + \boldsymbol{u} \cdot \nabla \theta = \mathcal{Q} \tag{1.32}$$

$$\frac{\partial \boldsymbol{u}}{\partial t} + \boldsymbol{u} \cdot \nabla \boldsymbol{u} + 2\Omega \times \boldsymbol{u} + \frac{1}{\rho} \nabla p = -\nabla \Phi + \mathcal{F} \tag{1.33}$$

where ρ is the density, $\boldsymbol{u}$ the three-dimensional velocity, θ the potential temperature, $\mathcal{Q}$ a diabatic source term, Ω the rotation vector indicating the earth's rotation, p the pressure, Φ the geopotential, and $\mathcal{F}$ additional forces such as friction. The potential temperature is related to the other thermodynamic variables (temperature T in particular) via

$$\theta = T \left(\frac{p_0}{p} \right)^{\kappa} \tag{1.34}$$

where p_0 is a reference pressure (typically $10^5 Pa$) and $\kappa = R/C_p$ for dry air gas constant R and specific heat capacity at constant pressure C_p. The system is completely described by considering the equation of state for an idea gas

$$p = RT\rho. \tag{1.35}$$

Conservation of mass following the flow is ensured via (1.31). The evolution and conservation of momentum in the absence of frictional forces is guaranteed by (1.33), and (1.32) indicates that potential temperature is conserved when $\mathcal{Q} = 0$. Note that this system of equations is written in vector-invariant form, i.e., in reality on the earth's surface there is a need to move to some type of spherical grid with appropriate geometric considerations in all of the incident derivatives. In addition while we are considering the Coriolis force ($\Omega \times \boldsymbol{u}$) explicitly, we have included the centrifugal force due to a rotating coordinate system in the gradient of the geopotential (in addition to the gravitational force).

One of the most frequent approximations made in the study of the earth's atmosphere is to assume the earth is a perfect sphere with average radius a. In addition, one may assume that the geopotential ϕ is dependent only on r the distance from the center of the earth implying that $\nabla\phi$ acts on the vertical component of momentum only. Some additional assumptions on the geometric factors in the spherical coordinate formation of the equations leads to what is typically referred to as the 'shallow atmosphere' approximation (see Thuburn (2011a)).

A common simplification is the anelastic approximation where (1.31) is reduced to

$$\nabla \cdot (\rho_0 \boldsymbol{u}) = 0. \tag{1.36}$$

For an anelastic fluid, $\rho_0 = \rho_0(z)$ is dependent on the vertical independent variable only. When ρ_0 is a constant this leads to incompressibility. Anelasticity is typically valid on small spatial scales, but is inaccurate for synoptic scale motions, and in the atmosphere at least, incompressibility neglects some important wave interactions that influence the large scale mean flows.

Another approximation that has proven useful is called the hydrostatic assumption and neglects the effects of acceleration with the flow in the vertical component of velocity. This is valid because it is well known that the vertical velocity (except in regions of strong convection) is typically extremely small in comparison to horizontal velocities. This, in concert with the extremely small aspect ratio of the atmosphere and oceans (the atmosphere is very thin in comparison to the expanse of the globe horizontally) make this assumption valid. And this indicates conditions when the hydrostatic assumption is not accurate, when the vertical and horizontal motion are similar in magnitude. This typically occurs at scales below $10km$, a horizontal scale

that is fast being approached by modern general circulation models (see Thuburn (2011a)).

The hydrostatic assumption can also be considered as a balance between gravity and the pressure gradient. This balance implies an infinite speed of propagation for internal acoustic waves that otherwise dictate a severe restriction on the numerical time-step (see next subsection for an explanation). In essence then, the hydrostatic assumption can be considered a filtered version of (1.33) where the acoustic waves have been judiciously removed. In concert with the shallow atmosphere assumptions on the geometry of the system (see White et al. (2005) for details), this leads to the 'hydrostatic primitive equations' which for the momentum, are

$$\frac{\partial u}{\partial t} + \frac{u}{a\cos\phi}\frac{\partial u}{\partial \lambda} + \frac{v}{a}\frac{\partial u}{\partial \phi} + w\frac{\partial u}{\partial z} = \frac{uv}{a}\tan\phi + 2\Omega v\sin\phi - \frac{1}{\rho a\cos\phi}\frac{\partial p}{\partial \lambda} \tag{1.37}$$

$$\frac{\partial v}{\partial t} + \frac{u}{a\cos\phi}\frac{\partial v}{\partial \lambda} + \frac{v}{a}\frac{\partial v}{\partial \phi} + w\frac{\partial v}{\partial z} = -\frac{u^2}{a}\tan\phi - 2\Omega u\sin\phi - \frac{1}{\rho a}\frac{\partial p}{\partial \phi} \tag{1.38}$$

$$\frac{\partial p}{\partial z} = -\rho g. \tag{1.39}$$

Here the substitution of a constant mean radius to the earth's surface is made, i.e. $r = a + z$ where a is a constant. The independent variables are latitude ϕ, longitude λ and height z with corresponding wind components u, v, w, density ρ, pressure p, and magnitude of the rotation vector Ω.

The non-hydrostatic primitive equations are produced by replacing (1.39) with

$$\frac{\partial w}{\partial t} + \frac{u}{a\cos\phi}\frac{\partial w}{\partial \lambda} + \frac{v}{a}\frac{\partial w}{\partial \phi} + w\frac{\partial w}{\partial z} = g - \frac{1}{\rho}\frac{\partial p}{\partial z}. \tag{1.40}$$

As detailed in White et al. (2005) the quasi-hydrostatic equations are an intermediate set of equations between (1.39) and (1.40) that partially resolves the smaller scales, while removing the fast waves that place stringent constraints on the time-stepping. (1.40) is valid on scales smaller than $10km$, but the vertical acoustic modes dictate a sever time-step restriction that can be costly in the numerics.

Each of these equation sets have advantages and disadvantages that need to be considered when developing the individual model. When choosing the set of equations, one must consider the available computational resources, and consider what the goal of the model is. For example, a model that intends to simulate climate scale characteristics on long time scales of hundreds of years would likely fare well with the hydrostatic equations, while a short term regional weather forecast may need to consider the non-hydrostatic effects that play a significant role in the smaller scales.

1.2.2 Numerical Algorithms

Once a continuous set of equations is chosen for a model, it remains to select the method of discretization. There are various ways of discretizing the equations of motion that are complicated by the spherical geometry of the earth, and the desire to maintain certain conservation properties inherent to the continuous equations. As when choosing the set of equations, the modelers are faced with a trade off between accuracy and finite resources. A customary approach in numerical modeling is to discretize the continuous equations as accurately and efficiently as possible, supposing that in the limit of small grid spacings, the solutions will converge to reality. Climate models are not near (nor will they be soon) the limit of small grid spacing, and it is desirable to focus not only on the accuracy of individual components of the discretization, but on the overarching ability of the scheme to maintain certain physically meaningful identities such as conservation of energy. In this sense, low order schemes that conserve certain meaningful relations, may be preferable to higher order approximations that sacrifice such properties for accuracy of individual components of the model (see Rood (2011) for a more thorough discussion).

Adequate filtering of the continuous equations can be used to eliminate fast propagating waves as mentioned in the previous subsection, but there are numerical

methods that can perform this same function. In this sense the numerical algorithm should be chosen in concert with the set of approximations made to determine the set of continuous equations. Dissipative numerical algorithms applied to the full equations may yield similar results to less dissipative techniques applied to a filtered set of equations. In addition some numerical techniques are better suited for different forms of the underlying equations, i.e. spectral transform models often incorporate the horizontal vorticity divergence form of the equations (for example consider the spectral transform Eulerian dynamical core CAM-EUL described in Neale et al. (2010)), while grid-point or finite-volume methods may choose the vector invariant form (see Lin and Rood (1996)). All of these considerations must be considered both when choosing the equation set and the numerical algorithm used to integrate the equations.

The first step in considering the vertical motion (after choosing the set of equations) is to determine a vertical coordinate. Thuburn (2011b) describes different options for the vertical coordinate, each of which has potential positive or negative impacts on the discretization of the dynamics. Typically a pressure-based approach is used in climate models in concert with the hydrostatic assumption, as the continuity equation (1.39) is then diagnostic. Height-based, and isentropic (based on potential temperature) coordinates have individual advantages as well, but the numerical implementation of each introduces particular challenges. The choice of vertical grid, and in particular the staggering of the variables plays an important role, although not as significantly as in the horizontal direction. The choice of vertical grid, coordinate, and underlying equation set influence the design of the numerics (see Konor and Arakawa (1997); Lin (2004) for some examples of vertical discretizations).

In climate models, because the horizontal motion dominates, the choice of hori-

zontal grid has a significant impact on the model design. Williamson (2007) focuses on the issues relevant to polar singularities that occur for a latitude-longitude grid, and briefly discusses several grid options. Some of the more popular alternatives to the traditional latitude-longitude grid are the cubed sphere (see Sadourny (1972); Putman and Lin (2009); Taylor et al. (2007) for some examples) and geodesic grids (see Sadourny et al. (1968); Williamson (1968); Gassman and Herzog (2008)). As pointed out in Williamson (2007) the choice of horizontal grid affects the corresponding choice of numerical algorithm. In particular Taylor (2011) points out the impact that the grid's geometry has on the ability of a scheme to conserve fundamental properties of the flow. Some algorithms are built for quadrilateral grids and would require a substantial effort to adjust to different geometries, especially if conservation of certain quantities was desired. These points illustrate the impact the grid has on the choice of the numerical algorithm.

In concert with choosing the grid, the choice of discretization for the horizontal component of the model can have a significant impact on the model output. As such there is a plethora of possibilities. Although the original models were formulated via finite differences, spectral transform methods quickly found footing in the community and are still in use by some General Circulation Models today (consider the Eulerian, and semi-Lagrangian models in Neale et al. (2010) for two examples). Finite volume methods, originally developed in the 1970s (see van Leer (1974, 1977) among others) for high energy hydrodynamics, have gained traction in recent years across a variety of grids (consider the finite volume dynamical core in Neale et al. (2010), as well as Putman and Lin (2009); Ringler (2011) for some examples). In addition we will consider finite-element based methods, common to engineering applications, and recently adapted to integration of the atmosphere (see Taylor et al. (2007); Nair

et al. (2011)). As with all other choices made in model development, each of these methods has both negative and positive effects on the model.

Part of the goal of this thesis is to understand how the choices in grid, numerics and set of equations is reflected in the sub-grid scales, and the corresponding mixing characteristics inherent to each model. To this end, Chapter V discusses the impact that an explicit dissipative term has on the numerical stability of the finite volume dynamical core of the Community Atmosphere Model (CAM-FV). The impact of the latitude-longitude grid and the potential improvements due to a more uniform grid are considered. Chapter VI proposes a test that will examine the dissipative nature of a model's dynamical core in comparison to its tracer advection routines.

CHAPTER II

Internal heating driven convection at infinite Prandtl number: sticky (no-slip) boundaries

2.1 Introduction

Thermal convection is the buoyancy-driven flow of a fluid heated from below and/or cooled from above. An ongoing challenge for analysis, theory, computation, and experiment is to ascertain how the heat transport depends on the thermal forcing as gauged by a nondimensional Rayleigh number and the fluid's material properties, typically characterized by the dimensionless Prandtl number, the ratio of kinematic viscosity to thermal diffusivity Ahlers et al. (2009). Bounds on heat transport within the Boussinesq approximation were pioneered by Howard Howard (1963) and elaborated by Busse Busse (1969). Later, following the motivational work of Hopf Hopf (1940), an alternative variational framework for bounds on turbulent transport of momentum, mass, and in the case of convection, heat, known as the 'background method' was formulated Doering and Constantin (1996). This is the approach we adopt here.

In this Chapter we consider an infinite Prandtl number Boussinesq fluid contained between two rigid isothermal boundaries thermally driven by constant internal heating. This model is inspired by convection in the Earth's mantle where the Prandtl number is $\mathcal{O}(10^{24})$ and the motion is predominantly driven by a semi-uniform heat-

ing from radioactive decay. For definiteness we consider an idealization of the actual geophysical conditions: an isoviscous fluid subject to no-slip isothermal vertical boundary conditions—without loss of generality the temperature equals 0 on the boundaries—and uniform heating at volumetric heat rate $\mathcal{H}\rho c$ where ρ is the density of the fluid and c is the specific heat.

Bulk heating is measured in terms of the dimensionless 'heat Rayleigh number' $\mathrm{R} = \frac{g\alpha\mathcal{H}h^5}{\nu\kappa^2}$ where g is the acceleration of gravity, α is the fluid's thermal expansion coefficient, h is the thickness of the layer, ν is the fluid's viscosity, and κ is its thermal diffusivity Roberts (1967). At low heating rates, i.e., for R below a finite critical value, the fluid remains at rest and heat is transported to the boundaries by conduction within a parabolic temperature profile across the layer shown in Fig. 2.1 (the solid curves). At higher heating rates convection sets in to actively transport heat, predominantly toward the upper boundary. Fig. 2.1 also contains a sketch (the dashed curve) of the expected form of the horizontally averaged temperature profile for internal heat driven convection with fixed temperature boundaries: convection decreases the temperature relative to the purely conductive values throughout most of the layer, preferentially transporting heat upward and producing a boundary layer of thickness $\delta \ll h$ near the top to satisfy the temperature boundary condition.

The challenge is to determine how the space-time averaged temperature $\langle\mathcal{T}\rangle$ varies with $\mathcal{H}$. Equivalently, the enhancement of heat transport is gauged nondimensionally by the space-time averaged temperature measured in units of $\mathcal{H}h^2/\kappa$ and the challenge is to determine how dimensionless $\langle T\rangle = \kappa\langle\mathcal{T}\rangle/\mathcal{H}h^2$ varies with R. The no-convection parabolic conduction solution exists for all values of $\mathcal{H}$ (or R) and, even though it is unstable at high heating rates, realizes the upper limit on the bulk averaged temperature for all values of $\mathcal{H}$ (or R). That is, $\langle\mathcal{T}\rangle \leq \frac{\mathcal{H}h^2}{12\kappa}$ (or $\langle T\rangle \leq \frac{1}{12}$).

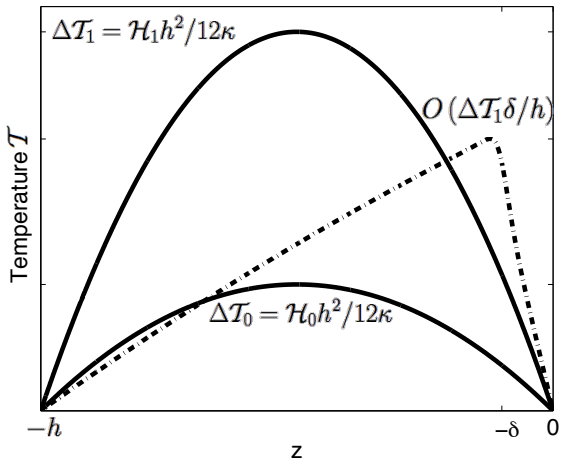

Figure 2.1: Sketches of horizontally and temporally averaged temperature profiles. The parabolic conduction profiles (solid curves) are stable at low R (say, for heating rate $\mathcal{H}_0$) and unstable state for large R (say, for $\mathcal{H}_1 > \mathcal{H}_0$). In the turbulent convection state at the higher heating rates $\mathcal{H}_1$, the heat is preferentially transported upward and a thermal boundary layer of thickness $\delta \ll h$ appears. The natural temperature scale is $\Delta\mathcal{T} = \mathcal{H}h^2/\kappa$, proportional to the maximum of the quadratic conduction profiles, but the amplitude of convection profiles is reduced by a factor of δ/h

The goal is to derive lower bounds on $\langle\mathcal{T}\rangle$ as a function of $\mathcal{H}$. In nondimensional terms, at high R the question is how low can $\langle T\rangle$ go?

A heuristic marginally stable boundary layer argument Malkus (1954) predicts the sublinear scaling estimate $\langle\mathcal{T}\rangle \sim \mathcal{H}^{3/4}$ in the presence of convection, corresponding to $\langle T\rangle \sim \mathrm{R}^{-1/4}$. The basic idea is that as the heating increases and convection sets in, the upper thermal boundary layer forms where the fluid is pinned at rest by the no-slip boundary. The constant heating produces a fixed heat flux across the upper boundary layer and the peak temperature of the averaged profile must be $\sim \frac{\delta}{h} \times \frac{\mathcal{H}h^2}{\kappa}$ so that the top of the boundary layer has a slope $\sim \frac{\mathcal{H}h}{\kappa}$ to conduct the majority of the heat out of the layer. Then $\langle\mathcal{T}\rangle \sim \frac{\mathcal{H}h\delta}{\kappa}$, so if we can infer how δ varies with the control parameters we can infer the scaling. The fundamental hypothesis is that the boundary layer thickness is precisely what it needs to be so that as a convection system unto itself, the boundary layer is marginally stable: if it were any thinner diffusion would cause it to grow, and if it were any thicker fluid motion would

commence and it would not exist as a static layer.

So consider the boundary layer from $-\delta$ to 0 as a distinct convective layer. Although we do not strictly speaking have boundary conditions on the bottom of the boundary layer, we presume that the velocity satisfies free-slip boundary conditions there; it certainly satisfies no-slip conditions at the top. Meanwhile the temperature satisfies a fixed temperature $\mathcal{T} = 0$ at the top and a fixed heat flux condition at the bottom of the boundary layer. The volumetric heating constant $\mathcal{H}$ is the same in the boundary layer as in the bulk, but there is also an imposed temperature gradient due to the incoming flux of heat from below. There are thus two driving forces that can each be described through nondimensional numbers (see Sparrow et al. (1963)). The first is a measure of the strength of the internal heating in the layer,

$$\mathrm{N}_\delta = \frac{\mathcal{H}\delta^2}{\Delta\mathcal{T}_\delta \kappa} \sim \frac{\delta}{h}, \tag{2.1}$$

where $\Delta\mathcal{T}_\delta \sim \frac{\mathcal{H}h\delta}{\kappa}$ is the temperature drop across the layer. This vanishes rapidly as the boundary layer decreases in size, i.e., for $\delta/h << 1$. The second non-dimensional number reflects the influence of the temperature gradient, namely the traditionally defined Rayleigh number

$$\mathrm{Ra}_\delta = \frac{g\alpha\Delta\mathcal{T}_\delta\delta^3}{\nu\kappa}. \tag{2.2}$$

Because $\mathrm{N}_s = O\left(\frac{\delta}{h}\right)$ we can neglect the effect of internal heating in the boundary layer and consider that in the turbulent regime, the boundary layer is a marginally stable conductive solution driven by the temperature gradient imposed by the fixed flux from below. Marginal stability means that Ra_δ assumes the relevant critical value 647, the critical Rayleigh number for convection with free-slip, fixed-flux on bottom, and no-slip, fixed temperature upper boundary conditions. Thus

$$647 \approx Ra_\delta = \frac{g\alpha\mathcal{H}\delta^4 h}{\nu\kappa^2} = \frac{\delta^4}{h^4}\mathrm{R}. \tag{2.3}$$

It follows that $\delta \approx 5h\mathrm{R}^{-1/4}$ suggesting that

$$\langle \mathcal{T} \rangle \approx \frac{\mathcal{H}h\delta}{2\kappa} \sim \frac{5\mathcal{H}h^2}{2\mathrm{R}^{1/4}\kappa} \sim \mathcal{H}^{3/4} \tag{2.4}$$

and, nondimensionally, that

$$\langle T \rangle \approx 2.5\, R^{-1/4}. \tag{2.5}$$

In this Chapter we prove

$$\langle T \rangle \geq 0.419\, \mathrm{R}^{-1/4} (\log \mathrm{R})^{-1/4} \quad \Rightarrow \quad \langle \mathcal{T} \rangle \gtrsim \mathcal{H}^{3/4} (\log \mathcal{H})^{-1/4}\,. \tag{2.6}$$

The rigorous lower bound is, modulo a logarithmic correction, consistent with the predictions of the marginally stable boundary layer argument. Moreover, it is not inconsistent with a scaling law measured from direct numerical simulations in Sotin and Labrosse (1999) implying that $\langle T \rangle \sim 1.65\, \mathrm{R}^{-0.234}$. We note, however, that those computations employed free-slip velocity boundary conditions rather than the no-slip conditions employed in the analysis here. Boundary conditions can drastically affect the fluid dynamics (and the bounds Ierley et al. (2006); **?**) for Rayleigh-Bénard convection so the comparison must be taken with a degree of caution.

Bounds for this internal heating problem were previously considerd by Lu *et al* Lu et al. (2004) who used estimates originally derived for boundary driven Rayleigh-Bénard convection Doering and Constantin (2001) and a simple piecewise linear background profile to produce a lower bound. That result was $\langle T \rangle \geq 0.81\, \mathrm{R}^{-2/7}$, or in dimensional units $\langle \mathcal{T} \rangle \gtrsim \mathcal{H}^{5/7}$. Subsequent developments Ierley et al. (2006); Doering et al. (2006) indicated that optimal background profiles for infinite Prandtl number convection may include some stable stratification suggesting there was room for improvement. In particular, a singular integral analysis produced a key estimate that was then utilized in the background method to establish an upper bound on the

Nusselt number Nu, the dimensionless measure of the enhancement of heat transport in boundary-driven Rayleigh-Bénard convection, in terms of the traditional Rayleigh number Ra of the form $\mathrm{Nu} \lesssim [\mathrm{Ra}\log(\mathrm{Ra})]^{1/3}$ Doering et al. (2006). In this paper we show that that key estimate is a modified Hardy-Rellich inequality and we derive the sharp prefactor. The newly derived inequality, along with some additional considerations, is then applied to the internal heating problem via the background method to obtain the improved result.

The rest of this Chapter is organized as follows. The next section describes the Boussinesq equations of motion with internal heating and provides an outline of the background method applied to the problem. Section III introduces the particular background temperature field as a logarithmic perturbation of a quadratic profile and applies the modified Hardy-Rellich estimate to obtain the bound (2.6). Section IV discusses these results and briefly remarks on the parallels between the internal heating and boundary driven convection problems. The new derivation of the Hardy-Rellich inequality is described in the appendix.

2.2 Internal Heating and the Background Method

The equations of motion in the Boussinesq approximation are

$$\frac{\partial \boldsymbol{u}}{\partial t} + \boldsymbol{u}\cdot\nabla\boldsymbol{u} = -\nabla p + \nu\nabla^2\boldsymbol{u} + g\alpha\mathcal{T}\hat{\boldsymbol{k}} \tag{2.7}$$

$$\nabla\cdot\boldsymbol{u} = 0 \tag{2.8}$$

$$\frac{\partial \mathcal{T}}{\partial t} + \boldsymbol{u}\cdot\nabla\mathcal{T} = \kappa\nabla^2\mathcal{T} + \mathcal{H} \tag{2.9}$$

where p is the pressure field, ν is the kinematic viscosity, g is the acceleration of gravity, α is the thermal expansion coefficient, and κ is the thermal diffusivity. The volumetric heat flux pumped into the system is $\mathcal{H}\rho c$ where ρ and c are the fluid's density and specific heat. We consider a fluid layer of height h with no-slip boundary

conditions in the vertical (z) direction, i.e., $\boldsymbol{u}|_{z=-h} = 0 = \boldsymbol{u}|_{z=0}$. The temperature satisfies $\mathcal{T}|_{z=-h} = 0 = \mathcal{T}|_{z=0}$, and all variables are periodic in the horizontal (x and y) directions with periods L_x and L_y.

The conventional dimensionless formulation Lu et al. (2004) uses the time-scale h^2/κ, the length scale is h, and the temperature is measured in units of $\mathcal{H}h^2/\kappa$. Then

$$\frac{1}{\mathrm{Pr}}\left(\frac{\partial \boldsymbol{u}}{\partial t} + \boldsymbol{u}\cdot\nabla\boldsymbol{u}\right) + \nabla p = \nabla^2\boldsymbol{u} + \mathrm{R}\,T\,\hat{\boldsymbol{k}} \tag{2.10}$$

$$\frac{\partial T}{\partial t} + \boldsymbol{u}\cdot\nabla T = \nabla^2 T + 1 \tag{2.11}$$

$$\nabla\cdot\boldsymbol{u} = 0 \tag{2.12}$$

where the heat Rayleigh number is $\mathrm{R} = \frac{g\alpha\mathcal{H}h^5}{\nu\kappa^2}$ and $\mathrm{Pr} = \frac{\nu}{\kappa}$ is the Prandtl number. Combined with the divergence-free condition (2.12), the no-slip velocity boundary condition implies that $\partial w/\partial z = 0$ at the top and bottom boundaries.

Defining the space-time average of a function $f(x, y, z, t)$ as

$$\langle f\rangle = \lim_{t\to\infty}\frac{1}{t}\int_0^t ds\,\frac{h}{L_x}\int_0^{L_x/h} dx\,\frac{h}{L_y}\int_0^{L_y/h} dy\int_{-1}^{0} dz\, f(x,y,z,s) \tag{2.13}$$

(assuming that the limits exist) we are interested in obtaining a lower bound on the average temperature $\langle T\rangle$ in terms of the Rayleigh heat number R. From this point on we focus on the infinite Pr limit of (2.10), the validity of which has recently been established Wang (2004), so that the Navier-Stokes momentum equations become the Stokes equations

$$\nabla p = \nabla^2\boldsymbol{u} + \mathrm{R}T\hat{\boldsymbol{k}}. \tag{2.14}$$

To apply the background method, write the temperature field as the sum of a stationary background profile and fluctuations according to $T(x, y, z, t) = \tau(z) + \theta(x, y, z, t)$ where $\tau(-1) = \tau(0) = 0$ so the fluctuation $\theta(x, y, z, t)$ satisfies homoge-

neous Dirichlet conditions at the top and bottom boundaries. Applying this decomposition to the equations of motion we arrive at the following

$$\nabla p = \nabla^2 \boldsymbol{u} + \mathrm{R}(\tau + \theta)\hat{\boldsymbol{k}} \tag{2.15}$$

$$\frac{\partial \theta}{\partial t} + \boldsymbol{u} \cdot \nabla \theta = \nabla^2 \theta + \tau'' + 1 - w\tau' \tag{2.16}$$

where $\boldsymbol{u} = (u, v, w)^T$ and $\tau' = \frac{d\tau}{dz}$.Applying (2.13) to $\theta\cdot$ (2.16) and $\tau\cdot$ (2.16) yields

$$\langle \tau' w\theta \rangle = -\langle |\nabla\theta|^2 \rangle - \left\langle \tau' \frac{\partial \theta}{\partial z} \right\rangle + \langle \theta \rangle, \tag{2.17}$$

$$-\langle \tau' w\theta \rangle = -\left\langle \tau' \frac{\partial \theta}{\partial z} \right\rangle + \langle \tau \rangle - \langle (\tau')^2 \rangle. \tag{2.18}$$

In order to eliminate the term involving the vertical derivative of the fluctuation θ consider the difference of these two identities:

$$\langle \theta \rangle - \langle \tau \rangle = 2\langle \tau' w\theta \rangle + \langle |\nabla\theta|^2 \rangle - \langle (\tau')^2 \rangle. \tag{2.19}$$

It follows that

$$\langle T \rangle = 2\langle \tau \rangle - \langle (\tau')^2 \rangle + \langle |\nabla\theta|^2 \rangle + 2\langle \tau' w\theta \rangle. \tag{2.20}$$

The key idea behind the background method is that one can immediately see that

$$\langle T \rangle \geq 2\langle \tau \rangle - \langle (\tau')^2 \rangle \tag{2.21}$$

as long as the quadratic (in θ) functional

$$Q = \langle |\nabla\theta|^2 \rangle + \langle 2\tau' w\theta \rangle \tag{2.22}$$

is positive semidefinite among temperature fluctuations and velocity fields satisfying the boundary conditions. Q is quadratic in θ because, applying the curl operator twice to (2.14), it is evident that there is an instantaneous linear albeit nonlocal slaving of the vertical velocity w to θ:

$$\Delta^2 w = -\mathrm{R}\Delta_H \theta \tag{2.23}$$

where Δ is the full Laplacian and Δ_H is the horizontal Laplacian $\frac{\partial^2}{\partial x^2} + \frac{\partial^2}{\partial y^2}$.

For calculational convenience we apply the Fourier transform in the horizontal directions to obtain the relation for each wave number $k = |\mathbf{k}|$,

$$\left(\frac{d^2}{dz^2} - k^2\right)^2 \hat{w}_{\mathbf{k}} = \mathrm{R}k^2\hat{\theta}_{\mathbf{k}}$$

where now for all $\mathbf{k}$ the single-wavenumber quadratic forms

$$Q_{\mathbf{k}} := \int_{-1}^{0} \left[\left| \frac{d\hat{\theta}_{\mathbf{k}}}{dz} \right|^2 + k^2|\hat{\theta}_{\mathbf{k}}|^2 + 2\tau' Re[\hat{\theta}_{\mathbf{k}}\hat{w}_{\mathbf{k}}] \right] dz$$

must all remain positive semidefinite. In the following we consider $Q_{\mathbf{k}}$ wavenumber by wavenumber so we drop the $\hat{\cdot}$ and subscript $\mathbf{k}$. In other words we seek to maximize $2\langle\tau\rangle - \langle(\tau')^2\rangle$ while maintaining positivite-semidefiniteness of

$$Q := \int_{-1}^{0} \left[\left| \frac{d\theta}{dz} \right|^2 + k^2|\theta|^2 + 2\tau' Re[\theta w] \right] dz \tag{2.24}$$

uniformly in k, where $\theta(z)$ satisfies homogeneous Dirichlet boundary conditions and $w(z)$ solves

$$w'''' - 2k^2 w'' + k^4 w = \mathrm{R}k^2\theta, \tag{2.25}$$

and satisfies both homogeneous Dirichlet and Neumann boundary conditions on $[-1, 0]$.

Previous analysis of this problem and boundary driven convection considered background profiles $\tau(z)$ constant in the bulk of the layer so the only possible negative contribution to Q relied on the product of $w(z)$ and $\theta(z)$ in boundary layers where both are constrained to be relatively small in magnitude. As was discovered for boundary driven convection, however, a stably stratified (i.e. $\tau'(z) > 0$) profile in the bulk can be exploited to utilize the positive weighted correlation between w and θ resulting from the slaving and improve the positivity of Q, allowing for sharper estimates Doering et al. (2006).

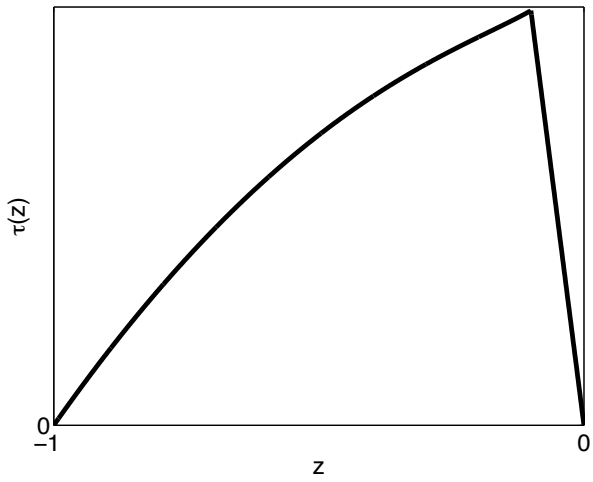

Figure 2.2: Background profile (2.26).

2.3 Singular perturbation of a stably stratified profile

Consider the family of background profiles illustrated in Figure 2.2,

$$\tau(z) = \begin{cases} a\log\left(\frac{-1}{z}\right) + b\,(1-z^2) & -1 \le z \le -\delta \\ \frac{-z}{\delta}\left[a\log(1/\delta) + b(1-\delta^2)\right] & -\delta \le z \le 0, \end{cases} \tag{2.26}$$

where the positive parameters $\delta < 1$, a, and b will be chosen to optimize the bound. The logarithmic term enhances the positivity of Q, and hence leads to an improved scaling of the boundary layer with R, while the quadratic term is meant to increase the integral of $\tau(z)$ sufficiently to offset the slow logarithmic growth near $z = -1$ and lessening the negative impact of the Dirichlet integral in (2.21).

It is easily verified that

$$\int_{-1}^{0} \tau(z)dz = a\left[1-\delta-\frac{\delta\log(1/\delta)}{2}\right] + b\left[\frac{2}{3}-\frac{\delta}{2}-\frac{\delta^3}{6}\right], \tag{2.27}$$

$$\int_{-1}^{0} \left(\tau'(z)\right)^2 dz = a^2\left(\frac{1}{\delta}-1+\frac{\left[\log(1/\delta)\right]^2}{\delta}\right) \tag{2.28}$$

$$+ \; ab\left(2\frac{\log(1/\delta)}{\delta}+4-2\delta\log(1/\delta)-4\delta\right) \tag{2.29}$$

$$+ \; b^2\left(\frac{1}{\delta}+\frac{4}{3}-2\delta-\frac{\delta^3}{3}\right), \tag{2.30}$$

producing the lower bound on the average temperature $\langle T \rangle$ given by (2.21) when the positivity of Q is maintained. An appropriate choice of the scaling of the parameters a and b with respect to δ will allow us to determine both the 'correct' boundary layer scaling, and to maximize the lower bound on $\langle \mathrm{T} \rangle$.

The two key inequalities required for the analysis are

$$\int_{-1}^{0} \theta(z) w^*(z) z dz \quad \leq \quad 0 \tag{2.31}$$

and

$$\int_{-1}^{0} \frac{\theta(z) w^*(z)}{z} dz \quad \leq \quad \frac{4}{\mathrm{R}} \int_{-1}^{0} \frac{|w(z)|^2}{z^3} dz \ \leq \ 0. \tag{2.32}$$

The first inequality (2.32) is an exercise in integration by parts the details of which are left to the reader. The second inequality (2.32) is a restatement—and slight improvement in the prefactor—of the key result previously derived for Rayleigh-Bénard convection Doering et al. (2006). While a prefactor improvement may be considered minor, our approach significantly simplifies the proof and embeds the problem in the context of generalized Hardy-Rellich inequalities. The proof, provided in the Appendix, also establishes that the estimate with this prefactor is sharp.

To determine conditions guaranteeing the positivity of Q we reformulate it neglecting much of the L^2 norm of $\frac{d\theta}{dz}$ as well as the $k^2|\theta|^2$ term and use (2.31) to observe

$$Q \ \geq \ \int_{-\delta}^{0} \left| \frac{d\theta}{dz} \right|^2 dz - 2a \int_{-1}^{0} \frac{Re[\theta w^*]}{z} dz \tag{2.33}$$

$$- \ \int_{-\delta}^{0} \left(\frac{2a \log(1/\delta)}{\delta} - \frac{2a}{z} - 4bz + \frac{2b(1-\delta^2)}{\delta} \right) Re[\theta w^*] dz. \tag{2.34}$$

In the above we added the bulk terms to the boundary layer in order to apply (2.31)

and (2.32) to the entire interval. Applying (2.32) then implies

$$\begin{aligned} Q &\geq \int_{-\delta}^{0} \left|\frac{d\theta}{dz}\right|^2 dz - \frac{8a}{\mathrm{R}} \int_{-1}^{0} \frac{|w|^2}{z^3} dz \\ &- \int_{-\delta}^{0} \left(\frac{2a\log(1/\delta)}{\delta} - \frac{2a}{z} - 4bz + \frac{2b(1-\delta^2)}{\delta} \right) Re[\theta w^*] dz. \end{aligned} \tag{2.35}$$

Bound the magnitude of the last integral in (2.35) as follows:

$$\left| \int_{-\delta}^{0} \left(\frac{2a\log(1/\delta)}{\delta} - \frac{2a}{z} - 4bz + \frac{2b(1-\delta^2)}{\delta} \right) Re[\theta w^*] dz \right| \tag{2.36}$$

$$\leq \int_{-\delta}^{0} \left(\frac{2a\log(1/\delta)}{\delta} - \frac{2a}{z} - 4bz + \frac{2b(1-\delta^2)}{\delta} \right) z^2 \frac{|\theta|}{|z|^{1/2}} \frac{|w|}{|z|^{3/2}} dz \tag{2.37}$$

$$\leq 2 \left(\sup_{-\delta \leq z \leq 0} \frac{|\theta(z)|}{|z|^{1/2}} \right) \left(\int_{-\delta}^{0} z^4 \left[\frac{a\log(1/\delta)}{\delta} - \frac{a}{z} - 2bz + \frac{b(1-\delta^2)}{\delta} \right]^2 dz \right)^{1/2} \tag{2.38}$$

$$\times \left(\int_{-1}^{0} \frac{|w|^2}{|z|^3} dz \right)^{1/2}. \tag{2.39}$$

The homogeneous boundary conditions on $\theta(z)$ mean that for $z \in (-\delta, 0)$,

$$|\theta(z)| = \left| \int_z^0 \frac{d\theta}{d\tilde{z}} d\tilde{z} \right| \leq |z|^{1/2} \left(\int_z^0 \left| \frac{d\theta}{d\tilde{z}} \right|^2 d\tilde{z} \right)^{1/2} \leq |z|^{1/2} \left(\int_{-\delta}^0 \left| \frac{d\theta}{dz} \right|^2 dz \right)^{1/2}. \tag{2.40}$$

Hence we can bound the supremum in (2.38) and apply Young's inequality to see that

$$\left| \int_{-\delta}^{0} \left(\frac{2a\log(1/\delta)}{\delta} - \frac{2a}{z} - 4bz + \frac{2b(1-\delta^2)}{\delta} \right) Re[\theta w^*] dz \right| \leq \tag{2.41}$$

$$\int_{-\delta}^{0} \left| \frac{d\theta}{dz} \right|^2 dz + \int_{-\delta}^{0} z^4 \left[\frac{a\log(1/\delta)}{\delta} - \frac{a}{z} - 2bz + \frac{b(1-\delta^2)}{\delta} \right]^2 dz \times \int_{-1}^{0} \frac{|w|^2}{|z|^3} dz. \tag{2.42}$$

Inserting (2.42) into (2.35) we see that

$$Q \geq \left\{ \frac{8a}{\mathrm{R}} - \int_{-\delta}^{0} z^4 \left[\frac{a\log(1/\delta)}{\delta} - \frac{a}{z} - 2bz + \frac{b(1-\delta^2)}{\delta} \right]^2 dz \right\} \int_{-1}^{0} \frac{|w|^2}{|z|^3} dz. \tag{2.43}$$

The integral about the boundary layer in (2.43) can be computed exactly. At this point we choose $a = a'\delta/\log(1/\delta)$ and $b = b'\delta$ where a' and b' are $\mathcal{O}(1)$ absolute

constants. Then

$$\int_{-\delta}^{0} z^4 \left[\frac{a\log(1/\delta)}{\delta} - \frac{a}{z} - 2bz + \frac{b(1-\delta^2)}{\delta}\right]^2 dz \tag{2.44}$$

$$= \; a'^2\frac{\delta^5}{5} + 2a'b'\frac{\delta^5}{5} + b'^2\frac{\delta^5}{5} + O\left(\delta^5\log(1/\delta)\right) \tag{2.45}$$

as $\delta \to 0$. Comparing this with (2.43) we see that the minimal requirement for Q to remain positive in the $\delta \to 0$ or $\mathrm{R} \to \infty$ limit is

$$\frac{8}{\mathrm{R}} \sim a'\frac{\delta^4\left[\log(1/\delta)\right]}{5} + 2b'\frac{\delta^4\log(1/\delta)}{5} + \frac{b'^2}{a'}\frac{\delta^4\log(1/\delta)}{5} \tag{2.46}$$

$$\Rightarrow \quad \frac{1}{\mathrm{R}} \sim \frac{\xi(a',b')}{4}\delta^4\log(1/\delta) \tag{2.47}$$

where

$$\xi(a',b') = \frac{(a'+b')^2}{10a'}. \tag{2.48}$$

This yields the scaling of the boundary layer thickness as

$$\delta \sim \left[\xi(a',b')\mathrm{R}\log(\mathrm{R})\right]^{-1/4}. \tag{2.49}$$

The average temperature is bounded by two times (2.27) minus (2.28) implying that, asymptotically,

$$\langle T\rangle \;\geq\; \frac{4}{3}b'\delta - a'^2\delta - 2a'b'\delta - b'^2\delta \tag{2.50}$$

$$\sim \; \left(\frac{4}{3}b' - a'^2 - 2a'b' - b'^2\right)\xi(a',b')^{-1/4}\left(\mathrm{R}\log(\mathrm{R})\right)^{-1/4}. \tag{2.51}$$

To obtain the 'best' prefactor, we maximize over a' and b' to achieve

$$\langle T\rangle \geq \frac{2^{3/4}5^{1/4}}{6}\left(\mathrm{R}\log(\mathrm{R})\right)^{-1/4} \sim 0.419\left(\mathrm{R}\log(\mathrm{R})\right)^{-1/4} \tag{2.52}$$

where the optimal prefactor is obtained for $a' = \frac{1}{16}$ and $b' = \frac{7}{16}$.

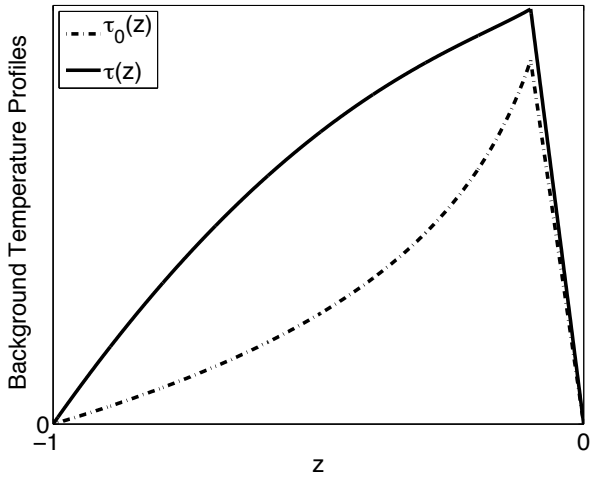

Figure 2.3: The background profile (2.26) where a and b scale in the optimal sense compared to the logarithmic profile given by (2.53).

2.4 Discussion and conclusions

The background profile (2.26) can be considered the sum of a singular logarithmic profile and a smooth conduction-like quadratic profile. If the logarithmic term only is considered, i.e., $b = 0$, then the profile would be

$$\tau_0(z) = \begin{cases} a \log\left(\frac{-1}{z}\right) & -1 \le z \le -\delta \\ -\frac{a \log(1/\delta) z}{\delta} & -\delta \le z \le 0. \end{cases} \tag{2.53}$$

This would be analogous to the approach taken in Doering et al. (2006) for boundary driven convection. However if the same steps are followed, the optimal estimate occurs for $a \sim \frac{\delta}{[\log(1/\delta)]^2}$ in which case the bound becomes

$$\langle T \rangle \ge \frac{\delta}{[\log(1/\delta)]^2}. \tag{2.54}$$

This is a weaker result than that derived above. However, the same analysis performed to ensure the positivity of Q, but with (2.53) as the background profile yields the 'pure' boundary layer thickness scaling $\delta \sim \mathrm{R}^{-1/4}$.

Fig. 2.3 yields further insight. The purely logarithmic profile (2.53) (the dashed line) yields a thicker boundary layer at high R because the steep gradient near

$z = 0$ enhances the positivity of Q sufficiently to maintain the increased size of the boundary layer. But this costs dearly in the Dirichlet integral that negatively affects the estimate of $\langle \mathrm{T} \rangle$ while adding very little to the computation of $\langle \tau_0(z) \rangle$. That is, while the quadratic term ($b > 0$) thins the boundary layer, it also contributes significantly to $\langle \tau \rangle$ and raises the lower bound. In previous applications of the background method Doering et al. (2006); Doering and Constantin (2001); Otero et al. (2002) the scaling of the boundary layer dictates the bound: typically the heat transport is bounded by $\frac{1}{\delta}$ where δ is the size of the boundary layer. Bounding the average temperature from below for the internal heating problem creates a different situation where the 'optimal' boundary layer scaling in terms of δ yields an apparently sub-optimal bound in terms of R.

Another key difference between this problem and the traditional application of the background method to boundary driven Rayleigh-Bénard convection is the symmetry of the problem. In purely boundary driven convection in the Boussinesq approximation, the system is naturally symmetric in the vertical (across the mid-plane of the layer) so the optimal choice of background profile is symmetric as well. Indeed, in that case thermal boundary layers near both the bottom and top boundaries are unstably stratified. In the case of an internal heat source there is an inherent asymmetry: the (horizontally and time averaged) vertical temperature profile throughout the bulk is stably stratified toward the bottom of the layer and unstably stratified only near the top.

The lower bound on the mean temperature (2.52) is remarkably close to the scaling derived from the marginally stable boundary layer argument, and it is not inconsistent with numerical simulations Sotin and Labrosse (1999) although we reiterate that the simulations employed stress-free (a.k.a. free-slip) boundary conditions on

the velocity, as opposed to the no-slip conditions employed here, that may affect the scaling behavior. The stress-free internal heating problem is addressed in Chapter IV (and in Whitehead and Doering (2011a)), where it is shown that $\langle T \rangle \gtrsim \mathrm{R}^{-5/17}$ or dimensionally $\langle \mathcal{T} \rangle \gtrsim \mathcal{H}^{12/17}$. It will also be of interest to examine numerical solutions of the Euler-Lagrange equations for this problem, as has been done for boundary driven Rayleigh-Bénard convection for finite Plasting and Kerswell (2003) and infinite Ierley et al. (2006) Prandtl numbers. Their solution would indicate what the true optimal background profile is, and may provide additional insight into the pursuit of further rigorous bounds.

The results of this Chapter are reported in Whitehead and Doering (2011a).

CHAPTER III

"Ultimate state" of two-dimensional convection between slippery (stress-free) boundaries

3.1 Introduction

As discussed in previous Chapters, Rayleigh-Bénard convection is the buoyancy-driven flow of a fluid heated from below and cooled from above. It is important for a variety of systems in the engineering, geophysical, and astrophysical sciences, and it has long served as a fundamental paradigm of nonlinear science, chaos, and pattern formation. Indeed, the Boussinesq approximation to the Navier-Stokes equations with the boundary conditions analyzed in this Chapter was Rayleigh's original model for calculating conditions for onset Rayleigh (1916), it is the basis of the Lorenz equations Lorenz (1963), and it formed the foundation of developments in the modern mathematical theory of amplitude Malkus and Veronis (1958) and modulation Newell and Whitehead (1969) equations. Most recently Rayleigh-Bénard convection has been the focus of a large body of experimental, computational, theoretical, and mathematical research aimed at characterizing the fully turbulent dynamics for application in geophysical and astrophysical regimes Ahlers et al. (2009).

Convective fluid flow increases vertical heat transport beyond the purely conductive flux. The dimensionless enhancement factor, the Nusselt number Nu (defined by (1.26)), is both of fundamental interest for applications and the natural and widely

recognized measure of the intensity and effectiveness of the motion. The most basic question for Rayleigh-Bénard convection is the dependence of Nu on (i) the strength of the thermal forcing, commonly expressed in terms of a dimensionless Rayleigh number Ra, (ii) the material properties of the fluid, which within the Boussinesq approximation is set by the dimensionless Prandtl number Pr, the ratio of the fluid's momentum and thermal diffusion coefficients, (iii) the geometry, typically the aspect ratio of the container, and (iv) the boundary conditions. The connection between these variables is generally complex and often not even unique, but in the "ultimate" high Rayleigh number regime when the flow is turbulent, the presumed functional relation between the Nu, Pr, and Ra is $\mathrm{Nu} \sim \mathrm{Pr}^{\gamma}\,\mathrm{Ra}^{\beta}$.

Experiments and simulations with $\mathrm{Pr} = \mathcal{O}(1)$ and *no-slip* boundary conditions suggest a scaling exponent $0.27 \lesssim \beta \lesssim 0.40$ at the highest available Ra Ahlers et al. (2009); Roche et al. (2010). Various theories suggest (modulo possible logarithmic corrections) that $\mathrm{Nu} \sim \mathrm{Pr}^{1/2}\,\mathrm{Ra}^{1/2}$ as $\mathrm{Ra} \to \infty$ Kraichnan (1962); Spiegel (1971); Grossman and Lohse (2000). Rigorous analyses of the Boussinesq model with no-slip velocity and isothermal (fixed temperature) Howard (1963); Doering and Constantin (1996) or fixed heat flux Otero et al. (2002) or mixed temperature Wittenberg (2010) boundary conditions yield upper bounds of the form $\mathrm{Nu} \leq c\,\mathrm{Ra}^{1/2}$ with prefactors $0 < c < \infty$ independent of Pr, so $\beta = \frac{1}{2}$ and $\gamma = \frac{1}{2}$ cannot both hold for very large Pr. The Nu-Ra relation is certainly different for *no-slip* boundaries at $\mathrm{Pr} = \infty$ where theory suggests Malkus (1954) and analysis proves Doering et al. (2006) (modulo possible logarithmic corrections) that $\mathrm{Nu} \lesssim \mathrm{Ra}^{1/3}$.

Two dimensional Rayleigh-Bénard convection displays many of the physical and turbulent transport features of three dimensional convection and has long been utilized as a test-bed for theoretical concepts DeLuca et al. (1990); Johnston and Do-

ering (2009). The effect of free-slip (no-stress) velocity boundary conditions on developed turbulent convection has largely been unexplored although we note that the rigorous scaling bound reported here was anticipated by recent numerical and perturbative investigations of transport limits for finite Otero (2002) and infinite Ierley and Worthing (2001); Ierley et al. (2006) Prandtl numbers. This Chapter bridges that gap with a proof that $\mathrm{Nu} \leq 0.2891\, Ra^{5/12}$ uniformly in $0 < \mathrm{Pr} \leq \infty$ for the Boussinesq model in two spatial dimensions with fixed temperature and free-slip boundaries. For continuity of the argument, the methodology is developed first for the case of internal heating driven convection (see Chapter II) in two dimensions for which we obtain the bound $\langle T \rangle \geq 0.7198\mathrm{R}^{-5/17}$, and then applied to the Rayleigh Bénard problem. The result for boundary driven convection refutes predictions of a $\mathrm{Nu} \sim Ra^{1/2}$ ultimate regime insofar as the theoretical arguments do not refer specifically to the boundary conditions or the spatial dimension. This issue is discussed further in the conclusion section at the end of the Chapter. Meanwhile the proof of the bound is presented in sufficient detail immediately below for motivated readers to reproduce the calculation in its entirety. The key new idea used to derive the result emerged from intuition developed in numerical studies of upper bounds Ierley and Worthing (2001); Otero (2002): implement and exploit the bulk averaged enstrophy balance available for two-dimensional flows with free-slip boundaries to decrease the upper bound, or increase the lower bound in the case of internal heating.

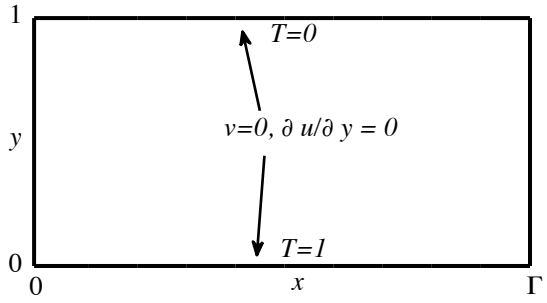

Figure 3.1: Geometry for the 2d stress-free convection problem. Boundary conditions for T, u, v, and the vorticity ω at the isothermal no-slip vertical boundaries are shown. All these variables as well as the pressure p are periodic in the horizontal direction with period Γ.

3.2 Boussinesq equations and energy identities

The dimensionless equations of motion for the Boussinesq approximation are

$$\frac{1}{\mathrm{Pr}}\left(\frac{\partial \boldsymbol{u}}{\partial t} + \boldsymbol{u}\cdot\nabla\boldsymbol{u}\right) + \nabla p = \nabla^2\boldsymbol{u} + \mathrm{Ra}\,\hat{\boldsymbol{j}}\,T, \tag{3.1}$$

$$\nabla\cdot\boldsymbol{u} = 0, \tag{3.2}$$

$$\frac{\partial T}{\partial t} + \boldsymbol{u}\cdot\nabla T = \nabla^2 T, \tag{3.3}$$

where the Prandtl number $\mathrm{Pr} = \nu/\kappa$ is the ratio of the fluid's kinematic viscosity ν to its thermal diffusivity κ, and the Rayleigh number $\mathrm{Ra} = g\,\alpha\,\Delta T\,h^3/\nu\,\kappa$ where g is the acceleration of gravity, α is the fluid's thermal expansion coefficient, and ΔT is the imposed temperature drop across the layer of thickness h. Lengths are measured in units of h, time in units of h^2/κ, and temperature in units of ΔT. The velocity vector field $\boldsymbol{u}(x,y,t) = \hat{\boldsymbol{i}}u(x,y,t) + \hat{\boldsymbol{j}}v(x,y,t)$ satisfies no-penetration and free-slip (stress-free) boundary conditions, and the temperature field $T(x,y,t)$ is isothermal on the vertical boundaries at $y = 0$ and $y = 1$ as shown in Fig. 3.1. All dependent variables, u, v, T, and the pressure field $p(x,y,t)$, are periodic in the horizontal direction x with period Γ (the aspect ratio).

As described in Chapter II the dimensional system for convection driven by inter-

nal heating is only slightly different, and in fact the only change to the dimensionless equations is to replace (3.3) with

$$\frac{\partial T}{\partial t} + \boldsymbol{u} \cdot \nabla T = \nabla^2 T + 1, \tag{3.4}$$

where $T = 0$ is satisfied at the top ($y = 0$) and bottom ($y = -1$) boundaries in this case.

Taking the curl of (6.1) one obtains the evolution equation for the scalar vorticity $\omega = \partial v/\partial x - \partial u/\partial y$,

$$\frac{1}{\mathrm{Pr}}\left(\frac{\partial \omega}{\partial t} + \boldsymbol{u} \cdot \nabla \omega\right) = \nabla^2 \omega + \mathrm{Ra}\,\frac{\partial T}{\partial x}. \tag{3.5}$$

The boundary conditions on u and v imply that $\omega = 0$ on the vertical boundaries at $y = 0$ and $y = 1$.

The goal of the analysis is to use the equations of motion to derive upper bounds on the Nusselt number defined as $\mathrm{Nu} = 1 + \langle vT \rangle$ or lower bounds on the averaged temperature $\langle T \rangle$, where $\langle \cdot \rangle$ represents the spatial and long time average, in terms of Ra, Pr, and Γ. Toward this end we utilize the background method Doering and Constantin (1992), a mathematical device introduced by Hopf to establish the existence of weak solutions to the Navier-Stokes equations in bounded domains Hopf (1940). For convection problems the background method involves decomposing the temperature field into a background profile $\tau(y)$ which satisfies the vertical boundary conditions ($\tau(0) = 1$ and $\tau(1) = 0$) and a perturbation term $\theta(x, y, t)$ satisfying corresponding homogeneous boundary conditions ($\theta(x, 0, t) = 0 = \theta(x, 1, t)$) so that $T(x, y, t) = \tau(y) + \theta(x, y, t)$ Doering and Constantin (1996). Implementing this decomposition the temperature equation (3.3) implies

$$\frac{\partial \theta}{\partial t} + \boldsymbol{u} \cdot \nabla \theta = \nabla^2 \theta + \tau''(y) - v\tau'(y) \tag{3.6}$$

for boundary driven convection, and (3.4) implies

$$\frac{\partial\theta}{\partial t} + \boldsymbol{u}\cdot\nabla\theta = \nabla^2\theta + \tau''(y) - v\tau'(y) + 1 \tag{3.7}$$

for convection driven by internal heating. Then the equations of motion together with the boundary conditions and the background decomposition imply

$$\frac{1}{2\,\mathrm{Pr}}\frac{d}{dt}\|\boldsymbol{u}\|_2^2 = -\|\omega\|_2^2 + \mathrm{Ra}\int v\,\theta\,dxdy \tag{3.8}$$

$$\frac{1}{2\,\mathrm{Pr}}\frac{d}{dt}\|\omega\|_2^2 = -\|\nabla\omega\|_2^2 + \mathrm{Ra}\int \omega\,\frac{\partial\theta}{\partial x}\,dxdy \tag{3.9}$$

$$\|\nabla T\|_2^2 = \|\nabla\theta\|_2^2 + 2\int \tau'\frac{\partial\theta}{\partial y}dxdy + \|\tau'\|_2^2 \tag{3.10}$$

and for boundary driven convection,

$$\frac{1}{2}\frac{d}{dt}\|\theta\|_2^2 = -\|\nabla\theta\|_2^2 - \int\left[\tau'\frac{\partial\theta}{\partial y} + \tau' v\theta\right]dxdy \tag{3.11}$$

or for internal heating,

$$\frac{1}{2}\frac{d}{dt}\|\theta\|_2^2 = -\|\nabla\theta\|_2^2 - \int\left[\tau'\frac{\partial\theta}{\partial y} + \tau' v\theta + \theta\right]dxdy \tag{3.12}$$

where $\|\cdot\|_2$ is the L^2 norm on the spatial domain and the elementary identity $\|\nabla\boldsymbol{u}\|_2^2 = \|\omega\|_2^2$ was used in (3.8), and $\mathrm{Ra}\to\mathrm{R}$ for internal heating. For internal heating we also require the following identities (derived modulo time-averaging in Chapter II for the no-slip infinite Pr problem):

$$\int \tau' w\theta dxdy = -\int|\nabla\theta|^2 dxdy - \int\tau'\frac{\partial\theta}{\partial y}dxdy + \int\theta dxdy \tag{3.13}$$

$$-\int \tau' w\theta dxdy = -\int\tau'\frac{\partial\theta}{\partial y}dxdy + \int\tau dxdy - \int(\tau')^2 dxdy. \tag{3.14}$$

3.3 The background method applied to internal heating

As in Chapter II we can combine (3.13) and (3.14), taking the long time average—remarking that it can be shown within the background method that the time averages

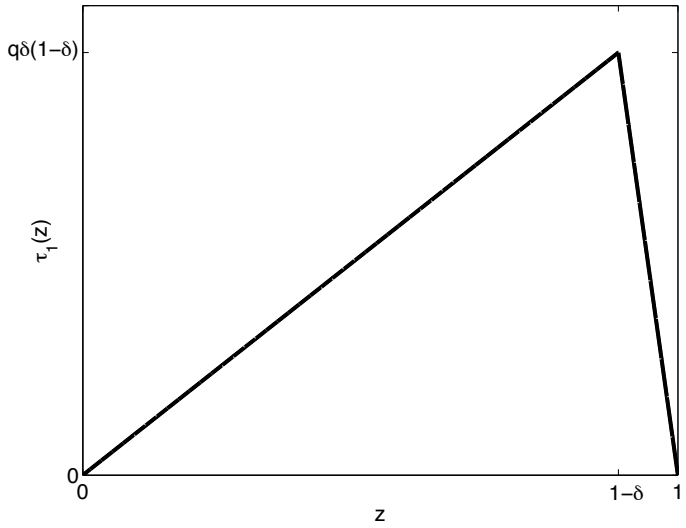

Figure 3.2: The background temperature profile for internal heating driven convection.

of the time derivatives vanish Doering and Constantin (1992, 1996)—and dividing by the aspect ratio Γ to see that

$$\langle T\rangle = \langle\theta\rangle + \langle\tau\rangle = 2\langle\tau\rangle - \langle(\tau')^2\rangle + \langle|\nabla\theta|^2\rangle + 2\langle\tau' v\theta\rangle. \tag{3.15}$$

Once again considering the long time average (and dividing by Γ), consider

$$(3.15) - 2\frac{q\delta}{\mathrm{R}} \times (3.8) - \frac{a\delta^{1/2}}{\mathrm{R}^{3/2}} \times (3.9) \tag{3.16}$$

where q and a are absolute constants to be determined later, and $\delta = \delta(\mathrm{R})$ is the size of the boundary layer as shown in Fig. 3.2. When the dust clears we arrive at

$$\langle T\rangle \;=\; 2\langle\tau\rangle - \langle(\tau')^2\rangle + \mathcal{Q} \tag{3.17}$$

where

$$\mathcal{Q} := \langle|\nabla\theta|^2\rangle + 2\langle[\tau' - q\delta]\, v\theta\rangle + \frac{q\delta}{\mathrm{R}}\langle|\omega|^2\rangle + \frac{a\delta^{1/2}}{\mathrm{R}^{3/2}}\langle|\nabla\omega|^2\rangle - \frac{a\delta^{1/2}}{\mathrm{R}^{1/2}}\left\langle\omega\frac{\partial\theta}{\partial x}\right\rangle. \tag{3.18}$$

Hence *if* we can choose the background profile $\tau(y)$ and coefficients $q > 0$ and $b > 0$ so that $\mathcal{Q} \geq 0$ for all relevant θ, ω and v, *then* we have the following lower

bound on the average temperature

$$\langle T\rangle \geq 2\langle\tau\rangle - \langle(\tau')^2\rangle. \tag{3.19}$$

For the problem at hand we will use the piece-wise linear profile shown in Fig. 3.2 where the thickness of the "boundary layer" is to be determined as a function of R to ensure that $\mathcal{Q} \geq 0$. With this choice of $\tau(y)$ the bound becomes

$$\langle T\rangle \geq q\delta(1-\delta)(1-q-2\delta) \sim q(1-q)\delta. \tag{3.20}$$

Similar to the approach used in Chapter II consider the horizontal Fourier transform, and using the shorthand $D = \frac{d}{dy}$, it is evident that the positivity of $\mathcal{Q}$ is equivalent to maintaining the positivity of

$$\begin{aligned}
\mathcal{Q}_k &= \|D\hat{\theta}_k\|^2 + k^2\|\hat{\theta}_k\|^2 + \frac{a\delta^{1/2}}{\mathrm{R}^{3/2}}\|D\hat{\omega}_k\|^2 \\
&+ \frac{q\delta}{\mathrm{R}}\|\hat{\omega}_k\|^2 + k^2\frac{a\delta^{1/2}}{\mathrm{R}^{3/2}}\|\hat{\omega}_k\|^2 \\
&+ \mathrm{Re}\left\{2\int_0^1 [\tau' - q\delta]\,\hat{v}_k\hat{\theta}_k^* dy - \frac{a\delta^{1/2}\imath k}{\mathrm{R}^{1/2}}\int_0^1 \hat{\omega}_k\hat{\theta}_k^* dy\right\}
\end{aligned} \tag{3.21}$$

for each horizontal wavenumber k where $\|\cdot\|$ is now the L^2 norm on complex valued functions of $y \in [-1, 0]$ and $\mathrm{Re}\{\cdot\}$ indicates the real part of a complex quantity. The Cauchy-Schwarz and Young inequalities imply

$$\left|\frac{a\delta^{1/2}\imath k}{\mathrm{R}^{1/2}}\int_0^1 \hat{\omega}_k\hat{\theta}_k^* dy\right| \leq \frac{a^2\delta}{4\mathrm{R}}\|\hat{\omega}_k\|^2 + k^2\|\hat{\theta}_k\|^2 \tag{3.22}$$

so dropping the manifestly non-negative term $\|D\hat{\omega}_k\|^2$,

$$\mathcal{Q}_k \geq \|D\hat{\theta}_k\|^2 + \left[\frac{a\delta^{1/2}k^2}{\mathrm{R}^{3/2}} + \frac{\delta}{\mathrm{R}}\left(q - \frac{a^2}{4}\right)\right]\|\hat{\omega}_k\|^2 - q\mathrm{Re}\left\{\int_{1-\delta}^1 \hat{v}_k\hat{\theta}_k dy\right\}.$$

Restricting $a^2 < 4q$, the task is to dominate the indefinite boundary layer integrals by the positive definite terms.

The Fourier coefficients of the vertical velocity and vorticity (suppressing the time dependence) are related by

$$ik\ \hat{\omega}_k(y) = D^2\hat{v}_k(y) - k^2\hat{v}_k(y). \tag{3.23}$$

Integrating the modulus squared of both sides with a simple integration by parts implies

$$k^2\|\ \hat{\omega}_k\|_2^2 = \|D^2 v_k\|^2 + 2k^2\|Dv_k\|^2 + k^4\|v_k\|^2. \tag{3.24}$$

On the other hand, integration by parts and the Cauchy-Schwarz and Young inequalities yield

$$\frac{2}{3}k^2\|D\hat{v}_k\|^2 \ \leq\ \frac{1}{9}\|D^2\hat{v}_k\|_2^2 + k^4\|\hat{v}_k\|^2 \tag{3.25}$$

so that, combining (3.24) and (3.25),

$$k^2\|\hat{\omega}_k\|_2^2 \geq \frac{8}{9}\|D^2\hat{v}_k\|^2 + \frac{8}{3}k^2\|D\hat{v}_k\|^2. \tag{3.26}$$

Boundary conditions on $\hat{v}_k(y)$ dictate that

$$\int_0^1 \mathrm{Re}\left\{D\hat{v}_k(y)\right\} dy = \left.\mathrm{Re}\left\{\hat{v}_k(y)\right\}\right|_{y=-1}^{y=0} = 0 \tag{3.27}$$

so $\exists\ y_0 \in (0,1)$ such that $\mathrm{Re}\left\{D\hat{v}_k(y_0)\right\} = 0$. The fundamental theorem of calculus followed by application of the Cauchy-Schwarz and Young inequalities imply

$$\begin{aligned}\left(\mathrm{Re}\left\{D\hat{v}_k(y)\right\}\right)^2 &= 2\int_{y_0}^{y} \mathrm{Re}\left\{D^2\hat{v}_k(y')\right\}\mathrm{Re}\left\{D\hat{v}_k(y')\right\} dy' \\ &\leq\ \tfrac{\sqrt{27}}{8k}\left(\tfrac{8}{9}\|\mathrm{Re}\left\{D^2\hat{v}_k\right\}\|^2 + \tfrac{8}{3}k^2\|\mathrm{Re}\left\{D\hat{v}_k\right\}\|^2\right).\end{aligned} \tag{3.28}$$

A similar pointwise bound holds for the imaginary part of $D\hat{v}_k(y)$ so its modulus squared satisfies

$$\begin{aligned}|D\hat{v}_k(y)|^2 &\leq\ \tfrac{\sqrt{27}}{8k}\left(\tfrac{8}{9}\|D^2\hat{v}_k\|^2 + \tfrac{8}{3}k^2\|D\hat{v}_k\|^2\right) \\ &\leq \tfrac{3^{3/2}}{8}k\|\ \hat{\omega}_k\|^2.\end{aligned} \tag{3.29}$$

Thus, integrating $D\hat{v}_k$ from y to 1 and applying Hölder's inequality, it is evident that

$$|\hat{v}_k(y)| \leq \frac{3^{3/4}}{2^{3/2}}\, k^{1/2}\,(1-y)\,\|\,\hat{\omega}_k\|. \tag{3.30}$$

Because $\theta(1) = 0$, (2.40) holds here (with $z \to y$), i.e.

$$|\hat{\theta}_k(y)| \leq |y|^{1/2}\|D\hat{\theta}_k\|. \tag{3.31}$$

Using these estimates, we conclude

$$q\left|\int_{1-\delta}^{1} \hat{v}_k(y)\hat{\theta}_k^*(y)dy\right| \leq \frac{3^{3/2}}{5^2\times 2^2}kq^2\delta^5\|\hat{\omega}_k\|^2 + \|D\hat{\theta}_k\|^2. \tag{3.32}$$

Hence

$$\mathcal{Q}_k \geq \left[\frac{a\delta^{1/2}k^2}{\mathrm{R}^{3/2}} + \frac{\delta}{\mathrm{R}}\left(q - \frac{a^2}{4}\right) - \frac{3^{3/2}}{5^2\times 2^2}kq^2\delta^5\right]\|\hat{\omega}_k\|^2 \tag{3.33}$$

so that positivity of $\mathcal{Q}_k$ (and hence $\mathcal{Q}$) is guaranteed if this term in front of $\|\hat{\omega}_k\|^2$ is non-negative. This becomes

$$\frac{3^{3/2}}{5^2\times 2^2}q^2\delta^4 \;\;\leq\;\; \frac{ak}{\delta^{1/2}\mathrm{R}^{3/2}} + \frac{1}{k\mathrm{R}}\left(q - \frac{a^2}{4}\right). \tag{3.34}$$

Minimizing the right hand side of (3.34) with respect to k yields

$$\frac{3^{3/2}}{5^2\times 2^2}q^2\delta^4 \leq 2\frac{a^{1/2}}{\delta^{1/4}\mathrm{R}^{5/4}}\left(q - \frac{a^2}{4}\right)^{1/2} \tag{3.35}$$

where

$$k = \frac{\delta^{1/4}\mathrm{R}^{1/4}}{a^{1/2}}\left(q - \frac{a^2}{4}\right)^{1/2} \tag{3.36}$$

is the minimizing wavenumber. It follows that the optimal choice of δ corresponds to

$$\delta \sim \frac{2^{12/17}\times 5^{8/17}\times a^{2/17}}{3^{6/17}\times q^{8/17}}\left(q - \frac{a^2}{4}\right)^{2/17}\frac{1}{\mathrm{R}^{5/17}}. \tag{3.37}$$

Plugging this into (3.20) and optimizing over a and q we arrive at

$$\langle T \rangle \geq \frac{2^{40/17} \times 3^{3/17} \times 5^{8/17} \times 17}{29^{29/17} \mathrm{R}^{5/17}} \sim 0.7198 \mathrm{R}^{-5/17} \tag{3.38}$$

where $a = \frac{4}{29^{1/2}}$ and $q = \frac{12}{29}$ are the optimal constants.

It is worth noting that this result is fundamentally different than that obtained for no-slip boundaries at infinite Prandtl number in Chapter II. The analysis performed here relies on uniform point-wise estimates on the vertical velocity, in terms of the enstrophy, while we employed singular integral inequalities in Chapter II. Another key difference is the appearance for this problem of the optimizing wavenumber $k \sim \mathrm{R}^{3/17}$ implicitly defined in (3.36). For no-slip boundaries, all the necessary bounds were uniform in the horizontal wavenumber, and there was no specific horizontal scale that came out of the analysis. It is of interest to consider whether this particular scale is of physical importance or not.

3.4 The background method applied to Rayleigh Bénard convection

The approach taken in the previous section lends itself readily to the problem of Rayleigh Bénard convection in 2 dimensions. An outline of the analysis is provided here, with appropriate analogy to the internal heating problem and the bounds derived in the previous section. This particular problem is of specific interest to the fluid dynamics community as the result obtained here invalidates a theoretical prediction of the "ultimate" regime of turbulent convection, unless this prediction is modified to consider 3 dimensions or no-slip boundaries.

As discussed in Chapter I, it is well-known that the equations of motion imply $\mathrm{Nu} = \langle |\nabla T|^2 \rangle$ Howard (1963); Doering and Constantin (1996). Thus, given coeffi-

cients a and b with precise values to be determined, then we can use

$$\frac{b}{\mathrm{Ra}} \times (3.8) + \frac{a}{\mathrm{Ra}^{3/2}} \times (3.9) + 2 \times (3.11) + (3.10), \tag{3.39}$$

taking the long time average, and dividing by Γ to write the Nusselt number as

$$\begin{aligned} Nu &= \left\langle -|\nabla\theta|^2 + (\tau')^2 + -2\tau' v\theta - \frac{b}{\mathrm{Ra}}|\omega|^2 \right. \\ &+ \left. bv\theta - \frac{a}{\mathrm{Ra}^{3/2}}|\nabla\omega|^2 + \frac{a}{\mathrm{Ra}^{1/2}}\omega\frac{\partial\theta}{\partial x} \right\rangle. \end{aligned} \tag{3.40}$$

Now we need the definition

$$\mathrm{Nu} = 1 + \langle vT \rangle = 1 + \langle v(\tau + \theta) \rangle = 1 + \langle v\theta \rangle \tag{3.41}$$

where the last identity is a result of the horizontal average, and τ being independent of x. Using this, and rearranging (3.40) we obtain

$$\mathrm{Nu} = \frac{1}{1-b}\left(\int_0^1 \tau'(y)^2 dy - b\right) - \frac{1}{1-b}\,\mathcal{Q} \tag{3.42}$$

where

$$\begin{aligned} \mathcal{Q} &= \left\langle |\nabla\theta|^2 \;+\; \frac{a}{\mathrm{Ra}^{3/2}}|\nabla\omega|^2 \;+\; \frac{b}{\mathrm{Ra}}|\omega|^2 \right. \\ &+ \left. 2\,\tau'\,v\,\theta \;+\; \frac{a}{\mathrm{Ra}^{1/2}}\omega\,\frac{\partial\theta}{\partial x} \right\rangle. \end{aligned} \tag{3.43}$$

As before, *if* we can choose the background profile $\tau(y)$ and coefficients $a > 0$ and $0 < b < 1$ so that $\mathcal{Q} \geq 0$ for all relevant θ, ω and v, *then* the first term on the right hand side of (4.14) is an upper bound on Nu. In this case we will use the piece-wise linear profile shown in Fig. 3.3 where the thickness δ of the "boundary layers" is to be determined as a function of Ra to satisfy $\mathcal{Q} \geq 0$. With this choice of $\tau(y)$ the bound will be

$$\mathrm{Nu} \leq \frac{1}{2\delta(1-b)} - \frac{b}{1-b}. \tag{3.44}$$

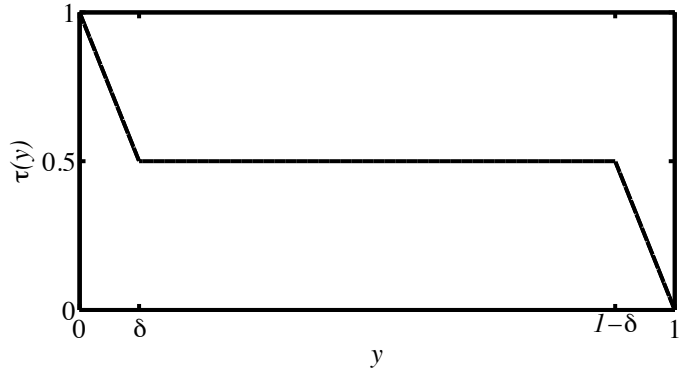

Figure 3.3: Background profile with boundary layers of thickness $0 < \delta \leq \frac{1}{2}$ in which $\tau'(y) = -\frac{1}{2\delta}$; $\tau'(y) \equiv 0$ for $\delta < y < 1 - \delta$.

Applying the horizontal Fourier transform and introducing the shorthand $D = \frac{d}{dy}$, it is evident that positivity of $\mathcal{Q}$ is equivalent to the positivity of

$$\begin{aligned} \mathcal{Q}_k &= \|D\hat{\theta}_k\|^2 + k^2\|\hat{\theta}_k\|^2 + \frac{a}{\mathrm{Ra}^{3/2}}\|D\hat{\omega}_k\|^2 \\ &\quad + \frac{a}{\mathrm{Ra}^{3/2}}k^2\|\hat{\omega}_k\|^2 + \frac{b}{\mathrm{Ra}}\|\hat{\omega}_k\|^2 \\ &\quad + \mathrm{Re}\left\{2\int_0^1 \tau'\,\hat{v}_k\,\hat{\theta}_k^* dy - \frac{aik}{\mathrm{Ra}^{1/2}}\int_0^1 \hat{\omega}_k\,\hat{\theta}_k^* dy\right\} \end{aligned} \tag{3.45}$$

for each horizontal wavenumber k where $\|\cdot\|$ is now the L^2 norm on complex valued functions of $y \in [0,1]$ and $\mathrm{Re}\{\cdot\}$ indicates the real part of a complex quantity. The Cauchy-Schwarz and Young inequalities imply

$$\left|\frac{a\,i\,k}{\mathrm{Ra}^{1/2}}\int_0^1 \hat{\omega}_k\hat{\theta}_k^* dy\right| \leq \frac{a^2}{4\mathrm{Ra}}\|\,\hat{\omega}_k\|^2 + k^2\|\hat{\theta}_k\|^2 \tag{3.46}$$

so dropping the manifestly non-negative term $\|D\hat{\omega}_k\|^2$,

$$\begin{aligned} \mathcal{Q}_k &\geq \|D\hat{\theta}_k\|^2 + \left[\frac{ak^2}{\mathrm{Ra}^{3/2}} + \frac{1}{\mathrm{Ra}}\left(b - \frac{a^2}{4}\right)\right]\|\,\hat{\omega}_k\|^2 \\ &\quad -\frac{1}{\delta}\,\mathrm{Re}\left\{\int_0^\delta \hat{v}_k(y)\hat{\theta}_k^*(y)dy + \int_{1-\delta}^1 \hat{v}_k(y)\hat{\theta}_k^*(y)dy\right\}. \end{aligned} \tag{3.47}$$

Restricting $a^2 < 4b$, the task is to dominate the indefinite boundary layer integrals by the positive definite terms.

The Fourier coefficients of the vertical velocity and vorticity (suppressing the time dependence) are related by (3.23) just as in the case of internal heating. Following the same arguments as the previous section, but now on the interval $y \in [0,1]$, and considering both boundaries, we see that:

$$|\hat{v}_k(y)| \leq \frac{3^{3/4}}{2^{3/2}}\, k^{1/2}\, y \parallel \hat{\omega}_k \parallel. \tag{3.48}$$

Likewise, integrating $D\hat{v}_k$ from $1-y$ to 1,

$$|\hat{v}_k(y)| \leq \frac{3^{3/4}}{2^{3/2}}\, k^{1/2}\, (1-y) \parallel \hat{\omega}_k \parallel. \tag{3.49}$$

We can also derive the following bounds just as before:

$$|\hat{\theta}_k(y)| \leq y^{1/2} \left(\int_0^{1/2} |D\hat{\theta}_k(y')|^2 dy' \right)^{1/2} \tag{3.50}$$

for $0 \leq y \leq 1/2$ and, for $1/2 \leq y \leq 1$,

$$|\hat{\theta}_k(y)| \leq (1-y)^{1/2} \left(\int_{1/2}^{1} |D\hat{\theta}_k(y')|^2 dy' \right)^{1/2}. \tag{3.51}$$

Using (3.48 - 3.51), we conclude

$$\begin{aligned} &\tfrac{1}{\delta} \left| \textstyle\int_0^\delta \hat{v}_k(y)\hat{\theta}_k^*(y)dy + \int_{1-\delta}^1 \hat{v}_k(y)\hat{\theta}_k^*(y)dy \right| \\ &\leq \tfrac{3^{3/2}}{5^2 \cdot 2^2}\, k\, \delta^3 \parallel \hat{\omega}_k \parallel^2 + \parallel D\hat{\theta}_k \parallel^2. \end{aligned} \tag{3.52}$$

Hence $\mathcal{Q}_k \geq 0$ is guaranteed by a δ small enough that

$$\frac{ak^2}{\mathrm{Ra}^{3/2}} + \frac{1}{\mathrm{Ra}} \left(b - \frac{a^2}{4} \right) - \frac{3^{3/2} k}{5^2 \cdot 2^2} \delta^3 \geq 0. \tag{3.53}$$

Inserting $a = \frac{2}{\sqrt{15}}$ and $b = \frac{1}{5}$ into (3.53)—chosen to minimize the prefactor in the bound—and minimizing the suitable δ over k, this is satisfied by choosing $\delta = \frac{2^{4/3} \cdot 5^{5/12}}{3^{3/4}} Ra^{-5/12}$ where $k = \frac{1}{3^{1/4} \cdot 5^{1/4}} \mathrm{Ra}^{1/4}$ is the minimizing wavenumber. Inserting these δ and b into (3.44) we see that for large Ra (actually for all $\mathrm{Ra} > \frac{27}{4}\pi^4$)

$$\mathrm{Nu} \;\leq\; \frac{5^{7/12} \cdot 3^{3/4}}{2^{13/3}} \mathrm{Ra}^{5/12} - \frac{1}{4} \;\lesssim\; 0.2891\, \mathrm{Ra}^{5/12}. \tag{3.54}$$

3.5 Discussion of the bound on Nu

The $\frac{5}{12}$ exponent for the Nu-Ra upper bound scaling, albeit with a prefactor 0.142, was conjectured by Otero from a numerical study nearly a decade ago Otero (2002). The proof here puts that result on firm analytical ground. The Nu-Ra *and* the distinguished horizontal wavenumber scaling $k \sim \mathrm{Ra}^{1/4}$ also agree with those conjectured by Ierley, Plasting, and Kerswell following a careful combination of numerical and asymptotic analyses of the upper bound problem for infinite Prandtl number Rayleigh-Bénard convection in *three* spatial dimensions with free-slip boundaries Ierley et al. (2006). In fact the analysis in this paper can be extended to that case because there is no vortex stretching at $\mathrm{Pr} = \infty$ so an enstrophy balance akin to (3.9) is realized for free-slip boundaries Whitehead and Doering (2011a).

While the rigorous bound $\beta \leq \frac{5}{12} \approx .4167$ for the model of Rayleigh-Bénard convection considered here is still well above that observed in most experiments and direct numerical simulations, it has significant ramifications from a theoretical point of view. There are several theoretical predictions of $\mathrm{Ra}^{1/2}$ scaling of the heat transport in the "ultimate" regime of asymptotically high Raleigh numbers Kraichnan (1962); Spiegel (1971); Grossman and Lohse (2000) and the result proved here shows that those arguments cannot be correct without plainly appealing to no-slip boundary conditions or directly relying on three dimensional dynamics (or both).

Perhaps the simplest scaling argument—making no mention of boundaries or boundary conditions or the spatial dimension—is the hypothesis that the physical heat transport is independent of the molecular transport coefficients, i.e., the kinematic viscosity ν and the thermal diffusivity κ, in the fully developed turbulent regime Spiegel (1971). This implies $\mathrm{Nu} \sim \mathrm{Pr}^{1/2}\,\mathrm{Ra}^{1/2}$. A more physically explicit

version of the argument proceeds from the assumption that the rate-limiting process is not transferring heat across boundary layers into the bulk, but rather is the time it takes to adiabatically transport hot and cold fluid elements across the layer accelerated by the reduced gravity $\alpha\Delta T g$ neglecting frictional forces. Then the vertical velocity scale of rising or falling elements is $\sqrt{g\alpha\Delta T h}$ and their heat content is $\mathcal{O}(\Delta T)$, so at sufficiently high density of such elements the heat flux is $\sim (g\alpha h)^{1/2}\Delta T^{3/2}$. When normalized by the conductive heat flux $\kappa\Delta T/h$, this again yields $\mathrm{Nu} \sim \mathrm{Pr}^{1/2}\,\mathrm{Ra}^{1/2}$.

More sophisticated arguments Kraichnan (1962); Grossman and Lohse (2000) produce the similar predictions. It has also been proposed that the $\frac{1}{2}$ exponents will appear if the physical boundary layers are negligible (as might be hypothesized when $\mathrm{Ra} \to \infty$) or absent altogether. This leads to the consideration of "homogeneous" Rayleigh-Bénard convection where the Boussinesq equations with a linear background profile are posed on a fully periodic domain. Direct numerical simulations in three dimensions and a closure theory have indicated that this scaling emerges for some aspect ratios Lohse and Toschi (2003); Garaud et al. (2010) although no upper bounds on the heat transport can possibly exist and the genuineness of statistical steady states is questionable for this formulation Calzavarini et al. (2006); Garaud et al. (2010).

The $\mathrm{Nu} \lesssim \mathrm{Ra}^{5/12}$ bound derived here raises questions of precisely how the spatial dimension and the nature of even very thin boundary layers enter into the problem at high Rayleigh numbers. At least in two dimensions with free-slip boundaries, no matter how high the Rayleigh number is it is apparent that boundary layers continue to play a limiting role in the turbulent heat transport.

The results of this Chapter are reported in Whitehead and Doering (2011b,c).

CHAPTER IV

Rigid rigorous bounds on heat transport in a slippery (stress-free) container at infinite Prandtl number

4.1 Introduction

As introduced in earlier Chapters, we consider the Boussinesq approximation for a fluid driven by buoyancy. In non-dimensional units the momentum and continuity equations are:

$$\frac{1}{\mathrm{Pr}}\left(\frac{\partial \boldsymbol{u}}{\partial t} + \boldsymbol{u}\cdot\nabla\boldsymbol{u}\right) + \nabla p = \nabla^2\boldsymbol{u} + \mathrm{R}\hat{\boldsymbol{k}}\mathrm{T} \tag{4.1}$$

$$\nabla\cdot\boldsymbol{u} = 0 \tag{4.2}$$

(4.3)

where R (Ra) the Rayleigh number, is a measure of the strength of the forcing (see Rayleigh (1916) and Roberts (1967)). Pr is the ratio of the kinematic viscosity to the thermal diffusivity. The fluid is constrained vertically by two plates a unit distance apart where we consider stress-free boundaries on the velocity field $\boldsymbol{u}$, and periodicity in the horizontal direction(s) for all variables. For boundary driven Rayleigh-Bénard convection (Ra), the temperature satisfies $T = 0$ at $z = 1$ and $T = 1$ at $z = 0$ giving a unit vertical temperature gradient and the evolution of the temperature is governed by

$$\frac{\partial \mathrm{T}}{\partial t} + \boldsymbol{u}\cdot\nabla\mathrm{T} = \nabla^2\mathrm{T}. \tag{4.4}$$

For details regarding the dimensionalization of this system, consider Otero (2002) and Chapter III.

We also consider internal heating driven convection (see Roberts (1967); Sparrow et al. (1963) and Chapter II), whereupon (4.2) and (6.1) are satisfied (where R is now referred to as the 'Rayleigh heat number' Sotin and Labrosse (1999); Roberts (1967)), but (4.4) becomes

$$\frac{\partial \mathrm{T}}{\partial t} + \boldsymbol{u} \cdot \nabla \mathrm{T} = \nabla^2 \mathrm{T} + 1. \tag{4.5}$$

Once again we will consider stress-free boundary conditions in the vertical for the velocity, but in order to maintain a mathematically tractable problem we consider isothermal boundary conditions, i.e. $T = 0$ at $z = 0, 1$.

Although convection driven by the enforced temperature gradient has been widely studied in the literature, inclusion of internal heating is a more realistic representation of the earth's mantle (see Sotin and Labrosse (1999)) and is applicable to the turbulence of plasmas in stars. In reality the motion of the earth's mantle is driven by radioactive decay (internal heat source) and extreme temperatures at the earth's core (bottom boundary). Convection in large stars is driven by unstable fusion in the core which can be modeled crudely by a constant internal heat source. In the interest of mathematical clarity we will consider either a constant internal heat source, or an imposed temperature gradient. Future investigations should consider the effect of both driving mechanisms, as well as more realistic temperature dependent heat sources.

The equations of motion for either the internal heating problem, or boundary forced convection are highly nonlinear, and tractable analytic solutions are rare, and typically trivial (see Doering and Gibbon (1995)). In highly turbulent regimes of as-

trophysical and geophysical interest (when the forcing term R or Ra is asymptotically large) turbulence sets in, and deterministic prediction of solutions becomes difficult, if not impossible (see Fefferman (2002)) in three dimensions. Instead, experiments, numerical simulations, theoretical simplifications, and analytic methods have focused on statistical quantities that reflect the supposed 'efficiency' of the underlying turbulence in the convection (see Ahlers et al. (2009) for a review of the current state of affairs for boundary driven convection). This Chapter focuses on rigorous bounds on these statistical quantities for both types of driving forces, and is meant to augment the previous Chapter in the investigation of the effects of stress-free boundaries on the transport of heat in convective turbulence.

This Chapter addresses two variations of convection constrained between slippery plates, deriving appropriate, rigid bounds for each. In both cases we will consider convection of the earth's mantle where $\mathrm{Pr} = O\left(10^{23}\right)$ so we assume (see Wang (2004) for a discussion of the validity of this limit) that $\mathrm{Pr} = \infty$ whereupon (6.1) becomes

$$\nabla p = \nabla^2 \boldsymbol{u} + \mathrm{R}\hat{\boldsymbol{k}}\mathrm{T}. \tag{4.6}$$

Unlike in Chapter III we make no restriction on the dimension of the problem, i.e. the results hold for both 2 and 3 dimensions, and we consider both boundary driven convection (4.4) and internal heating driven convection (4.5).

For (4.4) the enhancement of the transport of heat due to convection is measured by the nondimensional Nusselt number (see Otero (2002) and the previous Chapters for a complete derivation and discussion)

$$\mathrm{Nu} = 1 + \langle w\theta \rangle \tag{4.7}$$

where $\langle \cdot \rangle$ represents the spatial and long time average (we consider the limit supremum for the temporal average to avoid issues of regularity and existence of the limit).

For internal heating driven convection, as the forcing is increased ($\mathrm{R} \to \infty$) the flow becomes more turbulent, causing the temperature to be distributed uniformly across the layer, implying that $\langle T \rangle$ decreases (in the non-dimensional setting, see Chapter II for a discussion of the physical relevance and dimensional analogue for this problem). The functional relationship between $\langle T \rangle$ and R provides a measure of the transport of heat in this case.

It is well agreed that $\mathrm{Nu} \sim \mathrm{Ra}^{\gamma}$ for some exponent γ, and similarly it is accepted that $\langle T \rangle \sim \mathrm{R}^{-\beta}$, but the precise value of γ is a source of contention (see Ahlers et al. (2009)) as, to date experiments and numerical simulations do not agree (see Johnston and Doering (2009) and Ahlers (2009)). In addition, there are several theories proposed to determine the proper scaling of the Nusselt number for asymptotically large values of Ra (see Kraichnan (1962) and Malkus (1954) for two examples) which do not always agree with the experimental data or with state of the art numerical simulations. As pointed out in Chapter III, these theoretical simplifications do not rely on a specific set of boundary conditions, indicating that the change from stress-free to no-slip velocity boundaries should not affect the scaling of the Nusselt number. The bounds derived in this paper refute this assumption, indicating that the choice of stress-free boundaries significantly changes the possible scaling of the Nusselt number, at least at infinite Prandtl number. Convection driven by internal heating has not been investigated as thoroughly, but there still exist some fundamental arguments (see the beginning of Chapter II) that yield potential scaling laws for the bulk averaged temperature, and there has been some recent interest in direct numerical simulations for this problem (see Goluskin (2011); Cloutier et al. (2011)). The rigorous bounds found in this paper narrow the regime of possible exponents for both γ and β.

Previous work for boundary driven convection (see Doering et al. (2006), Ierley et al. (2006), and Doering and Constantin (1994)) and for internal heating driven convection (see Lu et al. (2004) and Chapter II) has primarily focused on no-slip velocity boundary conditions. While this is more comparable to experiments, it is not a realistic boundary condition for the earth's mantle (see Vatteville et al. (2009) and Sotin and Labrosse (1999)) and may not be realistic for convection in stars (viable for $\mathrm{Pr} < \infty$). Vitanov and Busse (see Vitanov and Busse (1997)) approach the stress-free problem using Howard's multi-wave expansion technique (see Howard (1963)), and some numerical considerations in Plasting and Ierley (2005) and Ierley et al. (2006) consider boundary driven convection for free-slip boundaries, but the internal heating problem has not been discussed. This Chapter is an extension of the framework developed in Chapter III to the 3 dimensional, infinite Prandtl number case, addressing free-slip boundary conditions, and putting a rigorous bound to the postulation of Ierley et al. (2006) that $\gamma = 5/12$, as well as deriving a rigorous bound of $\beta = 5/17$ for internal heating in 3d at infinite Pr.

The rest of this Chapter is outlined as follows. The following section introduces the so called background method, and demonstrates the equivalence of the inclusion of the balance parameter to a piece-wise linear background profile with stable stratification for Rayleigh Bénard convection at infinite Pr. Section 4.3 derives the scaling $\gamma = 5/12$ for the boundary driven convection at infinite Pr, and $\beta = 5/17$ for internal heating. Section 4.4 discusses the results of this work and the significance of these strict bounds on the understanding of turbulent convection.

4.2 The background method and piece-wise linear temperature profiles

4.2.1 General construction of the background method

As introduced in the previous Chapters, the background method is a mathematical tool used to derive a bounding principle on different statistically important properties in fluid flow. As before, we substitute the decomposition $T(x,y,z,t) = \tau(z) + \theta(x,y,z,t)$ into the equations of motion, and as in Chapter II we arrive at:

$$\nabla^4 w = -\mathrm{R}\nabla_H^2\theta \tag{4.8}$$

$$\frac{\partial\theta}{\partial t} + \boldsymbol{u}\cdot\nabla\theta = \nabla^2\theta + \tau'' - w\tau' \tag{4.9}$$

for boundary driven convection, and

$$\frac{\partial\theta}{\partial t} + \boldsymbol{u}\cdot\nabla\theta = \nabla^2\theta + \tau'' - w\tau' + 1 \tag{4.10}$$

for internal heating, where $\tau'(z) = \frac{d\tau(z)}{dz}$. With the help of standard energy identities, these equations allow us to rewrite Nu and $\langle T\rangle$ (see the previous two Chapters for details)

$$\mathrm{Nu} = \int_0^1 (\tau')^2\, dz - \mathcal{Q}_\tau(w,\theta) \tag{4.11}$$

$$\langle T\rangle = 2\int_0^1 \tau dz - \int_0^1 (\tau')^2\, dz + \mathcal{Q}_\tau(w,\theta) \tag{4.12}$$

where

$$\mathcal{Q}_\tau(w,\theta) = \langle|\nabla\theta|^2\rangle + \left\langle \int_0^1 w\theta\tau' dz \right\rangle. \tag{4.13}$$

This immediately lends to a bounding principle for both problems, i.e. if we can choose a background profile $\tau(z)$ so that $\mathcal{Q}_\tau$ is positive definite for all w,θ satisfying (4.8), then

$$\mathrm{Nu} \leq \int_0^1 (\tau')^2\, dz \tag{4.14}$$

$$\langle T\rangle \geq 2\int_0^1 \tau dz - \int_0^1 (\tau')^2\, dz. \tag{4.15}$$

To simplify the analysis, we apply the horizontal Fourier transform. For wavenumber $\mathbf{k}$ with $k = |\mathbf{k}|$, the Fourier coefficients $w_{\mathbf{k}}, \theta_{\mathbf{k}}$ of w and θ must satisfy

$$D^4\hat{w}_{\mathbf{k}} - 2k^2\hat{w}_{\mathbf{k}} + k^4\hat{w}_{\mathbf{k}} = \mathrm{R}k^2\hat{\theta}_{\mathbf{k}}, \tag{4.16}$$

where $D = \frac{d}{dz}$, and $\hat{w}_{\mathbf{k}}(z) = D^2\hat{w}_{\mathbf{k}}(z) = 0$ at $z = 0, 1$ for each $\mathbf{k}$ (due to incompressibility and the stress-free boundary conditions). Similarly each $\hat{\theta}_{\mathbf{k}}$ satisfies homogeneous Dirichlet boundary conditions. Ensuring the positivity of $\mathcal{Q}_\tau$ then reduces to verifying the following quadratic form is positive definite for all $\mathbf{k}$:

$$\hat{\mathcal{Q}}_\tau = \|D\hat{\theta}_{\mathbf{k}}\|_2^2 + k^2\|\hat{\theta}_{\mathbf{k}}\|_2^2 + 2\int_0^1 \tau' Re[\hat{w}_{\mathbf{k}}^*\hat{\theta}_{\mathbf{k}}]dz \tag{4.17}$$

where $\|\cdot\|_2$ is the standard L^2 norm with respect to integration in the vertical and $Re[f]$ is the real part of the complex valued function $f(z)$.

To simplify notation, we drop the subscript k from (4.16) and (4.17) so that ensuring that

$$\mathcal{Q} = \|D\theta\|_2^2 + k^2\|\theta\|_2^2 + 2\int_0^1 \tau' Re[w^*\theta]dz \geq 0 \tag{4.18}$$

where w and θ sastisfy

$$D^4 w - 2k^2 D^2 w + k^4 w = \mathrm{R}k^2\theta, \tag{4.19}$$

and the appropriate boundary conditions on $z \in [0, 1]$ are satisfied, guarantees (4.14) and (4.15). Thus the goal is to find $\tau(z)$ that will minimize (4.14) (or equivalently in this case, maximize (4.15)) while maintaining the 'spectral constraint' (4.18) over the fields $w(z),\ \theta(z)$ that satisfy (4.19).

4.2.2 Piecewise linear background profiles and the balance parameter in boundary driven convection.

As indicated in Chapter III, ensuring (4.18) would indicate that choosing $\tau' \sim 0$ is the optimal choice, with the required boundary conditions on $\tau(z)$ then introducing

boundary layers that are balanced with the l^2 norms of the temperature fluctuations $\theta(z)$. On the contrary, numerical simulations at infinite Prandtl number in Sotin and Labrosse (1999) indicate that the horizontally averaged temperature (akin to $\tau(z)$) for boundary driven convection, is not monotonic, and is stably stratified in the bulk. Numerical exploration of the background method applied to the boundary driven problem by Plasting and Ierley (2005) and Ierley et al. (2006) indicate that for free-slip it is indeed optimal to consider a family of background profiles so that $\tau'(z) \sim p > 0$ in the bulk (with appropriate matching boundary layers). Section 4.3.2 can be considered a rigorous proof of the bound obtained in Plasting and Ierley (2005), utilizing this family of background profiles. Section 4.3.3 uses the same $\tau(z)$ found in Fig. 3.2, only applied now to the 3d infinite Pr problem.

Using the family of background profiles introduced by Plasting and Ierley (2005) (with $\tau' = p$ in the bulk as given explicitly in (4.40)) one can show that (4.14) becomes

$$Nu \leq \frac{(1+p)^2}{2\delta} - p(2+p) \tag{4.20}$$

and (4.13) can be reformulated as

$$0 \leq \langle |\nabla\theta|^2 \rangle + p\langle w(z)\theta(z) \rangle - \frac{1+p}{\delta} \left\langle \left(\int_0^\delta w(z)\theta(z)dz + \int_{1-\delta}^1 w(z)\theta(z)dz \right) \right\rangle_H \tag{4.21}$$

where $\langle \cdot \rangle_H$ represents the horizontal and temporal average. Recall that in the infinite Pr limit, $w(z)$ and $\theta(z)$ are related via (4.8). Heuristically, one can suppose that

$$\theta(z) \sim \frac{1}{\mathrm{R}} \nabla^2 w, \tag{4.22}$$

and hence

$$\langle w\theta \rangle \sim \frac{1}{\mathrm{R}} \left\langle |\nabla w|^2 \right\rangle. \tag{4.23}$$

In a seemingly unrelated development to the introduction of the stably stratifying bulk term, Nicodemus et al. (1997) introduced the use of a 'balance parameter' $0 < b < 1$ to the variational formula that relies on an energy identity derived from (6.1) (which is valid in the infinite Pr limit) and an equivalent definition of Nu. This introduces an additional degree of freedom in the variational statement. Employing the balance parameter b (this is the same absolute constant b used in the derivation of the $\mathrm{Nu} \lesssim \mathrm{Ra}^{5/12}$ bound in the previous Chapter) with no stable stratification in the bulk of the flow leads to (see Otero et al. (2002) and Nicodemus et al. (1997) for details)

$$\mathrm{Nu} \quad \leq \quad \frac{1}{2(1-b)\delta} - \frac{b}{1-b} \tag{4.24}$$

where

$$\left\langle |\nabla\theta|^2 \right\rangle + \frac{b}{\mathrm{R}} \left\langle |\nabla \boldsymbol{u}|^2 \right\rangle \quad \geq \quad \frac{1}{\delta} \left\langle \int_0^\delta w(z)\theta(z)dz + \int_{1-\delta}^1 w(z)\theta(z)dz \right\rangle_H . \tag{4.25}$$

From the previous discussion, one quickly recognizes that these two formulations of $\mathcal{Q}_\tau$ are similar. To see this rigorously we consider the Fourier transformed version of the quadratic form (neglecting the k subscript and $\hat{\cdot}$ as before). Otero et al. (2002) showed that incompressibility implies that maintaining (4.25) is equivalent to showing that

$$\|D\theta\|_2^2 + k^2\|\theta\|_2^2 + \frac{b}{\mathrm{R}} \left(\frac{1}{k^2}\|D^2 w\|_2^2 + 2\|D^2 w\|_2^2 + k^2\|w\|_2^2 \right) \tag{4.26}$$

$$- \quad \frac{1}{\delta}\int_0^\delta Re[w^*(z)\theta(z)]dz - \frac{1}{\delta}\int_{1-\delta}^1 Re[w^*(z)\theta(z)]dz \geq 0. \tag{4.27}$$

For the stably stratified $\tau(z)$ absent the balance parameter, applying (4.19) to (4.21) and integrating by parts appropriately leads to

$$\|D\theta\|_2^2 + k^2\|\theta\|_2^2 + \frac{2p}{\mathrm{R}} \left(\frac{1}{k^2}\|D^2 w\|_2^2 + 2\|D^2 w\|_2^2 + k^2\|w\|_2^2 \right) \tag{4.28}$$

$$- \quad \frac{1+p}{\delta}\int_0^\delta Re[w^*(z)\theta(z)]dz - \frac{1+p}{\delta}\int_{1-\delta}^1 Re[w^*(z)\theta(z)]dz \geq 0. \tag{4.29}$$

The slight differences between these two formulations will not affect the scaling exponent (the prefactor on the bound of the Nusselt number may differ). In essence, including the balance parameter is equivalent to using a stable stratification in the form of a positive linear profile in the bulk of the background temperature field. This equivalence is not surprising, as the initial application of the background method to convection in Doering and Constantin (1996) made use of just such a non-monotonic background field $\tau(z)$, while Nicodemus et al. (1997) achieved the same scaling exponent via a monotonic $\tau(z)$ (with no stable stratification) by introducing the balance parameter. To illustrate the differences, this Chapter uses a non-monotonic background profile, rather than the balance parameter.

4.3 Bounds on convection

4.3.1 Necessary prerequisites at infinite Pr.

In analogy to the analysis performed in Chapter III, we formulate all terms in the quadratic form in terms of an enstrophy balance. This is valid, as solutions to the system (4.6),(4.2),(4.4) are known to be regular (see Wang (2004) and note that the change from (4.4) to (4.5) will not affect the regularity results). For infinite Pr the enstrophy balance is implicitly contained in the quadratic form due to the piecewise constraint (4.19) that, as observed above, indicates that

$$\langle|\nabla\theta|^2\rangle \sim \frac{1}{\mathrm{R}^2}\langle|\nabla^3 w|^2\rangle \gtrsim \frac{1}{\mathrm{R}^2}\langle|\nabla^2 w|^2\rangle \tag{4.30}$$

which is (via incompressibility) akin to the balance term in the conservation of enstrophy.

To make this rigorous, several estimates are required. This subsection details these estimates, paying particular attention to reformulating $\mathcal{Q}$ in terms of a pseudo-enstrophy, and its derivatives. The following two subsections apply the estimates to

the boundary driven and internal heating problem respectively to obtain the desired bounds for infinite Pr.

Recall that (4.19) holds for both boundary driven convection and internal heating. Motivated by the previous Chapter we introduce a 'pseudo-vorticity' ω such that

$$\left(D^2 - k^2\right) w = k\omega \tag{4.31}$$

$$\left(D^2 - k^2\right) \omega = k\mathrm{R}\theta. \tag{4.32}$$

The free-slip boundary conditions indicate that $w(z)$ and $D^2 w(z)$ both vanish at $z = 0, 1$, implying that $\omega(z)$ also vanishes at the boundaries. It was shown in Chapter III that (4.31) with the given boundary conditions on $w(z)$, indicate that

$$|w(z)| \leq \frac{3^{3/4}}{2^{3/2}} k^{1/2} z \|\omega\|_2 \tag{4.33}$$

and

$$|w(z)| \leq \frac{3^{3/4}}{2^{3/2}} k^{1/2} (1 - z) \|\omega\|_2. \tag{4.34}$$

Bounds on $\theta(z)$ are also derived using the Fundamental Theorem of Calculus and Cauchy Schwarz inequality, as

$$|\theta(z)| = \left| \int_0^z D\theta(z') dz' \right| \leq z^{1/2} \left(\int_0^z \left[D\theta(z') \right]^2 dz' \right)^{1/2} \leq z^{1/2} \|D\theta\|_2 \tag{4.35}$$

and

$$|\theta(z)| \leq (1 - z)^{1/2} \|D\theta\|_2. \tag{4.36}$$

Consider the Green's function $G(z, z')$ for (4.31) with the appropriate boundary conditions imposed. Careful consideration of (4.32) and the homogeneous boundary conditions on both $w(z)$ and $\omega(z)$ indicate that

$$\omega(z) = \mathrm{R} \int_0^1 G(z, z') \theta(z') dz', \tag{4.37}$$

so that a simple application of Fubini's theorem yields

$$\int_0^1 w^*(z)\theta(z)dz = \int_0^1 \int_0^1 G(z,z')\omega^*(z')\theta(z)dzdz' = \frac{1}{\mathrm{R}}\|\omega\|_2^2. \tag{4.38}$$

Finally, the relationship between $\omega(z)$ and $\theta(z)$ can be further exploited. Squaring (4.32) and integrating over the unit interval, we can verify that

$$k^2\mathrm{R}^2\|\theta\|_2^2 = \|D^2\omega\|_2^2 + 2k^2\|D\omega\|_2^2 + k^4\|\omega\|_2^2 \geq k^4\|\omega\|_2^2, \tag{4.39}$$

where the Dirichlet boundary conditions on $\omega(z)$ are essential to remove the boundary terms, i.e., this doesn't work for no-slip or rigid boundaries. As alluded to, (4.39) and (4.38) imply an 'enstrophy balance' in $\mathcal{Q}$ akin to that used in Chapter III. The analysis in the next two sections then proceeds, using (4.33), (4.35), (4.38), and (4.39), much as it did in the previous Chapter for two dimensional, finite Pr convection.

4.3.2 Boundary driven convection at infinite Pr.

We consider a background profile $\tau(z)$ that includes a stabilizing linear term in the bulk. For traditional Rayleigh Bénard convection driven by an imposed temperature gradient, this is

$$\tau_0(z) = \begin{cases} 1 - \left(\frac{1+p}{2\delta} - p\right) z & 0 \leq z \leq \delta \\ \frac{1}{2} + p\left(z - \frac{1}{2}\right) & \delta \leq z \leq 1-\delta \\ \left(\frac{1+p}{2\delta} - p\right)(1-z) & 1-\delta \leq z \leq 1 \end{cases} \tag{4.40}$$

as shown in Fig. 4.1. This leads to (4.20), with (4.18) becoming the need to keep

$$\mathcal{Q}_{RB} = \|D\theta\|_2^2 + k^2\|\theta\|_2^2 + 2p\int_0^1 Re[w^*(z)\theta(z)]dz \tag{4.41}$$

$$- \frac{1+p}{\delta}\int_0^\delta Re[w^*(z)\theta(z)]dz - \frac{1+p}{\delta}\int_{1-\delta}^1 Re[w^*(z)\theta(z)]dz \tag{4.42}$$

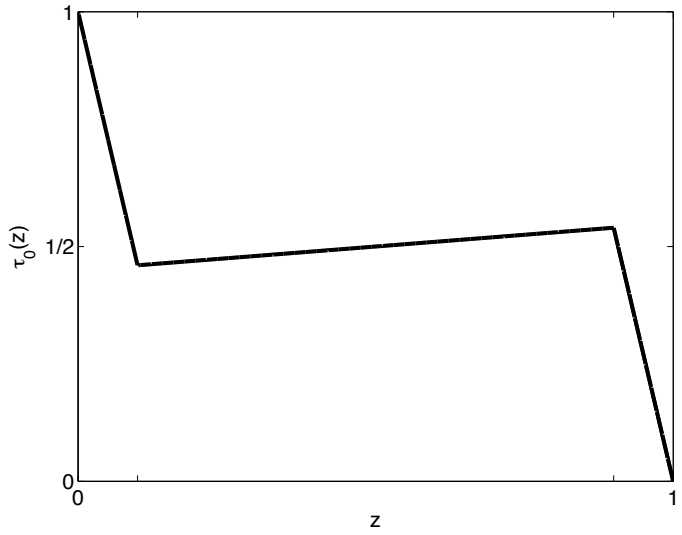

Figure 4.1: The background temperature profile for boundary driven convection at infinite Pr.

positive definite. To ensure this quantity remains nonnegative, first consider application of (4.38) and (4.39):

$$\begin{aligned} \mathcal{Q}_{RB} &\geq \|D\theta\|_2^2 + \left(\frac{k^4}{\mathrm{Ra}^2} + \frac{2p}{\mathrm{Ra}}\right)\|\omega\|_2^2 - \frac{1+p}{\delta}\int_0^\delta Re[w^*(z)\theta(z)]dz \\ &- \frac{1+p}{\delta}\int_{1-\delta}^1 Re[w^*(z)\theta(z)]dz. \end{aligned} \tag{4.43}$$

For the boundary layer integrals, we employ (4.33) and (4.35) in conjunction with Young's inequality to see that:

$$\frac{1+p}{\delta}\left|\int_0^\delta Re[w^*(z)\theta(z)]dz + \int_{1-\delta}^1 Re[w^*(z)\theta(z)]dz\right| \tag{4.44}$$

$$\leq \frac{(1+p)3^{3/4}\cdot 2^{1/2}k^{1/2}}{5}\delta^{3/2}\|\omega\|_2\|D\theta\|_2 \tag{4.45}$$

$$\leq \|D\theta\|_2^2 + \frac{3^{3/2}\cdot(1+p)^2}{2\cdot 5^2}k\delta^3\|\omega\|_2^2. \tag{4.46}$$

Inserting this back into (4.43), positivity of $\mathcal{Q}_{RB}$ is reduced to an algebraic expression requiring the positivity of the term involving the enstrophy $\|\omega\|_2^2$:

$$\left(\frac{k^4}{\mathrm{Ra}^2} + \frac{2p}{\mathrm{Ra}} - \frac{3^{3/2}\cdot(1+p)^2\cdot k}{2\cdot 5^2}\delta^3\right)\|\omega\|_2^2 \geq 0 \tag{4.47}$$

$$\Rightarrow \frac{3^{3/2}\cdot(1+p)^2}{2\cdot 5^2}\delta^3 \leq \frac{k^3}{\mathrm{Ra}^2} + \frac{2p}{k\mathrm{Ra}}. \tag{4.48}$$

Minimizing over the wavenumber k we see that this is equivalent to

$$\frac{3^{3/2}\cdot(1+p)^2}{2\cdot 5^2}\delta^3 \leq \frac{2^{11/4}\cdot p^{3/4}}{3^{3/4}\cdot \mathrm{Ra}^{5/4}} \tag{4.49}$$

$$\Rightarrow \delta \leq \frac{2^{5/4}\cdot 5^{2/3}\cdot p^{1/4}}{3^{3/4}\cdot(1+p)^{2/3}}\frac{1}{\mathrm{Ra}^{5/12}} \tag{4.50}$$

where the minimizing wavenumber is given by

$$k = \left(\frac{2p}{3}\mathrm{Ra}\right)^{1/4}. \tag{4.51}$$

Inserting this into (4.20),

$$Nu \leq \frac{3^{3/4}\cdot(1+p)^{8/3}}{2^{9/4}\cdot 5^{2/3}\cdot p^{1/4}}\mathrm{Ra}^{5/12} - p(2+p). \tag{4.52}$$

Optimizing the asymptotic prefactor over the slope parameter p we arrive at

$$\mathrm{Nu} \lesssim \frac{3^{1/2}\cdot 2^{133/12}}{5^{2/3}\cdot 29^{29/12}}\mathrm{Ra}^{5/12} \sim 0.3757\mathrm{Ra}^{5/12} \tag{4.53}$$

where $p = \frac{3}{29} \sim 0.1034$ is the 'optimal' slope.

The bound (4.53) compares favorably with that obtained in Chapter III where it was found that for 2d convection at arbitrary Pr, $\mathrm{Nu} \leq 0.2891\mathrm{Ra}^{5/12}$. The result here for infinite Pr was predicted through numeric and asymptotic analysis of variational bounds on the Nusselt number at infinite Prandtl number (see Plasting and Ierley (2005); Ierley et al. (2006)). It is of particular interest to compare this result to that obtained in Plasting and Ierley (2005) where the bound $\mathrm{Nu} \leq 0.1262\mathrm{Ra}^{5/12}$ was predicted by numerically solving the Euler-Lagrange equations arising from maintaining the positivity of $\mathcal{Q}_{RB}$ for a piece-wise linear background profile. (4.53) is reasonably close, and consistent with this result. More particularly, Plasting and Ierley (2005) (and verified by the more general analysis in Ierley et al. (2006)) found that the saturating wave-number for this problem occurred for $k \sim \mathrm{Ra}^{1/4}$ which is precisely the saturating wave-number found in (4.51). Even more surprising, and

perhaps indicative of the sharpness of the current result, the optimal slope p found in Plasting and Ierley (2005) was $p = 0.103$ agreeing (within three decimal places) with $p = \frac{3}{29} \sim 0.1034$.

4.3.3 Internal heating at infinite Pr.

Convection driven by internal heating with isothermal boundaries, unlike the boundary driven convection considered in the previous subsection, is not symmetric. As such, the chosen background profile has a single upper boundary layer:

$$\tau_1(z) = \begin{cases} q\delta z & 0 \le z \le 1-\delta \\ q(1-\delta)(1-z) & 1-\delta \le z \le 1 \end{cases}. \tag{4.54}$$

Plugging this into (4.15) we see that this gives a bound on the averaged temperature as

$$\langle T \rangle \le q\delta(1-\delta)(1-q-2\delta) \sim q(1-q)\delta \tag{4.55}$$

so long as $\mathcal{Q}_{IH}$ remains positive definite. This quickly reduces to the constraint

$$\|D\theta\|_2^2 + k^2\|\theta\|_2^2 + 2q\delta \int_0^1 Re[w^*(z)\theta(z)]dz - 2q\int_{1-\delta}^1 Re[w^*(z)\theta(z)]dz \ge 0. \tag{4.56}$$

Just as before, we use (4.39) and (4.38) to bound this quantity as

$$\mathcal{Q}_{IH} \ge \|D\theta\|_2^2 + \left(\frac{k^4}{\mathrm{R}^2} + \frac{2q\delta}{\mathrm{R}}\right)\|\omega\|_2^2 - 2q\int_{1-\delta}^1 Re[w^*(z)\theta(z)]dz. \tag{4.57}$$

The pointwise estimates (4.33) and (4.35) then allow us to bound the boundary layer integral

$$2q\left|\int_{1-\delta}^1 w^*(z)\theta(z)dz\right| \le \frac{2^{1/2}\cdot 3^{3/4}\cdot q}{5} k^{1/2}\delta^{5/2}\|\omega\|_2\|D\theta\|_2 \tag{4.58}$$

$$\le \|D\theta\|_2^2 + \frac{3^{3/2}\cdot q^2}{2\cdot 5^2} k\delta^5\|\omega\|_2^2. \tag{4.59}$$

As before this implies that $\mathcal{Q}_{IH} \geq 0$ so long as

$$\frac{k^4}{\mathrm{R}^2} + \frac{2q\delta}{\mathrm{R}} - \frac{3^{3/2}\cdot q^2}{2\cdot 5^2} k\delta^5 \geq 0 \tag{4.60}$$

$$\Rightarrow \frac{3^{3/2}\cdot q^2}{2\cdot 5^2}\delta^5 \leq \frac{k^3}{\mathrm{R}^2} + \frac{2q\delta}{k\mathrm{R}}, \tag{4.61}$$

which upon minimizing the right hand side over k is equivalent to

$$\frac{3^{3/2}\cdot q^2}{2\cdot 5^2}\delta^5 \leq \frac{2^{11/4}\cdot q^{3/4}\cdot \delta^{3/4}}{3^{3/4}} \frac{1}{\mathrm{R}^{1/4}} \tag{4.62}$$

$$\Rightarrow \delta^{17/4} \leq \frac{2^{7/4}\cdot 5^2}{3^{9/4}\cdot q^{5/4}} \frac{1}{\mathrm{R}^{1/4}} \tag{4.63}$$

$$\Rightarrow \delta \leq \frac{2^{7/17}\cdot 5^{8/17}}{3^{9/17}\cdot q^{5/17}} \frac{1}{\mathrm{R}^{5/17}} \tag{4.64}$$

where

$$k = \left(\frac{2q\delta}{3}\mathrm{R}\right)^{1/4} \tag{4.65}$$

is the saturating wavenumber.

Returning to the bound on the averaged temperature, we arrive at

$$\langle T\rangle \lesssim \frac{2^{7/17}\cdot 5^{8/17}\cdot q^{12/17}\cdot (1-q)}{3^{9/17}} \frac{1}{\mathrm{R}^{5/17}} \tag{4.66}$$

which, upon optimizing over q leads to

$$\langle T\rangle \lesssim \frac{2^{21/17}\cdot 5^{8/17}\cdot 3^{3/17}\cdot 17^{12/17}}{29^{24/17}} \frac{1}{\mathrm{R}^{5/17}} \sim 0.3881\mathrm{R}^{-5/17} \tag{4.67}$$

where $q = \frac{12}{29}$ is optimal.

As discussed at the end of Chapter III, the key difference between the analysis performed on this problem and the boundary driven one, lies in the change in optimization for the critical, saturating wavenumber. For traditional Rayleigh-Bénard convection the saturating wavenumber was easily identifiable as scaling like $\mathrm{Ra}^{1/4}$. When the convection is driven by internal heating, the critical wavenumber behavior is implicitly defined, i.e. in reality $k \sim \mathrm{R}^{3/17}$, but this is not immediate from

minimizing the right hand side of (4.62). In further analogy to traditional Rayleigh-Bénard convection, the free-slip bound on internal heating is not as strong as that obtained for no-slip in Whitehead and Doering (2011a), but is still consistent with the numerical simulations performed in Sotin and Labrosse (1999). In Sotin and Labrosse (1999) for the strictly internal heating problem, an exponent of 0.234 was estimated. $\frac{5}{17} \sim 0.2941$ is not inconsistent with this numerically measured quantity, and lies within the same margin of error experienced with comparisons between rigorous bounds and numerical experiments for traditional convection problems (see Johnston and Doering (2009); Ahlers et al. (2009)).

4.4 Conclusions

As mentioned in the Introduction to this Chapter, convection is rarely entirely driven by a constant internal heat source, nor strictly by an imposed temperature gradient. A more realistic analysis would investigate the combination of these two driving forces akin to the numerical study performed in Sotin and Labrosse (1999), or perhaps the inclusion of reaction type interactions that are temperature dependent (see Goluskin (2011)). Further investigation of these situations, and the applicable analysis for both free-slip and no-slip velocity boundary conditions are of fundamental interest to the geophysical and astrophysical communities.

The different dynamics between free-slip and no-slip convection are well documented (see Julien et al. (1995) for one specific instance) at least at finite Pr. It is interesting to note that the analysis is significantly different as well. For infinite Pr no-slip, the bounds derived in Doering et al. (2006) and Chapter II rely on a singular integral Hardy-Rellich type inequality that is uniformly valid in the wavenumber k, but of necessity introduces logarithmic corrections to the bounds. Here, as in

Chapter III the analysis for stress-free boundaries relies on estimates that are non-uniform in k, and in fact isolates a uniquely important scale. This introduces another scale into the system that is different than the boundary layer thickness, and distinguished from any other known scales of interest. While one must be careful to not draw physical conclusions from such a mathematically based construct, the question arises whether the scale $\sim \mathrm{Ra}^{-1/4}$ (or equivalently $k \sim \mathrm{R}^{3/17}$) has any physical significance for free-slip convection, and if so, if there is a similar scale of physical importance present in no-slip convection.

Combined with Chapter III these results provide ample evidence that the 'optimal' scaling for stress-free (slippery) convection is $\mathrm{Nu} \sim \mathrm{Ra}^{5/12}$. The extension of these results to finite Pr in three spatial dimensions is nontrivial however, as the enstrophy balance (implicitly maintained for infinite Pr as described above, and explicitly included for 2d convection in Chapter III) is critical in the analysis, and without a proof of global regularity for the equations of motion (see Fefferman (2002)) there is no hope for including an enstrophy balance for 3 dimensional, finite Prandtl number, stress-free convection. Even if such a result were available, in three dimensions the vorticity is no longer a scalar quantity, and the enstrophy balance becomes far more complicated. This does not preclude the possibility that certain assumptions on the flows in three dimensions may yield bounds on the enstrophy that will lead to the same bounds found here and in Chapter III.

The results of this Chapter are reported in Whitehead and Doering (2011b).

CHAPTER V

A stability analysis of divergence damping on a latitude-longitude grid

5.1 Introduction

This Chapter focuses on the characteristics of an explicit diffusion mechanism in the finite-volume (FV) dynamical core (see Lin (2004)) that is part of the Community Atmosphere Model CAM version 5 (CAM 5) at the National Center for Atmospheric Research (NCAR) (see Neale et al. (2010)). A dynamical core is, broadly speaking, that part of an atmospheric General Circulation Model (GCM) associated with the fluid dynamics. It includes both the resolved and subgrid-scale flow. The spatial scale of the resolved flow is determined by the grid spacing of the discrete mesh. The actual "believable scales" of a model are highly dependent on the numerical scheme (see Lander and Hoskins (1997)). For example, Skamarock (2004) estimated with the help of kinetic energy spectra that the "effective resolution" of the Weather Research and Forecasting (WRF) model is $7\Delta x$ where Δx symbolizes the grid spacing. In any case, subgrid scales smaller than $2\Delta x$ fall below the resolution of the grid. Slightly larger scales (for WRF these are the scales between $2\Delta x$ and $7\Delta x$) are represented by the model, but not resolved effectively. This paper seeks to quantify the effects of diffusive processes on these un- and under-resolved subgrid scales in GCMs. Of particular interest here is the impact of a specific, explicitly added diffusive mechanism

on the underresolved scales.

The dynamical core of each model is engineered to satisfy a delicate balance between numerical stability, an accurate representation of the equations of motion, and computational cost. In an effort to balance these factors, each model employs some form of diffusion, filtering or a-posteriori fixers (see Williamson et al. (2009)). Often these practices are poorly documented, with the presumption that their impact on model performance is small. This presumption is often justified when considering their effect on a fully resolved, isolated wave. However, model performance is determined by a complex spectrum of motions on many scales and the interactions of these scales. The decay of waves, ultimately, has important implications for the mean circulation of the atmosphere (see Andrews and McIntyre (1978)). Therefore, relegating this ultimate decay to a set of poorly understood subgrid-scale processes leaves an undocumented impact on the model circulation and possibly the climate statistics in long time integrations. Scientific rigor requires the evaluation of the effects of adding diffusion, filters and fixers (see Jablonowski and Williamson (2011)). We assert that this might be a particularly important aspect of dynamical cores as we push models to higher resolution in pursuit of more realistic representations of both climate and weather. This assertion is based on the fact that it has been implicit in both model construction and dynamical meteorology that the scales of interest are quasi-nondivergent. This will not be true for models with grid sizes of order 10 km or finer that start to resolve motions in the meso-scale regime.

Spurious, dispersive phenomena are a common problem inherent to computational fluid dynamics. Examples include the Gibbs phenomenon, non-propagating numerical modes and spectral blocking (e.g. Rood (1987)). These phenomena may propagate, interact nonlinearly and negatively impact the model solution. An eco-

nomic method to reduce these dispersive modes is to add an explicit diffusion term to the equations of motion prior to discretization. Most often, a hyper-diffusion technique is used as documented in Jablonowski and Williamson (2011). This provides a mechanism to dissipate these known spurious modes, presumably, before they have a negative impact on the overall dynamics.

Generally, the strength of the diffusive process is empirically tuned so that the kinetic energy spectra imitate observation (see Boville (1991); Takahashi et al. (2006)). This technique is classically utilized in spectral transform based schemes where the Gibbs phenomenon is present when sharp gradients in the flow field arise. Explicit diffusion or filtering processes are also widely used in finite-difference or spectral element dynamical cores. In contrast, flux-limiting finite-difference and flux- or slope-limiting finite-volume methods typically introduce an inherent nonlinear diffusion via the numerical scheme that prevents unphysical oscillations from appearing (see Durran (1999)). Here, the phrase "unphysical" refers to obvious overshoots and undershoots of numerical estimates. Sometimes the modeler will deliberately choose an inherently diffusive, low-order, numerical scheme to "manage" such numerical issues, and hence avoid or alleviate the need for an additional explicit diffusive term. Considering the treatment of dispersion errors, the management of nonlinear or linear computational instabilities, the effects of grid staggering, and inherent diffusion, all models have some forms of diffusion mechanisms that are not fully grounded in the basic physics of the fluid flow. The overarching goal is to avoid the accumulation of energy or enstrophy at the smallest scales near the truncation limit.

In this Chapter we explore the linear von Neumann stability characteristics of a second-order and fourth-order horizontal divergence damping mechanism applied on a regular, equal-angle latitude-longitude grid. As a specific instance, we con-

sider the divergence damping implementation in the FV dynamical core of CAM 5 (see Lauritzen et al. (2011a)) which utilizes explicit time-stepping (see Neale et al. (2010)). The second-order divergence damping mechanism in CAM 5 is also implemented in earlier versions of CAM (CAM 4 and the finite-volume dynamical core in CAM 3.1, see Collins et al. (2004)). This FV dynamical core was developed at the NASA Goddard Space Flight Center, and has some similarities to the Goddard Earth Observing System version 5 model (GEOS5) (see Rienecker et al. (2008)) and the NOAA Geophysical Fluid Dynamics Laboratory's (GFDL) atmospheric model AM2.1 (see Delworth et al. (2006)).

The analysis carried out in the following sections is not specific to the finite-volume dynamical core and is relevant to any model that employs divergence damping on a regular latitude-longitude grid with an explicit time-stepping scheme. Our particular analysis is carried out on a staggered D-grid (see Arakawa and Lamb (1977)). However, the analysis technique generalizes to other grid staggering options and is, in fact, identical for C-grids. We explore the divergence damping mechanism from both a theoretical and practical viewpoint. The latter includes selected dynamical core test cases that demonstrate the impact of the diffusive processes directly on the model simulations. This provides a guiding method to analyze the additional diffusion incorporated in other climate or weather models. Similar tests and analysis can be performed on other forms of explicit diffusion, providing a systematic framework that brings to light the various methods for introducing diffusion to a model. Simulations for two different idealized dynamical core test cases indicate that this linear stability analysis is very accurate, providing more impetus to perform similar stability analyses on other models' methods of explicit diffusion or damping.

This Chapter is organized as follows. In section 5.2 we review the finite-volume

dynamical core as set up in CAM and discuss the implementation (and motivation) of horizontal divergence damping on a latitude-longitude grid. In sections 5.3 and 5.4 we present stability analyses of both the second-order and fourth-order divergence damping mechanisms. In addition, we analyze the impact of various formulations of the divergence damping coefficient on idealized dynamical core simulations and compare these to the theoretical analyses. Conclusions and future work are presented in section 5.5. Appendix B incorporates the effects of the polar Fourier filter into the stability analyses.

5.2 The Finite-Volume Dynamical Core in CAM

5.2.1 Design aspects

The finite-volume dynamical core in CAM 5 (CAM-FV) is constructed in a flux form which is mass-conserving by design. The hydrostatic approximation allows the horizontal discretization to be built from a 2D shallow water algorithm (see Lin and Rood (1997)). The vertical discretization of the model utilizes a floating Lagrangian coordinate that is remapped to an Eulerian reference grid after several sub-cycled dynamics time steps (see Lin (2004)). In this study, we do not directly investigate the effects of this vertical discretization, nor the remapping algorithm. The following is primarily concerned with the horizontal discretization.

The horizontal discretization is based on one-dimensional finite-volume schemes. The prognostic variables are cast on a staggered D-grid that "favors" the conservation of vorticity. In order to compute the mass and momentum fluxes across cell boundaries, a dual C-grid formulation (a "CD" grid) is utilized. First, the variables on the C-grid are advanced by half a time step to estimate the time-centered "advective" C-grid winds. These are then used to advance the prognostic variables on the

D-grid which assures a second-order accuracy in time. As an aside, the CD-grid approach introduces some inherent numerical diffusion due to grid interpolations. This is discussed in Skamarock (2008) who reviewed the linear stability characteristics of the CAM-FV dynamical core.

Finite-volume methods are developed with the general supposition that diffusive behavior near steep gradients is preferable to dispersive waves which generate unphysical extrema in the solution (see Bala et al. (2008) for a specific example). CAM 5 primarily uses the formally third-order Piecewise Parabolic Method (PPM, Colella and Woodward (1984)) for the integration of the prognostic variables on the D-grid. In addition, a second-order van Leer method is applied for the computation of the C-grid winds (see Lin and Rood (1997)). Both algorithms also incorporate a first-order upwind scheme to represent advective inner operators in the cross directions. This approach is designed to eliminate the directional bias or splitting error. However, as pointed out in Lauritzen (2007) this limits the overall accuracy of the entire scheme, introducing nonlinear diffusive effects and possible instabilities. In CAM-FV there are also several choices for the finite-volume slope- and curvature-limiters which are applied near steep gradients (see Lin and Rood (1996); Lin (2004)). In addition, enhanced inherent diffusion is included near the model top to provide a sponge layer. This is accomplished by lowering the order of the flux operators to a first-order upwind or second-order van Leer scheme and increasing the effects of the divergence damping mechanism in the uppermost few levels (typically 3 levels for a 26-level configuration).

5.2.2 The need for polar filtering

The Lin-Rood algorithm (see Lin and Rood (1997)) is developed on a latitude-longitude rectangular grid, with constant (in angle) mesh spacing. This leads to a

convergence of the longitudinal (zonal) grid points near each geographic pole. To lessen the corresponding strict time step restriction near the poles, a semi-Lagrangian extension of the transport scheme is implemented in the longitudinal direction (see Lin and Rood (1996)). However, the semi-Lagrangian method does not filter small-scale noise inherent to this grid and numerical method. Therefore, a polar Fourier filter is applied poleward of the midlatitudes starting at approximately $36 - 40^\circ$ N/S. The Fourier filter coefficients gradually increase in strength as the poles are approached and follow the formulation in Fox-Rabinovitz et al. (1997) (see also Eq. (B.1)). The Fourier filter removes linear and nonlinear computational instabilities, but only selectively damps the waves in the zonal direction. No filtering is applied in the meridional direction. It will be shown that the Fourier filter interacts very closely with the horizontal divergence damping discussed in this paper, and both should be considered with some care.

5.2.3 Inherent diffusion in CAM-FV

The Lin-Rood algorithm is built to conserve and transport vorticity monotonically. This is done by considering the vector invariant form of the horizontal equations of motion (see Lin (2004)). Limiters are applied to the vorticity fluxes in a highly nonlinear fashion to ensure that unphysical extrema are not generated. These limiters introduce a certain level of inherent diffusion to the vorticity. This provides, conjecturally, a nonlinear imitation of the kinematic viscosity of a viscous fluid, but does not model the bulk viscosity that appears in divergent flows. As the order of the scheme is increased, this kinematic diffusive process will increase in order which can be concluded from a short calculation of the modified equation for a linear highly simplified flow (not shown here). As an example, the formally third-order PPM scheme corresponds to a fourth-order damping of the vorticity, while the first-order

upwind scheme corresponds to a second-order diffusive term. The inherent diffusion in this algorithm is only applied to the vorticity. Divergence damping can therefore be thought of as a "fix" to imitate an equivalent diffusive force on the divergence. Explicitly added horizontal diffusion of the momentum would have the same effect, but would unnecessarily damp the vorticity as well.

The previous discussion may lend an intuitive and qualitative reasoning for the need of divergence damping in CAM-FV, but it does not provide a quantitative method for estimating the needed damping coefficient. Instead, this coefficient intuitively depends on grid size, time step and latitude; that is, physical attributes of the scales of motion. In general, diffusion coefficients are often chosen empirically to match the model with observations and believed "truth". One measure of "truth" is the behavior of the kinetic energy spectrum at large wavenumbers (see Nastrom and Gage (1985); Lindborg (1999); Jablonowski and Williamson (2011)). This is an indirect measure and should not be used as the sole criterion. As shown in the next section, the choice of the damping coefficient has a significant impact on the dynamics, as a large enough value will introduce instabilities at a fundamental level due to the explicit time-stepping in CAM-FV. Too little damping on the other hand will allow small-scale oscillations to propagate or even fail to prevent instabilities (both linear and nonlinear) from developing.

5.2.4 The formulation of horizontal divergence damping

Horizontal divergence damping was suggested by Sadourny (1975), Dey (1978), Haltiner and Williams (1980) and Bates et al. (1993) to control numerical noise in weather forecast models and for numerical stability reasons. The particular form of

the second-order horizontal divergence damping mechanism is

$$\frac{\partial u}{\partial t} = \cdots + \frac{1}{a\cos\phi}\frac{\partial}{\partial\lambda}\big(\nu_2 D\big) \tag{5.1}$$

$$\frac{\partial v}{\partial t} = \cdots + \frac{1}{a}\frac{\partial}{\partial\phi}\big(\nu_2 D\big), \tag{5.2}$$

where u and v are the zonal and meridional components of velocity, a is the radius of the earth, $\phi \in [-\pi/2, \pi/2]$ and $\lambda \in [0, 2\pi]$ stand for the latitude and longitude, t is time, and ν_2 symbolizes the second-order divergence damping coefficient. The horizontal divergence D is given by

$$D = \frac{1}{a\cos\phi}\left(\frac{\partial u}{\partial\lambda} + \frac{\partial(v\cos\phi)}{\partial\phi}\right). \tag{5.3}$$

If we apply the divergence operator to Eqs. (5.1) and (5.2) we arrive at the evolution equation for the divergence

$$\frac{\partial D}{\partial t} = \cdots + \nabla^2\left(\nu_2 D\right). \tag{5.4}$$

This Laplacian type (∇^2) diffusion of the divergence damps all scales, but with more damping at higher wave numbers (akin to the square of the wave number). A standard practice in atmospheric modeling is to invoke a fourth-order hyper-diffusion that is meant to be more scale-selective (fourth power of the wave number, Collins et al. (2004)). This practice is based on the premise that lower-order damping may overly damp the larger scales that are physically relevant, and the presumption that it is the smallest scales that need to be eliminated. Because of this practice, we also explore higher-order damping mechanisms. In particular, the fourth-order divergence damping is given by

$$\frac{\partial u}{\partial t} = \cdots - \frac{1}{a\cos\phi}\frac{\partial}{\partial\lambda}\big(\nu_4\nabla^2 D\big) \tag{5.5}$$

$$\frac{\partial v}{\partial t} = \cdots - \frac{1}{a}\frac{\partial}{\partial\phi}\big(\nu_4\nabla^2 D\big), \tag{5.6}$$

where ν_4 is the damping coefficient for the fourth-order divergence damping. This leads to the following evolution equation for the horizontal divergence (if we assume that ν_4 has no dependence on ϕ or λ)

$$\frac{\partial D}{\partial t} = \cdots - \nu_4 \nabla^4 D. \tag{5.7}$$

In the following we perform a linear stability analysis on (5.4) and (5.7).

Eq. (5.4) is easily recognized as the heat (diffusion) equation, and (5.7) can be seen as the hyper-diffusion equation. Therefore, analyzing the stability of the divergence damping reduces to determining the stability of the diffusion or hyper-diffusion equation on the sphere. The corresponding details of the discretization will likely change somewhat between different model implementations, and this will affect the stability of the scheme; however, the basic analysis should carry over to each individual model. In the following sections we analyze the stability of (5.4) and (5.7) using the finite-difference discretization with an explicit time-stepping scheme as implemented in CAM 5. The default CAM 5 configuration employs the second-order divergence damping. The fourth-order damping can be selected as an option at run time. Because we analyze the scalar equations (5.4) and (5.7) the nature of the analysis is universal to both the C- and D- grid staggerings, as long as a latitude-longitude geometry is maintained.

5.3 Second-Order Divergence Damping

5.3.1 Stability analysis

For all that follows, subscripts indicate locations on the discretized grid, with the first letter i indicating the east-west (longitudinal or zonal) direction, and the second index j denoting the north-south direction (latitudinal or meridional). $\Delta\lambda$ and $\Delta\phi$ are the constant longitudinal and latitudinal grid spacings, respectively. The

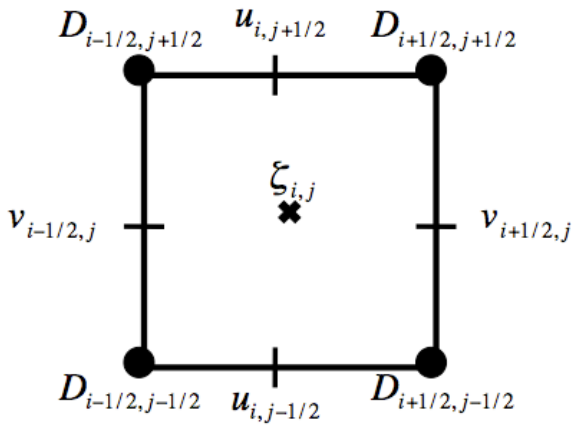

Figure 5.1: Discretization of the prognostic winds (u, v) and corresponding divergence D as well as the vorticity ζ.

divergence damping is applied to the prognostic horizontal wind components that are discretized on the D-grid as discussed above. This is shown in Fig. 5.1. In this figure the cell is centered at $(i\Delta\lambda, j\Delta\phi)$ and the winds are staggered appropriately around the cell so that the discretized vorticity $\zeta_{i,j}$ lies at the cell center. This places the divergence at the cell corners as illustrated in Fig. 5.1.

The divergence of the flow field with

$$\begin{aligned} u_{i,j-1/2} &= u\left(i\Delta\lambda, (j-1/2)\Delta\phi\right) \\ v_{i-1/2,j} &= v\left((i-1/2)\Delta\lambda, j\Delta\phi\right), \end{aligned}$$

is given by

(5.8)

$$D_{i-1/2,j-1/2} = \frac{1}{a\cos\phi_{j-1/2}}\left[\frac{u_{i,j-1/2} - u_{i-1,j-1/2}}{\Delta\lambda} + \frac{v_{i-1/2,j}\cos\phi_j - v_{i-1/2,j-1}\cos\phi_{j-1}}{\Delta\phi}\right].$$

We then write the discretized versions of Eqs. (5.1) and (5.2) as follows (the superscript 'n' refers to the time index, i.e. $\chi^n_{i,j} = \chi(i\Delta\lambda, j\Delta\phi, n\Delta t)$):

$$\begin{aligned} \frac{u^{n+1}_{i,j-1/2} - u^n_{i,j-1/2}}{\Delta t} &= \frac{\nu_2}{a\Delta\lambda\cos\phi_{j-1/2}}\left[D^n_{i+1/2,j-1/2} - D^n_{i-1/2,j-1/2}\right] \\ \frac{v^{n+1}_{i-1/2,j} - v^n_{i-1/2,j}}{\Delta t} &= \frac{\nu_2}{a\Delta\phi}\left[D^n_{i-1/2,j+1/2} - D^n_{i-1/2,j-1/2}\right]. \end{aligned}$$

Note that we have assumed that the coefficient ν_2 is independent of ϕ and λ (in reality we only need to assume that $\cos\phi$ does not vary on the grid level, as discussed below). In practice, ν_2 is chosen to be dependent on the time-step Δt and grid spacing (possibly latitudinally dependent). Suppression of this dependence at this point simplifies the algebra. Ideally we want to analyze the stability of this system, however this becomes prohibitive, as the eigenvalues inherent to the problem are not conducive to calculation. Instead we consider the evolution of the divergence (Eq. (5.4)) in CAM-FV which is discretized with the finite-difference approach

$$\begin{aligned}
&\frac{D^{n+1}_{i-1/2,j-1/2} - D^{n}_{i-1/2,j-1/2}}{\Delta t} = \frac{\nu_2}{a^2 \cos\phi_{j-1/2}} \\
\times \quad &\left\{ \frac{\cos\phi_j \left(D^{n}_{i-1/2,j+1/2} - D^{n}_{i-1/2,j-1/2} \right) - \cos\phi_{j-1} \left(D^{n}_{i-1/2,j-1/2} - D^{n}_{i-1/2,j-3/2} \right)}{(\Delta\phi)^2} \right. \\
+ \quad &\left. \frac{D^{n}_{i+1/2,j-1/2} - 2D^{n}_{i-1/2,j-1/2} + D^{n}_{i-3/2,j-1/2}}{(\Delta\lambda)^2 \cos\phi_{j-1/2}} \right\}.
\end{aligned}$$

The same analysis holds on the C-grid if each of the indices above are shifted by 1/2, not affecting the results obtained below.

In practice the divergence damping coefficient is defined as

$$\nu_2 = C_2 \ \cos^r \phi \ \frac{a^2 \Delta\phi \Delta\lambda}{\Delta t}, \tag{5.9}$$

where $r = 0$ is the default in CAM 5.0. The parameter r can be chosen to modify the latitudinal dependence of the damping coefficient. The empirical "tuning" parameter C_2 depends on the position in the vertical direction to provide increased damping near the model top. More information on C_2 is provided below. This formulation of ν_2 with $r = 0$ is proportional to the area of a grid cell at the equator, and inversely proportional to the time step. Dimensionally this is an appropriate choice of damping coefficient, however reliance on the area of the grid cell at the equator,

and not the true area of the grid cell (with appropriate latitudinal dependence) places the same damping effect on a given physical wave-length, regardless of discretization or latitudinal location.

Using (5.9) we now assume that $\cos\phi$ is approximately constant at the grid level ($\cos\phi_{j+1} \sim \cos\phi_j \sim \cos\phi$, which is the same approximation alluded to in deriving the evolution of the divergence). We consider a standard von Neumann stability analysis of Eq. (5.9), following Lauritzen (2007). In Lauritzen (2007) the discretization was formulated as a cell average approach. This is identical to the above, if we simply replace each $D_{i-1/2,j-1/2}$ with the corresponding cell average at each grid cell. Hence, we consider the growth of each wave number k (or combination of longitudinal and latitudinal wave numbers k_λ and k_ϕ in this case) by looking at solutions of the type

$$\begin{aligned} D(\lambda,\phi,t) &= D_0 e^{\imath\left(\omega t + k_\lambda \lambda + k_\phi \phi\right)} \\ \Rightarrow D^n_{i,j} &= D_0 \Gamma_2^n e^{\imath(i k_\lambda \Delta\lambda + j k_\phi \Delta\phi)}, \end{aligned} \tag{5.10}$$

where D_0 denotes the initial amplitude of the wave, ω stands for the frequency, $\Gamma_2 = e^{\imath\omega\Delta t}$ is the complex amplification factor, and $\imath = \sqrt{-1}$ represents the imaginary unit number. The scheme described previously is stable if the growth in each wave number, given by $|\Gamma_2|$, is less than or equal to unity (although a more realistic restriction is to force Γ_2 to remain positive as well). Inserting the ansatz (5.10) in the discretized divergence equation (5.9), and dividing by the common factor $D_0\Gamma_2^n e^{\imath\left[(i-1/2)k_\lambda\Delta\lambda + (j-1/2)k_\phi\Delta\phi\right]}$ we identify the amplification factor as

$$\Gamma_2 = 1 - 4\,C_2\,\cos^r\phi\left\{\alpha\sin^2\left(\frac{k_\phi\Delta\phi}{2}\right) + \frac{1}{\alpha\cos^2\phi}\sin^2\left(\frac{k_\lambda\Delta\lambda}{2}\right)\right\}, \tag{5.11}$$

where $\alpha = \Delta\lambda/\Delta\phi$ is the grid aspect ratio. Note that Eq. (5.11) is real because this discretization is symmetric. In our model simulations, α will be identical to 1. In

default CAM 5 configurations an aspect ratio of $\alpha \sim 1.33$ is also often chosen with wider longitudinal grid spacings.

As mentioned, the minimum requirement for stability in a linear flow is to restrict C_2 such that $|\Gamma_2| \leq 1$, although it would be preferable to restrict $0 \leq \Gamma_2 \leq 1$ ensuring that the modes do not change sign with each time step. At the equator with $\phi = 0°$, these requirements are equivalent to

$$C_2 \left\{ \alpha + \frac{1}{\alpha} \right\} \leq \frac{1}{4} \qquad \text{and} \qquad C_2 \left\{ \alpha + \frac{1}{\alpha} \right\} \leq \frac{1}{8},$$

where the stricter requirement does not allow the sign of the wave to change with each time step. However, near the poles Eq. (5.11) becomes increasingly more restrictive, indicating that instabilities in the divergence field will emerge in the polar regions (particularly for $r = 0$). Note that this singularity appears in the zonal direction as the poles are approached ($|\phi| \to \pi/2$) and originates from the second term in the curly brackets in Eq. (5.11). The polar Fourier filter is designed to remove zonal instabilities near the poles, and so in practice this instability is not revealed in CAM-FV. To see how the polar Fourier filter removes this instability, the reader is referred to the Appendix.

While the singularity at the poles found in (5.11) for $r = 0$ is controlled by the polar filter, it is of interest to consider $r = 1$ as well, which takes the latitudinal dependence of the grid cell's approximate area into account. In this instance, the singularity in the zonal direction is reduced near the poles, but now there is an additional $\cos\phi$ on the meridional modes (first term in the curly bracket in (5.11)) which reduces the effective damping of such modes near the poles. In essence, this indicates a delicate balance between the zonal and meridional waves; using $r = 0$ damps the wave numbers in the meridional direction sufficiently, but is only marginally stable

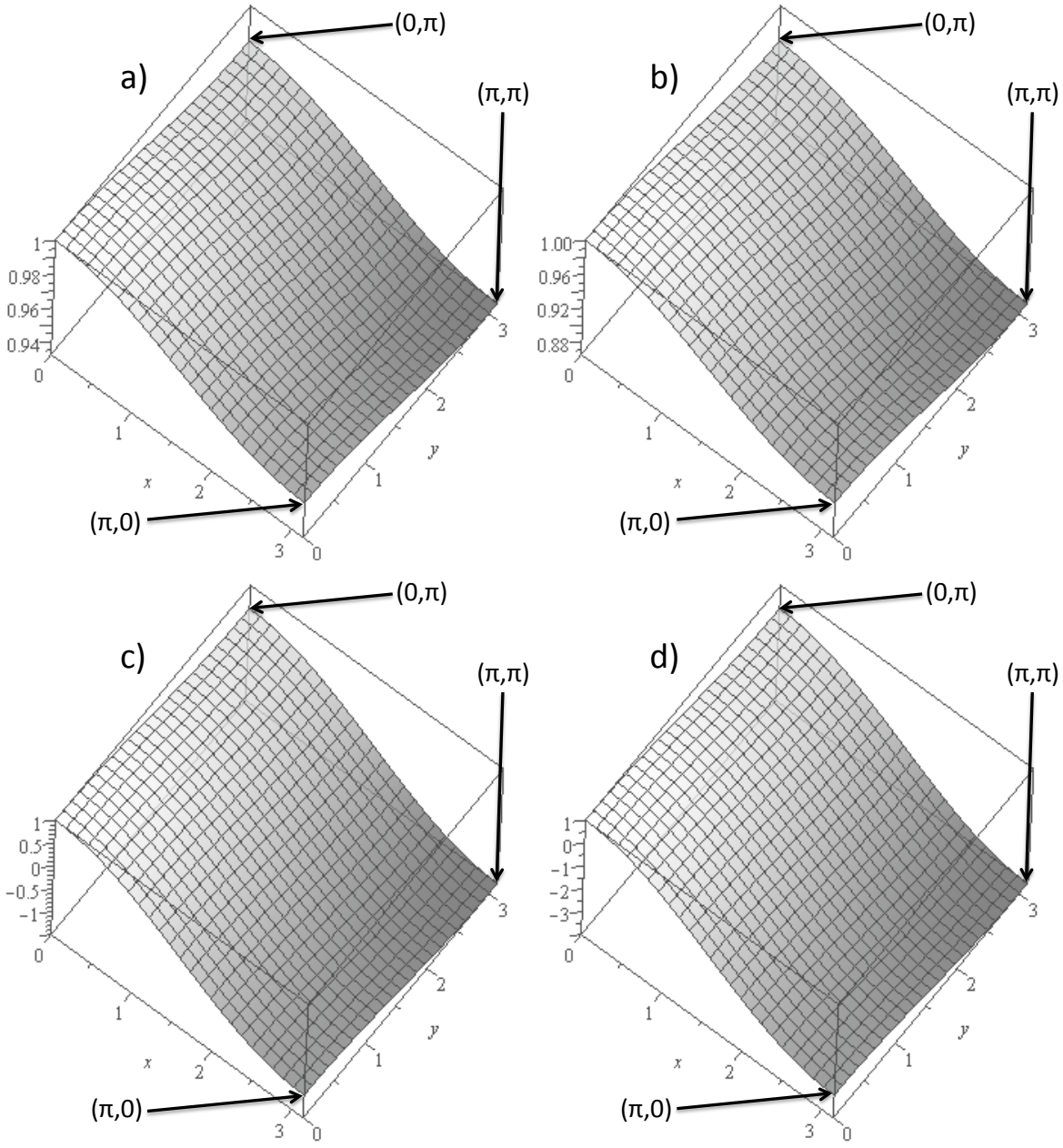

Figure 5.2: Amplification factor for the second-order damping (a,c) Γ_2 for $r = 1$ and (b,d) Γ_2 with $r = 0$. The top row (a,b) shows the CAM 5 default configurations with $C_2 = 1/128$ and $\alpha = 1.33$, the bottom row (c,d) shows the extreme case with $C_2 = 1/4$ and $\alpha = 1$. All four plots are created at a latitude of $\phi = \pi/3 = 60°$. The axis labels are $x = k_\lambda \Delta\lambda$ and $y = k_\phi \Delta\phi$. Thus $x = \pi$ corresponds to the smallest resolvable wavelength of $2\Delta\lambda$. Note the differences in scale.

(with the application of the Fourier filter) for the zonal wave numbers, while using $r = 1$ reduces this instability in the zonal direction, but does not damp the meridional waves as efficiently. To visualize these effects, Fig. 5.2 provides a plot of the amplification factor Γ_2 (without Fourier filter) for both $r = 0$ (CAM default) and $r = 1$ at a latitude of $\phi = 60°$. The top row is shown for the typical CAM 5 values of $C_2 = 1/128$ and $\alpha = 1.33$, the bottom row displays the extreme case (critical at the equator at least) $C_2 = 1/4$ with $\alpha = 1$. These constant C_2 values neglect the sponge layer at the model top that is discussed later. Note that the axis labels are described by $x = k_\lambda \Delta\lambda$ and $y = k_\phi \Delta\phi$ where the value of x=y=π denotes the smallest wavelength $2\Delta\lambda$ or $2\Delta\phi$.

At this latitude of $\phi = 60°$ the typical CAM 5 configurations (Figs. 5.2(a,b), (b) is the default) are stable since the amplification factors are bounded by $|\Gamma_2| \leq 1$. However, there is a latitude close to the poles for which both $r = [0, 1]$ become unstable. In particular, the instability occurs when the $(2\Delta\lambda, 2\Delta\phi) = (\pi, \pi)$ wave drops below -1. For $r = 1$ this does not occur until $|\phi| > 89°$ (not shown). For $r = 0$ the amplification drops below -1 for $|\phi| > 83°$. Both instabilities are adequately controlled by the polar Fourier filter, as illustrated in the Appendix.

The key observation to take away from Fig. 5.2 is that at these higher latitudes the waves in the zonal direction become unstable, while for $r = 1$, the purely meridional wave numbers become less damped with increasing wavenumber (decreasing scale). This can partially be seen from Fig. 5.2c where we observe that the $2\Delta\phi$ wave $(0, \pi)$ has an amplification factor of $\Gamma_2 \sim 0.8$ for $r = 1$, whereas the corresponding amplification factor for $r = 0$ is $\Gamma_2 \sim 0.4$ (Fig. 5.2d). This implies that at high latitudes (here $\phi = 60°$), using $r = 1$ will not quickly damp out small-scale purely meridional waves. However, as noted in the previous paragraph, the choice of $r = 0$

implies that the polar filter is required to maintain the computational stability at a lower latitude than would be needed for $r = 1$.

5.3.2 Vertical Profile of the second-order damping coeffcient

As mentioned previously, the parameter C_2 is designed to depend on the vertical position in the FV dynamical core. This dependence introduces a diffusive sponge layer near the model top to absorb rather than reflect outgoing gravity waves. This concept of a diffusive sponge layer is outlined in Jablonowski and Williamson (2011). The use of sponge layers has come under questioning (see Shepherd et al. (1996)) as it also introduces an artificial sink for momentum, and some nonlinear transfer of energy takes place due to the total energy fixer employed by all default versions of CAM (see Neale et al. (2010)). The purpose of this discussion is to determine the characteristics that arise when utilizing an artificially determined sponge layer for the divergence damping, as employed in CAM 5 and its predecessor versions CAM 4 and CAM-FV 3.1.

In the following we rely on the discussion in the previous section, with all the same definitions. Let p_{top} be the pressure at the model top (in most default CAM runs this is taken to be $p_{top} \sim 3$ hPa) and let p^l_{ref} be the reference pressure at a given model level with index l. The computation of p^l_{ref} is based on the definition of the hybrid η-coordinate (see also Neale et al. (2010)) and assumes a surface pressure of 1000 hPa. Then, as implemented in the FV dycore, the parameter C_2^l depends on the model level and is given by

$$C_2^l = c \max\left\{1, 8\left[1 + \tanh\left(\ln\left(\frac{p_{top}}{p^l_{ref}}\right)\right)\right]\right\}. \tag{5.12}$$

The default value for c is $1/128$ which (modulo the $\cos\phi$) is certainly within the stable range at most latitudes determined in the previous section. For typical model

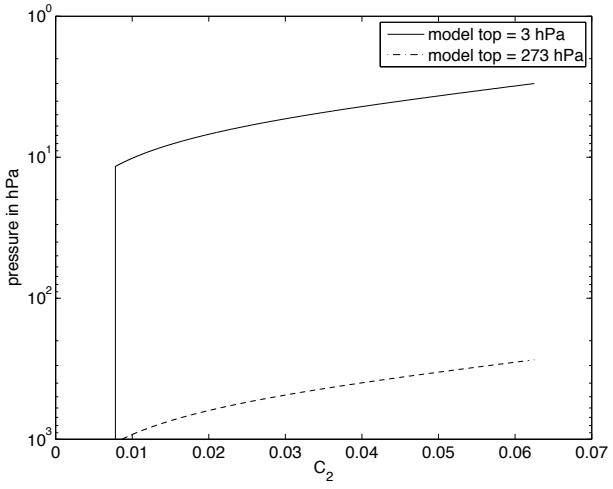

Figure 5.3: Vertical profiles of the pressure-dependent multiplicative factor in the unitless parameter C_2 (Eq. 5.12) for a configuration with the model top at $p_{top} = 3$ hPa and $p_{top} = 273$ hPa.

runs this provides a rather flat vertical profile until the final two to three model levels, whereupon the damping coefficient is increased rapidly by up to a factor of 8. It means that the strength and frequency of the polar instabilities increase near the model top due to this increased damping coefficient, requiring a stronger diffusive fixer to remove them, perhaps in addition to the polar Fourier filter. Such a fixer is, possibly serendipitously, already in place in the form of lowering the order of the numerical scheme near the model top. The latter aspect is a specific attribute of CAM-FV, i.e., this result is implementation-dependent.

Investigating the functional dependence of (5.12) on the location of the model top also raises another issue. Most model runs will be performed with the model top prescribed near $2 - 3$ hPa, however test cases specifically designed to test the dynamical core (see Jablonowski et al. (2008a)) lower the model top so as to highlight different aspects of the model's numerics. One such instance is a gravity wave test case without the Earth's rotation and an initial state at rest in which the squared Brunt-Vaisala frequency of the hydrostatic background conditions is prescribed as

$N^2 = 10^{-4}$ s^{-2}. An overlaid potential temperature perturbation then triggers the propagation of gravity waves. The surface temperature and pressure are set to 300 K and 1000 hPa, respectively. With a constant (in height) vertical grid spacing of $\Delta z = 500$ m and 20 vertical levels (L20), this forces the pressure at the model top to be $p_{top} = 273$ hPa. The dependence of the multiplicative factor C_2 on the position of such a rather high (low-lying) p_{top} value is illustrated in Fig. 5.3. The figure depicts the vertical profile of C_2 (Eq. (5.12)) for a model top at 3 hPa (solid line) and 273 hPa (dashed line). When the model top is lowered to 273 hPa the damping strengthens throughout the entire model, but particularly at the upper levels. This leads to not just a sponge layer, but an entire spongy model, detrimentally affecting the outcome of the gravity wave test case.

This observation explains a result by Jablonowski et al. (2008b) that compared the CAM-FV simulations to several other dynamical cores at their default configurations. It was noted that the default CAM-FV dynamical core with second-order divergence damping appeared to be extremely diffusive for this test case. Figure 5.4 displays this result. It depicts the potential temperature perturbation ($\Theta' = \Theta - \overline{\Theta}$) along the equator from the zonally symmetric initial state $\overline{\Theta}$, after the wave has developed for 96 hours. Note that there is a significant difference in the Θ' amplitudes and gradients between the $1^\circ \times 1^\circ$ L20 CAM-FV simulation with default divergence damping (Fig. 5.4a) and no divergence damping (Fig. 5.4c). For comparison, Figs. 5.4b,d display the corresponding results of an alternative CAM dynamical core which is the spectral transform Eulerian (CAM-EUL) model (see Collins et al. (2004)). It is run at a comparable resolution with the triangular truncation T85 and the identical 20 levels. In Fig. 5.4b the CAM-EUL default fourth-order hyper-diffusion with the coefficient $K_4 = 1 \times 10^{15}$ m^4 s^{-1} is used, in addition to a second-order diffusive sponge layer at

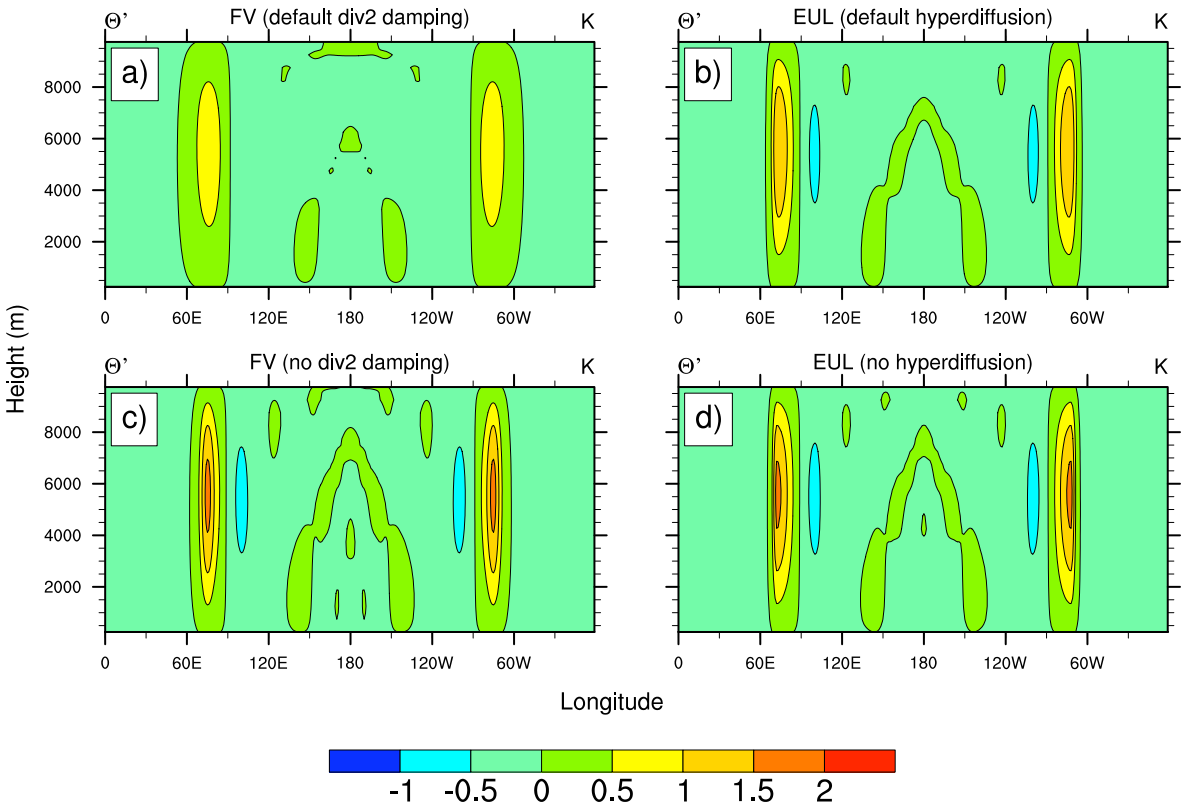

Figure 5.4: Latitude-height cross section of the potential temperature perturbation (in K) at the equator in the gravity wave test case after 96 hours. (a) CAM-FV with default second-order divergence damping (vertical dependence follows the dotted line in Fig. 5.3), (b) CAM-EUL (spectral transform Eulerian dynamical core) including a default fourth-order hyper-diffusion term and second-order sponge layer diffusion, (c) CAM-FV without divergence damping, (d) CAM-EUL without diffusion. The resolutions are (a,c) $1^\circ \times 1^\circ$ and (b,d) T85 with 20 levels and a model top at 273 hPa.

the top with the base coefficient $K_2 = 2.5 \times 10^5$ m^2 s^{-1}. In (d) both the CAM-EUL K_2 and K_4 coefficients were set to zero.

Figure 5.4 showcases several effects. First, the divergence damping in Fig. 5.4a significantly suppresses the evolution of the gravity wave along the equator and also seems to introduce a positive potential temperature perturbation in CAM-FV at the model top (near 180°). Secondly, the shape of the gravity waves in CAM-FV appear to be influenced by both the explicit diffusion via divergence damping (Fig. 5.4a) as well as the intrinsic diffusion via the numerical scheme (Fig. 5.4c). The latter can be concluded when CAM-FV is compared to CAM-EUL. The EUL simulations are characterized by sharper Θ' gradients at the leading edge of the gravity wave, even when hyper-diffusion is applied in the simulation (Fig. 5.4b). However, the perturbation amplitudes in the simulations without explicitly added damping (Figs. 5.4(c,d)) are comparable in both models. As an aside, omitting the explicit damping in CAM-FV and CAM-EUL is only feasible in idealized test cases such as the gravity wave test described here. It truly isolates the effects of the damping. In practical applications though, the damping is needed to avoid an accumulation of energy at the smallest scales and prevent CAM-EUL from becoming unstable.

5.4 Fourth-Order Divergence Damping

5.4.1 Stability analysis

Higher-order forms of divergence damping act more strongly on the higher wave numbers, while limiting the effects on the large-scale well-resolved features of the flow. We now analyze the stability constraints for fourth-order divergence damping using the notation introduced in section 5.3.

As before, we analyze the scalar equation (5.7) which we discretize with the help

of (5.8) and the following expression for the Laplacian of the divergence (also refer to Fig. 5.1)

$$\begin{aligned}
&\left(\nabla^2 D\right)_{i-1/2,j-1/2} \\
&= \frac{D_{i+1/2,j-1/2} - 2D_{i-1/2,j-1/2} + D_{i-3/2,j-1/2}}{a^2 \left(\Delta\lambda\right)^2 \cos^2\phi_{j-1/2}} \\
&\frac{\left(D_{i-1/2,j+1/2} - D_{i-1/2,j-1/2}\right)\cos\phi_j - \left(D_{i-1/2,j-1/2} - D_{i-1/2,j-3/2}\right)\cos\phi_{j-1}}{a^2 \left(\Delta\phi\right)^2 \cos\phi_{j-1/2}}.
\end{aligned} \tag{5.13}$$

It yields the discretized version of (5.7)

$$\begin{aligned}
\frac{D^{n+1}_{i-1/2,j-1/2} - D^n_{i-1/2,j-1/2}}{\Delta t} &= -\frac{\nu_4}{a^2\cos\phi_{j-1/2}} \left\{ \frac{\cos\phi_j}{\left(\Delta\phi\right)^2} \left[\left(\nabla^2 D^n\right)_{i-1/2,j+1/2} \right.\right. \\
&\left. - \left(\nabla^2 D^n\right)_{i-1/2,j-1/2} \right] - \frac{\cos\phi_{j-1}}{\left(\Delta\phi\right)^2} \left[\left(\nabla^2 D^n\right)_{i-1/2,j-1/2} - \left(\nabla^2 D^n\right)_{i-1/2,j-3/2} \right] \\
&+ \left. \frac{\left(\nabla^2 D^n\right)_{i+1/2,j-1/2} - 2\left(\nabla^2 D^n\right)_{i-1/2,j-1/2} + \left(\nabla^2 D^n\right)_{i-3/2,j-1/2}}{\left(\Delta\lambda\right)^2 \cos\phi_{j-1/2}} \right\}.
\end{aligned} \tag{5.14}$$

Here we again assume that ν_4 does not depend on ϕ or λ. While this is not entirely accurate in CAM-FV, it is permissible because we also make the assumption that $\cos\phi$ does not change on the grid level.

To analyze the stability of Eq. (5.14), we consider solutions of the form (5.10). The fourth-order damping coefficient ν_4 in CAM 5 is defined as

$$\nu_4 = C_4 \, \frac{a^4 \left(\Delta\lambda\right)^2 \left(\Delta\phi\right)^2 \cos^r\phi}{\Delta t}, \tag{5.15}$$

where $r = 2$ (the CAM 5 default if the optional fourth-order damping is invoked) lets ν_4 vary as the square of the area of each grid cell (dependent on latitude or $\cos\phi$ which again is assumed constant at the grid level). In CAM 5, the parameter C_4 is set to a default value of 0.01. Note that ν_4 does have a latitudinal dependence, but for the local analysis considered here with an approximately constant $\cos\phi$ at the grid level we can use (5.7). Once again we desire the modulus of the amplification

factor $|\Gamma_4| = |e^{i\omega\Delta t}|$ to have magnitude less than or equal to unity. Γ_4 is found to be

$$\Gamma_4 \;=\; 1 - 16\, C_4\, \cos^r \phi \left\{ \alpha \sin^2 \left(\frac{k_\phi \Delta\phi}{2} \right) + \frac{1}{\alpha \cos^2 \phi} \sin^2 \left(\frac{k_\lambda \Delta\lambda}{2} \right) \right\}^2 , \tag{5.16}$$

where $\alpha = \Delta\lambda/\Delta\phi$ as before. The effect of the polar Fourier filter on the amplification factor, and the corresponding stability constraint are described in the Appendix.

At the equator with $\phi = 0^\circ$ the stability constraint $|\Gamma_4| \leq 1$ implies that C_4 needs to be less or equal 1/32. However, the more conservative (and more desirable) constraint $0 \leq \Gamma_4 \leq 1$ demands the more restrictive bound $C_4 \leq 1/64$. Both values are quoted for $\alpha = 1$ and $r = 2$. The first estimate of the maximal value of C_4 is experimentally confirmed by considering baroclinic wave tests with CAM 5. This baroclinic wave test for dynamical cores is described in Jablonowski and Williamson (2006a,b). In essence, a perturbation in the zonal wind is added to a steady-state flow field that is initially in gradient-wind and hydrostatic balance. This perturbation develops into a baroclinic wave in the northern hemisphere. The wave breaks after nine days and creates sharp temperature fronts. However prior to day 5, the flow is primarily linear, and hence amenable for comparisons to the linear analysis performed here.

Leaving all other parameters fixed, the parameter C_4 was adjusted near the maximal value of 1/32 for the baroclinic wave. It was found that the evolution of the baroclinic wave with $C_4 < 0.031$ remained stable, whereas the model quickly developed numerical instabilities when C_4 exceeded this critical value. The simulation blew up after a few model hours. Figure 5.5 shows this development for $C_4 = 0.031$ after 4 hours and 45 minutes in the baroclinic wave test case at the resolution $1^\circ \times 1^\circ$ with 26 levels. Here, the vertical pressure velocity at the model level near 867 hPa is depicted. A similar situation developed for the gravity wave test (not shown). The

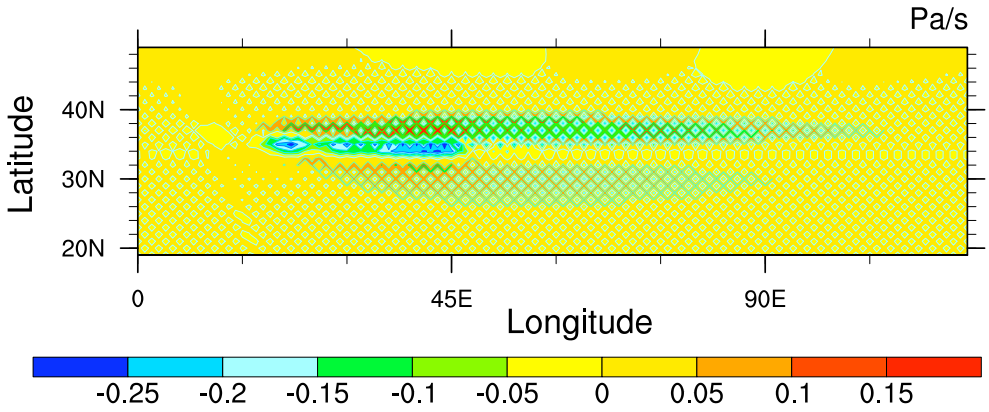

Figure 5.5: Vertical pressure velocity (in Pa/s) after 4 hours and 45 minutes at the CAM-FV model level near 867 hPa in the baroclinic wave test case. This shows the development of the $(2\Delta\lambda, 2\Delta\phi)$ instability of the fourth-order divergence damping when $C_4 = 0.031$. The resolution is $1^\circ \times 1^\circ$ with 26 vertical levels.

instability develops in the $(2\Delta\lambda, 2\Delta\phi) = (\pi, \pi)$ wave.

Note that the instability in Fig. 5.5 develops near $\phi \sim 36^\circ N$ which is precisely the position where the polar Fourier filter begins to take effect (with $\alpha = 1$). This also explains the slight discrepancy between the predicted value of $1/32 = 0.03125$ and 0.031 as observed in the model runs. If the previously omitted grid-level latitudinal dependence of Γ_4 is taken into account, an instability is expected to develop at almost exactly $C_4 = 0.031$ for $\phi = 36^\circ$. Poleward of this latitude the polar Fourier filter removes the zonal portion of this instability, and evidently controls its development. Eventually however, the developing instability at 36° overcomes the polar filter, and cascades throughout the model.

The relaxed bound $C_4 \leq 1/32$ allows the solution to change sign at each time step.Therefore, we expect that this constraint would not be sufficient for a more realistic, nonlinear flow. Instead, the more conservative restriction $C_4 < 1/64 = 0.015625$ (for $\alpha = 1$) is recommended, which is quite close to the CAM 5 default value of $C_4 = 0.01$. For the default CAM-FV settings where $\alpha = 1.33$, the recommended

restriction at the equator is $C_4 < 9/625 = 0.0144$ according to Eq. (5.16).

5.4.2 Latitudinal dependence and meridional waves

Figure 5.6 illustrates how Γ_4 (without applying the Fourier filter) with $r = 2$ depends on latitude and shows the amplification factors at both the Fig. 5.6(a,c) equator and Fig. 5.6 (b,d) $|\phi| = 60°$. Both the Fig. 5.6(a,b) CAM 5 default configuration as well as the Fig. 5.6(c,d) extremal cases are depicted. At higher latitudes Fig. 5.6(b,d), Γ_4 is smaller for the smallest zonal wave numbers ($x = \pi$). $\Gamma_4 < -1$ indicates the appearance of the grid-induced instability. For the extremal case ($\alpha = 1, C_4 = 1/32$), this happens for any latitude away from the equator. In contrast, for the default CAM-FV settings of $C_4 = 0.01$ and $\alpha = 1.33$ this occurs for $|\phi| > 76°$. This lies in the region where the Fourier filter is active.

Figure 5.6 demonstrates that the $\cos^r \phi$ (with default $r = 2$) dependence of the meridional wave modes (first term in the curly bracket in Eq.(5.16)) causes the purely meridional waves $(0, y)$ to be damped very little at high latitudes. In particular, Figs. 5.6(b,d) show that the purely meridional $2\Delta y$ (or $(0, \pi)$) wave is hardly damped at all at $\phi = 60°$. While this does not introduce an instability, it does not quickly remove the high-order modes either. This can be confirmed by analyzing model runs of the baroclinic wave test in Fig. 5.7. The figure shows the vertical pressure velocity at the model level near 867 hPa at day 4 in CAM-FV for both the second-order (top row) and fourth-order (bottom row) divergence damping mechanism. Both the default CAM 5 damping coefficients (left column) and runs with doubled coefficients (right column) are depicted. The careful consideration of this test case indicates that a meridional wave is triggered shortly after the initialization, with wavelength around 6°. For the depicted $1° \times 1°$ grid spacing, this corresponds to $(0, \pi/3)$ in Figs. 5.2 and 5.6. Figure 5.7 illustrates the persistence of these waves in the vertical pressure

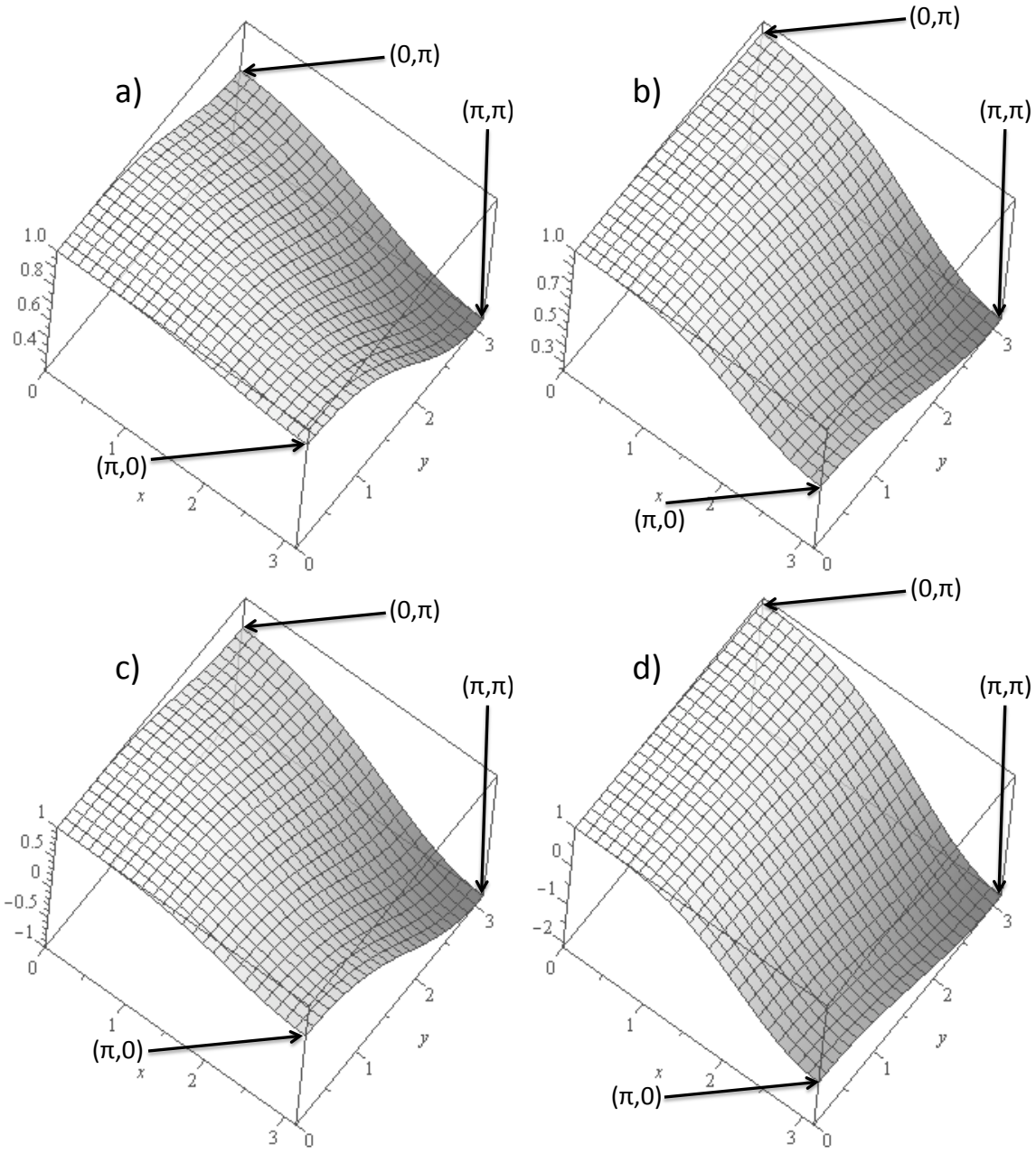

Figure 5.6: Amplification factor for the fourth-order damping Γ_4 with $r = 2$ (a,c) at the equator and (b,d) at $\phi = \pi/3 = 60°$. Top row (a,b): CAM 5 default configurations with $C_4 = 0.01$ and $\alpha = 1.33$. Bottom row (c,d): extreme case for $C_4 = 1/32$ and $\alpha = 1$. The axes are labeled as described for Fig. 5.2. Note the difference in scale.

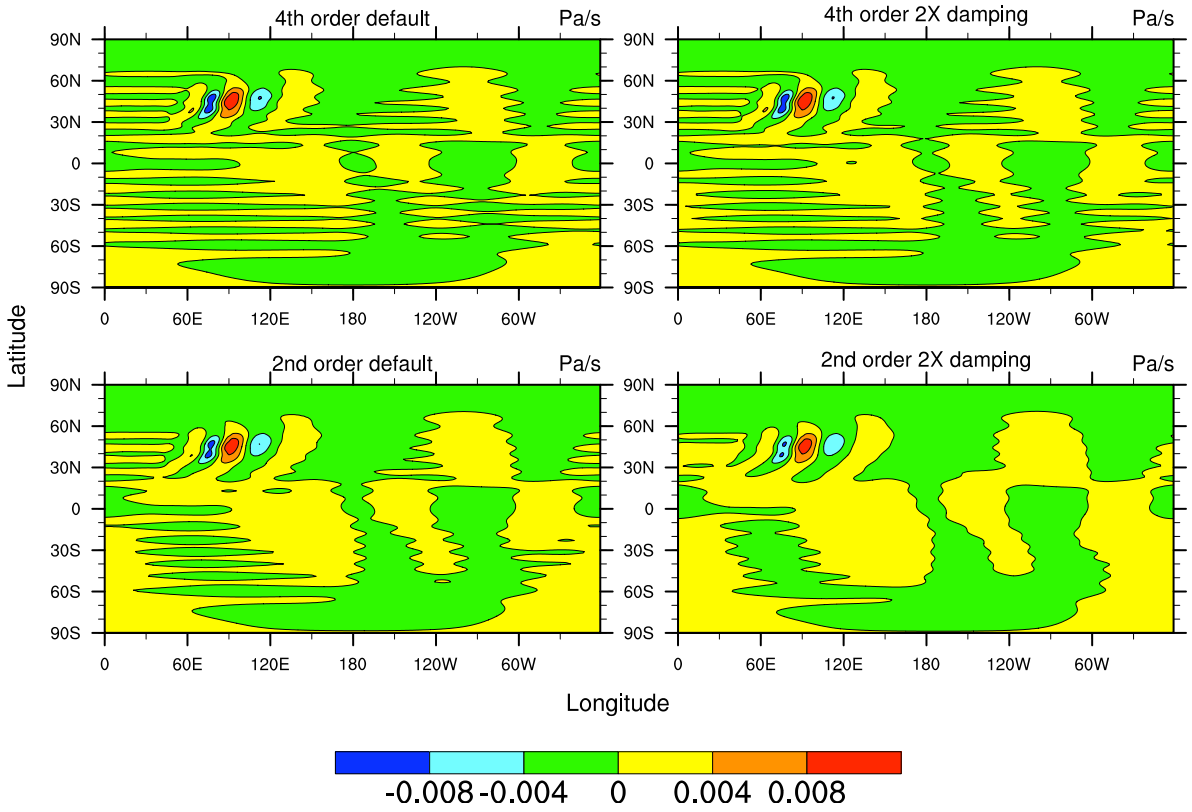

Figure 5.7: Vertical pressure velocity (in Pa/s) at day 4 at the CAM-FV model level near 867 hPa in the baroclinic wave test. The vertical velocity is closely related to the divergence, and at the model levels is not interpolated, so the meridional waves are most apparent. Left: The default fourth-order damping $r = 2$ employs $C_4 = 0.01$, the default second-order $r = 0$ uses $C_2 = 1/128$. Right: the 2X dampings use $C_4 = 0.02$ and $C_2 = 1/64$. The resolution is $1^\circ \times 1^\circ$ with 26 vertical levels.

velocity despite a doubling in the magnitude of the damping coefficients. The default second-order damping does not remove these waves either, but a simple doubling of the coefficient C_2 removes most of their effects. However, this comes at the cost of damping the resolved large-scale signal as well which might be unacceptable from a physical viewpoint.

To understand the damping characteristics at the equator, we can evaluate the amplification factors (5.11) and (5.16) for this particular example with $\alpha = 1$. For the default CAM-FV values $C_4 = 0.01$ and $C_2 = 1/128$ with a meridional wavelength of 6° the amplification factors are $\Gamma_4 = 0.99$ and $\Gamma_2 = 127/128 = 0.9921875$. If the 6°

wave is introduced at time step $n = 0$, then it would take approximately until $n = 70$ and $n = 90$ time steps for the fourth-order and second-order damping to damp the wave to half its original amplitude, respectively. When the damping coefficients are doubled as displayed in Fig. 5.7 (right column) this corresponds to $\Gamma_4 = 0.98$ and $\Gamma_2 = 63/64 = 0.984375$. These values require approximately $n = 35$ and $n = 45$ time steps for the fourth-order and second-order divergence damping to reduce the wave's amplitude by half (at the equator).

The apparent inability of divergence damping, and in particular fourth-order divergence damping, to adequately damp these small-scale modes is not immediately intuitive. An understanding can be gained by again considering Fig. 5.6. Note that along the line $x = 0$ the damping coefficients for both forms of damping is maximal, i.e. the amplification factor at $(0, y_0)$ is greater than at (x, y_0) for any $x \neq 0$. Physically this means that of all the modes damped by divergence damping, the purely meridional waves will be damped the least, whereas modes with mixed directions will be damped more adequately.

To understand why the second-order damping is more effective at removing these purely meridional waves, we must consider the effect that changes in latitude have on the amplification factors. Using the example from above but now at the high latitude of $\phi = \pi/3 = 60°$, the amplification factor for the 6° purely meridional wave is $\Gamma_4 = 0.9975$ which requires $n = 280$ time steps to damp the wave adequately for the default value of $C_4 = 0.01$. When using $C_4 = 0.02$, the amplification factor is $\Gamma_4 = 0.995$ which requires approximately $n = 140$ time steps to halve the amplitude of the 6° purely meridional wave. The second-order divergence damping employed in the runs illustrated in Fig. 5.7 (bottom row) uses Eq. (5.9) so that the amplification factor for purely meridional waves are independent of latitude, and thus only require

approximately $n = 90$ or $n = 45$ time steps for $c = 1/128$ and $c = 1/64$ to reduce the amplitude by half. Hence, it is this latitudinally dependent weakening of the fourth-order damping that allows the meridional waves to remain undamped for so long. In an effort to efficiently remove these modes and to obtain a damping coefficient meant to damp physical modes of a given size, regardless of latitudinal location and resolution, a modified fourth-order damping coefficient with $r = 0$ could be considered.

While it is not likely that such a modified formulation completely eliminates the meridional waves displayed in Fig. 5.7, it should damp these waves more effectively than the previous formulation. However one can also notice that the instability present at $k_\lambda \Delta\lambda = \pi$ and $k_\phi \Delta\phi = \pi$ will then be stronger in this case. This $1/\cos^4\phi$ instability near the poles will be stronger than the polar Fourier filter is designed to remove, so additional application or strengthening of the Fourier filter would be required. This is due to the current formulation of the damping coefficients in the Fourier filter itself. The coefficients (Eq. (B.1)) are proportional to $\cos^2\phi$, and can remove an instability in the zonal direction that depends on $1/\cos^2\phi$ which is the case for $r = 2$. Γ_4 with $r = 0$ presents a unique problem in that there is an additional $1/\cos^2\phi$ instability in the mixed direction, i.e. it is no longer the case that only zonal wave numbers become unstable near the poles. This implies that a simple application of the Fourier filter may not be sufficient to maintain stability.

5.4.3 Direct comparison of second-order and fourth-order divergence damping

As a final summary, Fig. 5.8 provides a direct comparison of the second- and fourth-order damping characteristics with the amplification factors Γ_4 with $r = 2$, and Γ_2 with $r = 0, 1$ at the (a,c) equator and (b,d) $|\phi| = 60°$. The amplification factors are plotted for identical wave numbers in both directions along the x-axis

where Δx is a placeholder for both $\Delta\lambda$ and $\Delta\phi$. In Figs. 5.8a,b the default CAM 5 Γ_4 and Γ_2 formulations with $C_4 = 0.01, r = 2$ and $C_2 = 1/128, r = 0$ are compared for the default aspect ratio $\alpha = 1.33$. In addition, Figs. 5.8c,d compare the extremal values (region of marginal stability at the equator) with aspect ratio $\alpha = 1$ for Γ_4 with $C_4 = 1/32, r = 2$ and Γ_2 with $C_2 = 1/4, r = 1$. The reason for evaluating the latitudinally dependent $r = 1$ case for the second-order damping instead of the default $r = 0$, is because the fourth-order divergence damping with $r = 2$ has the same area-dependence of the damping coefficient built-in.

Figures 5.8a,b show that the fourth-order damping is significantly stronger at the smallest scales. However, any amplification factor below 0.95 damps out the specified modes very effectively for long-term simulations since the damping is applied at each time step. Therefore, the damping rates of 0.3 or 0.85 in (b) for the $2\Delta x$ mode are not very different from each other in long climate runs. In general, we see that both forms of damping effectively eliminate the small-scale features such as the 2, 3, 4 Δx waves. The difference in the speed of the removal is evident, but is expected to play a minor role in climate simulations. However, this difference is important for data assimilation applications similar to the ones employed by the CAM Data Assimilation Research Testbed (CAM-DART) (see Anderson et al. (2009)) where the unbalanced nature of the model repeatedly introduces small-scale waves that must be damped out quickly. For this application of CAM (as well as for numerical weather prediction) the fourth-order damping mechanism is much more effective at small scales, while hardly influencing the well-resolved wave modes. This, combined with our observations for the purely meridional waves, explains recent observations that CAM-DART with fourth-order divergence damping adequately removes small-scale waves in the zonal direction (which is not the case for second-order damping),

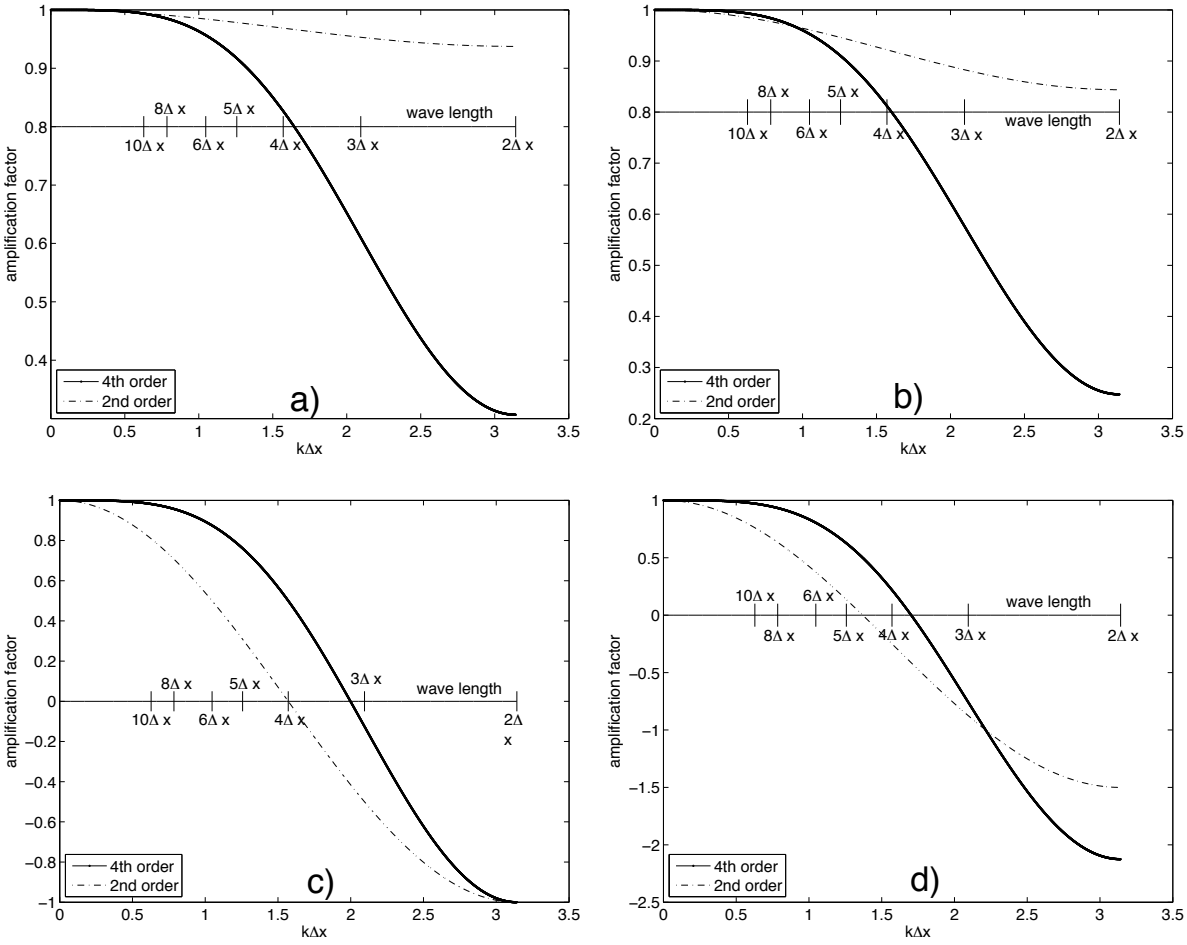

Figure 5.8: Scale-selective nature of the second and fourth-order divergence damping with $k_\lambda \Delta\lambda = k_\phi \Delta\phi$ along the x-axis. Top row (a,b): default CAM 5 with aspect ratio $\alpha = 1.33$ for Γ_2 ($r = 0$) with $C_2 = 1/128$ and Γ_4 ($r = 2$) with $C_4 = 0.01$. Bottom row (c,d): extreme cases using $\alpha = 1$ for Γ_2 ($r = 1$) with $C_2 = 1/4$ and Γ_4 ($r = 2$) with $C_4 = 1/32$. (a,c) are at the equator, (b,d) are at the latitude of $\phi = \pi/3 = 60°$.

but maintains some noisy meridional waves in the polar regions (see Lauritzen et al. (2011a)).

Figure 5.8b also shows that for modes larger than $6\Delta x$ the second-order divergence mechanism at $\phi = 60^\circ$ becomes stronger than the fourth-order scheme. The damping is only slightly stronger, but since the effect of the amplification factor is exponentially scaled, small differences near unity have major impact. In addition, these scales are well-resolved and have physical relevance. If the second-order mechanism damps them more, the effects are more likely to be evident in simulations. Overall, the fourth-order divergence damping or even high-order damping schemes are more scale-selective and more aggressive at removing the smallest scale waves while providing less damping at the larger modes. On the downside, higher-order schemes lead to a very restricted region of stability when applied in explicit time-stepping schemes.

Figures 5.8c,d clearly show for the extreme case that the fourth-order divergence damping barely damps the longer wavelengths until they reach $10\Delta x$ size. In contrast second-order divergence damping damps all modes except those of the very largest wavelength. The strongly negative values (< -1) of the amplification factors in Fig. 5.8d are not necessarily a concern as this choice of C_4 lies at the edge of the equatorial stability region and should not be used in practice for high latitudes. Instead, plots (c) and (d) are meant to only illustrate the qualitative behavior of the two damping mechanisms.

Fourth-order divergence damping is implemented as an option not only in CAM 5, but also in other GCMs such as the forthcoming GFDL/NASA finite-volume dynamical core on a cubed-sphere grid (see Putman and Lin (2009)). Even sixth- and eigth-order divergence damping mechanisms have been tested with the finite-volume

algorithm on the cubed-sphere grid (S.-J. Lin and W. Putman, personal communication, 2010). Note that the cubed-sphere grid does not suffer from the convergence of the meridians, or equivalently discretization on the grid avoids the $1/\cos\phi$ singularity that appears in this analysis. The intent of the damping mechanisms is to remove small-scale waves to prevent an accumulation of energy at the smallest scales. The singularity introduced by the latitude-longitude grid at the poles forces a trade-off between instabilities at the smallest resolvable scale $(2\Delta\lambda, 2\Delta\phi)$ and the inability of the damping to efficiently remove small-scale meridional waves. With the latitude-longitude grid, there is no clear winner, and while it may seem more acceptable to retain small-scale meridional waves longer than desired, as opposed to the introduction of grid-scale instabilities, this raises the question whether or not the fourth-order damping is truly damping sufficiently.

5.5 Conclusions

A linear von Neumann analysis is applied to the divergence damping implemented in CAM 5. Although care is taken to follow definitions and notation used within the CAM-FV framework, the analysis performed is not specific to CAM-FV. This analysis is specific only to divergence damping applied on a latitude-longitude grid with an explicit time-stepping scheme. This type of analysis can easily be adapted to other models, especially to those on other rectangular grids.

Stability restrictions are derived for both the second- and fourth-order divergence damping coefficients with homogeneous (in angle) grid spacing. While these restrictions are valid at the equator, the general formulas for the amplification factors provide the freedom to consider restrictions at other latitudes. In addition, the stability constraint depends on the grid resolution aspect ratio α which is accounted

for in the derivation. All model simulations utilized an equal grid spacing in both horizontal directions with $\alpha = 1$. The paper also demonstrates that different values of α alter the derived stability restriction.

The vertical dependence of the second-order divergence damping in CAM-FV is investigated. While most model runs with typical pressure values of 2-3 hPa at the model top are not negatively affected by the artificial 'sponge layer', it adequately explains the diffusive characteristics of idealized CAM-FV simulations with low-lying model tops around $p_{top} = 273$ hPa. In general, the effect of a sponge layer on the model needs to be carefully considered, as near the poles this sponge layer becomes increasingly unstable, and can become a source of divergence, rather than a sink of it.

The validity of the derived stability restrictions on the damping coefficients is experimentally confirmed through gravity wave and baroclinic instability tests of CAM-FV. The dynamical core simulations indicate that the analysis is very accurate for linear flows. The theoretical analyses and model simulations suggest that the fourth-order divergence damping parameter should be restricted by $C_4 \leq 1/64$ for $\alpha = 1$ and $C_4 \leq 9/625$ for the CAM 5 default $\alpha = 1.33$ setting. In addition, the latitudinal dependence of the damping has been investigated. For the fourth-order divergence damping it is found that the control of the grid-inherent singularity at the pole sacrifices the efficient reduction of small-scale purely meridional waves. Employing a damping coefficient that neglects the latitudinal variation of the grid cell area will likely damp these meridional waves more effectively, but the polar singularity will then be more apparent.

Most of the issues raised in this paper appear to be dependent on the choice of the computational grid. This analysis quantifies part of the effect that the two singular

poles in a latitude-longitude grid have on the subgrid-scale dynamics. In order to extend this analysis, the same method will be applied to other grid formulations, such as the finite-volume cubed-sphere dynamical core which is in development at GFDL and NASA. While this grid is presumably an improvement over the latitude-longitude grid, it also has its own peculiarities that must be accounted for in an analysis of the divergence damping.

Other sources of diffusive behavior in CAM-FV or other GCMs include inherent numerical diffusion, the use of 'sponge layers' at the model top, and filters and fixers that are meant to remove spurious waves that do not have physical origin. This paper quantifies the effect of one of these processes on the dynamics of a GCM. As illustrated, the divergence damping introduced to maintain numerical stability has the potential to introduce instability which negates the intended effect. Careful consideration of these processes should be high priority in the development of future models, so that their spurious impact on climate or weather predictions can be minimized.

The results of this Chapter are reported in Whitehead et al. (2011b).

CHAPTER VI

Potential Vorticity: a diagnostic tool for general circulation models

6.1 Introduction

Much attention has been paid of late to the evaluation and accuracy of the dynamical cores of general circulation models (GCM). One of the key building blocks for these models is the advection scheme that passively advects the hundreds of tracers (Lamarque et al., 2008) used in climate studies. Tracer advection schemes implicitly rely on the accurate integration of the momentum equation because the advective winds are taken from this dynamic step. In addition, some models (e.g. Lin (2004) and Lin and Rood (1996)) use the tracer advection algorithm as a building block for integrating the momentum. The effects of this coupling on the interaction of small-scale structures warrants further quantification.

Investigations into the veracity of a model's tracer transport algorithm (see Lauritzen et al. (2011b)) are necessary to validate model performance. Typically, test cases are performed on a variety of modeling frameworks, isolating the effect of the advective transport via a series of tests with variable difficulty (Kent et al., 2011; Nair and Lauritzen, 2010; Jablonowski et al., 2008a). These tests have prescribed dynamical fields like prescribed wind velocities, and omit the parameterized physics, concentrating on the advection algorithm which is the building block for the dynamical core.

In a different approach, Rasch et al. (2006) closely monitored the effect of different tracer routines on climate related constituents, using the full physics parameterization package available in the National Center for Atmospheric Research (NCAR)'s Community Atmosphere Model (CAM) version 3.0. Rasch et al. (2006) considered three of the dynamical cores available in CAM (named for the discretization method of the prognostic equations): finite volume (CAM-FV), spectral-transform Eulerian (CAM-EUL), and spectral-transform semi-Lagrangian (CAM-SLD). They find that with the same physics, the evolution of tracers is greatly effected by the choice of dynamical core and hence the choice of the advection algorithm. This Chapter is meant to clarify the symbiotic relationship between dynamics and tracer algorithms within each of the four dynamical cores in CAM 5.1, shedding some light on the results of Rasch et al. (2006).

In Williamson (2007) it is noted that employing two different numerical schemes for dynamics and tracer advection "is not entirely satisfactory". Joeckel et al. (2001) highlighted this concept, arguing that for accurate chemistry transport, the discrete advective continuity equation should reduce to that used for the transport of mass (dynamics). This restriction on the design of a dynamical core was one of the primary considerations in the design of CAM-FV (Rood, 2011; Lin, 2004; Lin and Rood, 1996). The importance of maintaining consistency between dynamics and tracer advection is investigated further in Lee et al. (2004); Zhang et al. (2008); Lauritzen et al. (2011b). The current Chapter develops a quantifiable test that can be used to measure this 'consistency'.

One of the fundamentally conserved quantities in the atmosphere, potential vorticity (PV), provides the opportunity to measure the consistency between the dynamics

and the tracer transport of a model. Consider the equations of motion given by:

$$\frac{\partial \boldsymbol{u}}{\partial t} + \boldsymbol{u} \cdot (\nabla \boldsymbol{u}) + 2\boldsymbol{\Omega} \times \boldsymbol{u} + \frac{1}{\rho}\nabla p + \nabla \Phi = \mathcal{F} \tag{6.1}$$

$$\frac{\partial \theta}{\partial t} + \boldsymbol{u} \cdot (\nabla \theta) = \mathcal{G} \tag{6.2}$$

$$\frac{\partial \rho}{\partial t} + \nabla \cdot (\rho \boldsymbol{u}) = 0 \tag{6.3}$$

where the three-dimensional winds are given by $\boldsymbol{u}$, the density is ρ, the pressure p, the rotation vector $\boldsymbol{\Omega}$, the geopotential Φ, and the potential temperature θ. $\mathcal{F}$ and $\mathcal{G}$ represent source terms that include diabatic and frictional effects which are not treated directly in the dynamical core. The system is closed by including an equation of state such as the ideal gas law:

$$p = RT\rho \tag{6.4}$$

where R is the dry air gas constant, and the temperature T is related to the potential temperature via

$$\theta = T\left(\frac{p_0}{p}\right)^{\kappa} \tag{6.5}$$

where $p_0 = 1000$ hPa is a reference pressure, and $\kappa = R/C_p$, C_p being the heat capacity of dry air at constant pressure. Neglecting $\mathcal{F}$ and $\mathcal{G}$ one can show that Ertel's potential vorticity, defined as

$$q = \frac{1}{\rho}(\nabla \times \boldsymbol{u} + 2\boldsymbol{\Omega}) \cdot (\nabla \theta), \tag{6.6}$$

is conserved following the adiabatic and frictionless flow (Ertel, 1942; Hoskins et al., 1985; Salmon, 1998; Gibbon and Holm, 2010), i.e.,

$$\frac{\partial q}{\partial t} + \boldsymbol{u} \cdot \nabla q = 0. \tag{6.7}$$

If the hydrostatic and shallow-atmosphere approximations are made, as is the case for models based on the primitive equations, the isobaric version of (6.6) is

$$q = -g(f\hat{\boldsymbol{k}} + \nabla_p \times \boldsymbol{v}) \cdot \nabla_p \theta \tag{6.8}$$

where $\hat{\boldsymbol{k}}$ is the vertical unit vector, $f = 2\Omega$ is the Coriolis parameter, $\boldsymbol{v}$ is the horizontal velocity field, and ∇_p is the three-dimensional gradient operator applied on levels of constant pressure (Hoskins et al., 1985). Hence if we consider initial data $\boldsymbol{u}_0, \theta_0$ for (6.1), (6.2), and (6.3) with a corresponding initial PV q_0 for (6.7) given by (6.6), then the PV advected by (6.7) is identical to PV computed via (6.6) from $\boldsymbol{u}$ and θ (solutions to (6.1), (6.2), and (6.3)). Therefore a model that purports to maintain consistency between tracer advection and the integration of the dynamics equations, should ensure that a tracer initialized as PV, is identical to PV computed from the dynamic variables (wind and potential temperature). Note that although this is true for the continuous equations, when discretization is applied the smallest scales are truncated and the scale interaction determined by the nonlinearity in (6.1) cannot be imitated by the linear tracer advection equation (see Babiano and Provenzale (2007) and Ohkitani (1991) for a discussion of this problem for incompressible flow in two dimensions).

In this Chapter, we will use the baroclinic wave test case described in Jablonowski and Williamson (2006a) to consider the analytic prescription of potential vorticity as a tracer (tracer PV) following (6.7), and compare this tracer's evolution with the computation of potential vorticity based on the dynamical variables of motion (dynamic PV) following the equations of motion (6.1), (6.2), and (6.3). We propose several methods for measuring the consistency of a model using the tracer PV and dynamic PV as test fields. Particular attention is paid to the CAM 5.1 framework

with its four dynamical cores: CAM-FV, CAM-SE, CAM-EUL, and CAM-SLD, and to CAM-FV in particular as this is the model version used in the current Coupled Model Intercomparison Project (CMIP5, see http://cmip-pcmdi.llnl.gov for details).

Comparisons between dynamic PV and trace constituents is not a novel idea. Zapotocny et al. (1996) compare the dynamically computed PV with a trace constituent that should (ideally) maintain an initially defined relationship with the PV. Their work focused on the comparison of four different model configurations, two from the University of Wisconsin (UW) global hybrid isentropic-sigma ($\theta - \sigma$) model and two configurations from NCAR's Community Climate Model 2 (CCM2, a predecessor of CESM1.0). The current work can be considered an extension of that study to a simpler test that is reproducible across modeling frameworks.

This Chapter will proceed as follows. Section 6.2 provides limited descriptions of the dynamical cores considered in this Chapter. Section 6.3 reviews the nature of potential vorticity as a dynamic tracer. Section 6.4 defines some quantitative measures of model consistency, including some comparison between the various dynamical cores of CAM 5.1. Section 6.5 compares these results to a model run at high resolution, and comments on the balance between accuracy, consistency, and the impact of necessary dissipation. The final section is relegated to conclusions and suggestions for further work and intercomparisons. The explicit calculation of the initial PV, and a description of the discrete computation of diagnostic PV as well as validation for this method are included in the Appendices.

6.2 Description of the four CAM 5.1 dynamical cores

The versatility of CAM's framework is displayed in the work of Rasch et al. (2006) wherein three dynamical cores are compared, while using the same physics package.

We take a similar approach, comparing the consistency of each of the four operational dynamical cores in CAM version 5.1, while omitting the physics parameterizations. This test case is not restricted to the model CAM however, and the simplicity of its construction makes it amenable for testing the consistency of other models.

As with other current GCM's, the dynamical cores in CAM employ some filters and explicitly added diffusion (see Jablonowski and Williamson (2011)) that must be accounted for. As detailed in Jablonowski and Williamson (2011); Neale et al. (2010) there are many different types of filters, fixers and other diffusion added to each of the dynamical cores in CAM. It is worth considering the effect of these dissipative forces on the consistency between the dynamics and tracers. We do not explore every possible form of dissipation or mixing process in CAM, but do consider how variations in certain aspects of the explicitly added diffusion may affect consistency.

6.2.1 CAM-FV

The finite volume dynamical core (CAM-FV) and its corresponding tracer transport algorithm are both based on the flux-form semi-Lagrangian scheme of Lin and Rood (1996). The method is a dimensional splitting technique that relies on the one-dimensional finite volume methods akin to the van Leer type monotonic methods (van Leer, 1974, 1977) or the Piecewise Parabolic Method (PPM, Colella and Woodward (1984)). The extension of this tracer advection algorithm to the shallow water equations is carried out in Lin and Rood (1997) with further application to three-dimensional hydrostatic motion introduced in Lin (2004).

CAM-FV is explored in greater detail in this study, in part because it is the default, operational configuration in CAM 5.1 (Neale et al., 2010). The emphasis on CAM-FV is also due to the versatility of the dynamical core, i.e., the flux-form semi-Lagrangian method allows for a variety of configurations both in the dynamics and

in the tracer routines. For instance, there are several one-dimensional finite volume methods (van Leer, 1977; Colella and Woodward, 1984) that can be considered for the dynamics and tracers (see Kent et al. (2011) for a brief overview of these options), and these can be interchanged, i.e., the dynamics can use a different operator than the tracer algorithm. The effect of explicitly added diffusion (and the stronger dissipative 'sponge layer) can be considered more readily in CAM-FV because a better understanding of the impact of divergence damping has recently been achieved (see Chapter V).

6.2.2 CAM-EUL

The spectral transform Eulerian dynamical core (CAM-EUL) is built on a Gaussian grid distinct from the latitude-longitude grid employed by CAM-FV. The momentum equation is formulated in vorticity-divergence form, then using spherical harmonics, the prognostic variables are cast into spectral space and integrated forward in time with a 3-time level Leapfrog method. The vorticity and divergence are then inverted to obtain the corresponding velocities. A fourth-order diffusive term is added for stability purposes (see Jablonowski and Williamson (2011) for details regarding the added stability preserving diffusive terms). A second-order diffusion is added near the model top to produce the 'sponge layer'. CAM-EUL uses different methods for the advection of tracers and the evolution of the dynamics. In particular, it employs a monotonic semi-Lagrangian advection scheme that is dimensionally split in the horizontal and vertical directions. This is in contrast to more consistent paradigms in CAM-FV and CAM-SLD.

6.2.3 CAM-SLD

CAM-SLD is based on a semi-Lagrangian, shape preserving advective algorithm on the same Gaussian grid as in CAM-EUL. The dynamics and tracer transport are then both based on the same premise, although conservation is not guaranteed in the dynamics and the tracer transport is performed in a single three-dimensional step with no dimensional splitting. The dynamic variables are cast in spectral space akin to CAM-EUL, but are integrated in time via a 2-time-level semi-Lagrangian semi-implicit time-stepping mechanism. To avoid dispersive errors inherent to the spectral transform spatial discretization, a fourth-order hyperdiffusion term is included in the dynamic calculation.

6.2.4 CAM-SE

The spectral element (SE) component of CAM (Taylor, 2011) is built on the cubed sphere to avoid the singularities generated by a latitude-longitude grid near the poles. CAM-SE is built on the spectral element approach developed initially for the shallow water equations in Taylor et al. (1997) and later expanded to the hydrostatic atmosphere (see Neale et al. (2010) for further references). The dynamics and tracer transport are treated similarly in CAM-SE, and an explicit fourth-order hyper-diffusion is added to both as well as second-order diffusion near the model top to maintain stability.

6.3 Potential Vorticity as a dynamic tracer

With the goal of comparing dynamic and tracer PV among the four dynamical cores described in the previous section, we consider the baroclinic wave test case described in Jablonowski and Williamson (2006a). This test case starts with an initialized steady state and small amplitude zonal wind perturbation centered in the

Northern Hemisphere. A baroclinic wave develops from this perturbation in the Northern Hemisphere after 4 days of integration, breaking at day 9. This provides an ideal situation to consider both the development of linear, yet realistic flow prior to the wave breaking, and nonlinear, multi-scale flow afterward. We develop a series of tools that allow us to consider the consistency of each model both in the linear and nonlinear regimes.

The PV for the baroclinic wave (with initial conditions given in Appendix C) qualitatively imitates the temperature field. As such, one can identify the development and breaking of the wave in the PV field. This allows for a distinction between the linear effects in tracer advection versus the dynamic (nonlinear) evolution of the PV at and after wave-breaking occurs. The wave-breaking is graphically identified near day 8 as seen in Fig. 6.1 where new contour levels are identified with respect to day 7. After this breaking occurs we observe the interaction of the mean flow with the spin up of much smaller scales. Turbulence theory indicates that these interactions across scales are a by-product of the nonlinear terms in the equations of motion. We make the distinction between the linear and nonlinear flow, because the tracer advection algorithm will always be integrating the linear equation (6.7) while the integration of the dynamics is effectively integrating (6.7) where $q = q(\boldsymbol{u})$ is an active scalar, i.e. the dynamics are a nonlinear problem.

The possibility of using maps of potential vorticity as a diagnostic tool was popularized by McIntyre and Palmer (1983); Hoskins et al. (1985), among others. Moeller and Montgomery (2000) suggested that anomalies in potential vorticity may be tracked to understand the generation and evolution of tropical cyclones. Using PV as a diagnostic tool has not taken significant root in the community however, primarily as a consequence of the difficulty in computing the vertical derivative of the potential

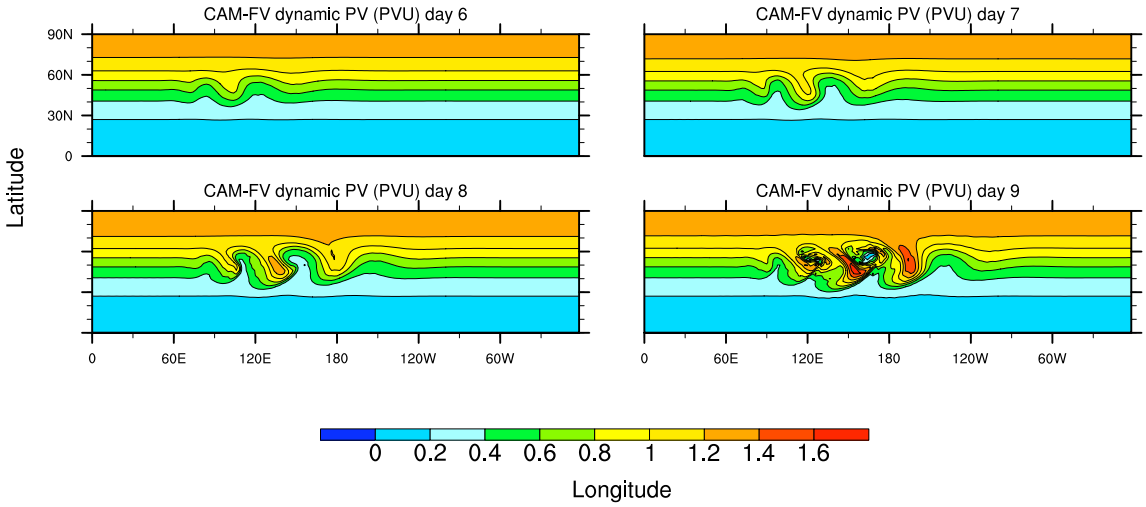

Figure 6.1: Evolution of the baroclinic wave in the dynamic potential vorticity field interpolated to 850 hPa. PVU is potential vorticity units and is defined explicitly in Section 6.4.2.

temperature (see Appendix D for a brief discussion of this).

Due to its unique conservation property following adiabatic, frictionless flow, potential vorticity has been extensively studied. Analytic properties of PV are investigated in Haynes and McIntyre (1987). It is found that even in the presence of friction and diabatic heating, PV is constrained between isentropic surfaces. Hence even in the presence of dissipative mechanisms such as filters, fixers and numerical diffusion (see Jablonowski and Williamson (2011)), the PV should satisfy this condition, yielding a test to verify whether these dissipative mechanisms do represent physical processes. Such a test would be a simple extension of the present study.

6.4 Model comparisons

6.4.1 Paradigms of consistency

There are two basic premises for quantifying the consistency between dynamics and tracer transport of a model. The first premise involves point to point comparisons, i.e. when comparing two data sets it is assumed that both lie on the same grid

so that error norms or scatter plots (as explained in the following subsection) can be determined exactly. This is a valid assumption provided we are comparing the tracer PV and dynamic PV within the same model framework, and at the same resolutions, and may also be considered viable if accurate interpolation methods from one grid type or resolution are known. Such is not generically the case, especially in the presence of differing vertical discretizations and grids (Ziv and Alpert, 1994). The second premise is that data on differing grids must be compared, and the influence of interpolating methods should be avoided. This is of particular interest when the flow is nonlinear, because errors due to interpolation should be more significant.

One of the common difficulties in analyzing data output from a GCM, is the dimensionality of the data sets. In the case of the baroclinic wave, we have two 4-dimensional variables in the form of the dynamic and tracer PV. It is difficult to graphically represent such a field, even as time snapshots. In addition, as discussed in Appendix D, the dynamic PV is not accurate near the vertical boundaries, in particular at the model top. Another issue arises in comparing the initial development of the baroclinic wave when the steady state is very nearly maintained throughout the atmosphere, and the wave is only affecting a small latitudinal strip in the northern hemisphere. To simplify comparisons between models and PV fields, we will interpolate the data from model levels to 850 hPa and consider the development of the wave by analyzing the latitudinal strip from 30° to 60° N.

Table 6.1 details the model configurations for each of the dynamical cores considered in this study. These comparisons are done at low climate resolutions of about $2^\circ \times 2^\circ$ or approximately 200 km grid spacing to indicate the effect that unresolved processes have on the consistency between dynamics and tracers. Each model was run with 52 vertical levels (twice the typical vertical resolution used in CAM4.0) in

order to accurately compute vertical derivatives in the calculation of dynamic PV (see Appendix D for more motivation of this choice). These levels are chosen at initial pressure levels that exactly interpolate between the 26 levels described in Appendix C of Jablonowski and Williamson (2006a).

Table 6.1: Model configurations for each of the four dynamical cores used in this study. In the spectral transform models $T85$ indicates the highest resolved wavenumber, 85. For CAM-SE, $ne16np4$ means that each face of the cubed sphere is divided into 16×16 elements with a fourth-order polynomial in each. There is no diffusion for CAM-FV, but fourth-order divergence damping is used (see Chapter V for details). The diffusion coefficients for the other three dynamical cores are for fourth-order hyper-diffusion.

Dynamical Core	**Horizontal Grid**	**Grid Size at equator**	**Dynamic time step (tracer time step)**	**Diffusion coefficient (m^4/s)**
CAM-SE	$ne16np4 \sim 2^\circ \times 2^\circ$	220 km	225 s (900 s)	6×10^{15}
CAM-SLD	T85	156 km	600 s (600 s)	1×10^{15}
CAM-EUL	T85	156 km	600 s (600 s)	1×10^{15}
CAM-FV	$2^\circ \times 2^\circ$	220 km	360 s (3600 s)	NA

6.4.2 Point to point comparisons: error norms, scatter plots and extreme values

The most frequent metric used in the analysis of numerical techniques is the discrete l^p norm of the error from an exact solution, i.e., if the model data is represented by q with an exact solution corresponding to q_T, then

$$l^p\{q\} = \left\{ \frac{I\left[(q - q_T)^p\right]}{I\left[(q_T)^p\right]} \right\}^{1/p} \tag{6.9}$$

defines the normalized l^p error of q where $I[\cdot]$ denotes the global integral (in this case, actually the integral over the latitudinal strip from 30° to 60° N at the interpolated pressure level 850 hPa) of the given quantity. The maximal norm $p = \infty$ then is equivalent to

$$l^\infty\{q\} = \frac{\max|q - q_T|}{\max|q_T|}. \tag{6.10}$$

There is no exact solution known for the baroclinic wave test, but we can consider the difference between the tracer PV and dynamic PV as a measurement of the

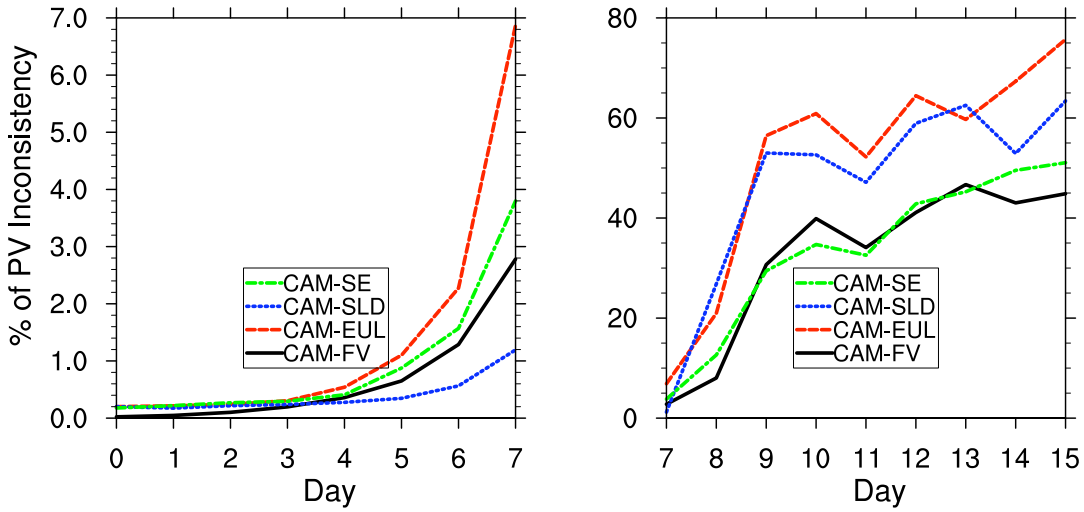

Figure 6.2: Evolution of the nomalized l^4 norm of the difference between dynamic and tracer PV for all four dynamical cores. The left figure shows the linear flow during the first 7 days of the test case, and the right figure shows the nonlinear flow for days 7 through 15. We consider the PV interpolated to 850 hPa contained in the region between $30°N$ and $60°N$. Note the difference in scale for the vertical axis.

lack of consistency in the model. A perfectly consistent model would have identical distributions of tracer PV and dynamic PV and hence the corresponding l^p norm would be due solely to the inaccuracy in the dynamic PV calculation (see Appendix D). For the dynamical cores considered here this error is minimal, so the evolution of consistency error can be considered independent of the dynamical calculation.

Traditionally $p = 2$ (least squares regression) or $p = \infty$ (maximal error norm) are used for measurements of model error. The l^2 error norm will not capture the detrimental effects of extreme differences on small scales, and the maximal error norm l^∞ will weigh these statistically rare events more than desired. Hence we consider the l^4 norm (a perfect interpolation between l^2 and l^∞) of the difference between the data sets. This provides an accurate measure of the overall error as provided by l^2, while including the effect of localized errors provided by l^∞. l^4 can also be interpreted as a measure of the kurtosis of the difference between tracer PV and dynamic PV, i.e. this measures the tendency of the error to originate from localized

regions as opposed to a global offset.

A plot of the normalized percentage l^4 error for CAM-FV, CAM-EUL, CAM-SLD, and CAM-SE is shown in Fig. 6.2. The model configurations are detailed in Table 6.1. 52 vertical levels were used. Even with the nominal higher horizontal resolution in CAM-EUL and CAM-SLD we observe that the dynamic and tracer PV are in less agreement after the wave breaks (right plot) than CAM-SE and CAM-FV. For the linear flow (left plot) CAM-SLD is the most consistent, but this changes suddenly when the flow becomes nonlinear. The semi-Lagrangian time-stepping used by CAM-SLD includes shape-preservation constraints to ensure monotonicity that will take full affect in the presence of nonlinearities in the dynamic equations. On the other hand, the linear tracer advection equation will not require as much limiting (and hence added dissipation) so that in a sense the dynamic PV will no longer be conserved following the flow, and so the differences between dynamic and tracer PV will grow. While all four dynamical cores employ dissipative sub-grid mechanisms, these affects are most apparent for CAM-SLD because of the dissipative nature of the interpolations in the semi-Lagrangian algorithm.

To see how the consistency error develops, note that in Table D.1, the $2^\circ \times 2^\circ$ CAM-FV initial dynamic PV calculation with 52 vertical levels yields an error less than 0.023%. Fig. 6.2 shows that when the wave is beginning to develop around day 4 or 5, the error is still minimal for all four dynamical cores (less than 1%). Even when the wave is fully developed at day 7, the inconsistencies for each model are moderate. After the wave breaks dynamic PV and tracer PV quickly separate as illustrated in the right plot in Figure 6.2. At day 15 the dynamics and tracers can no longer be considered closely related (45% error for CAM-FV and CAM-SE is poor, but 75% for CAM-EUL and 64% for CAM-SLD is significantly worse). Fig. 6.2

shows that consistency in nonlinear flow is not guaranteed for any of the dynamical cores, but it does not indicate whether this error is due to minor changes in the phase of the wave. This indicates the limitations of using the error norm to quantify the consistency of the model in the nonlinear regime.

One related, qualitative measurement that yields useful information for comparing PV is a scatter plot as shown in Figs. 6.3, 6.4, 6.5, and 6.6 (see also Zapotocny et al. (1996) for the use of similar scatter plots). The unit of measurement in all of these plots is the potential vorticity unit (PVU = $10^{-6} K \cdot m^2/(kg \cdot s)$). As mentioned earlier, we only consider data points from PV fields first interpolated to 850 hPa and located between 30° and 60° N latitutde. Each grid point has corresponding tracer PV and dynamic PV values. The horizontal axes in Figs. 6.3, 6.4, 6.5, and 6.6 correspond to the dynamic PV values at each grid point. The vertical axis is the tracer PV at the same grid point. Hence, in theory the scatter plots should follow the line, tracer PV=dynamic PV ($y = x$). Deviations from this line indicate errors in the consistency of the model.

Comparing these scatter plots to the l^4 error norms shown in Fig. 6.2, one can see that the separation of tracer PV from dynamic PV for all four models occurs as the dynamic PV develops larger extrema than the tracer PV. For CAM-FV this is intuitive. The dynamics of the system are governed by a diffusive finite volume formulation that diffuses the prognostic variables and hence the wind fields that are used in the advection algorithm. In the advective step, these diffused winds are used in the finite volume based tracer transport to advect the tracer PV. Hence, the tracers will have this (implicit) diffusion applied in two different ways, directly through the tracer transport algorithm, and indirectly as the winds used in the tracer transport are already diffused through the dynamic integration. The differ-

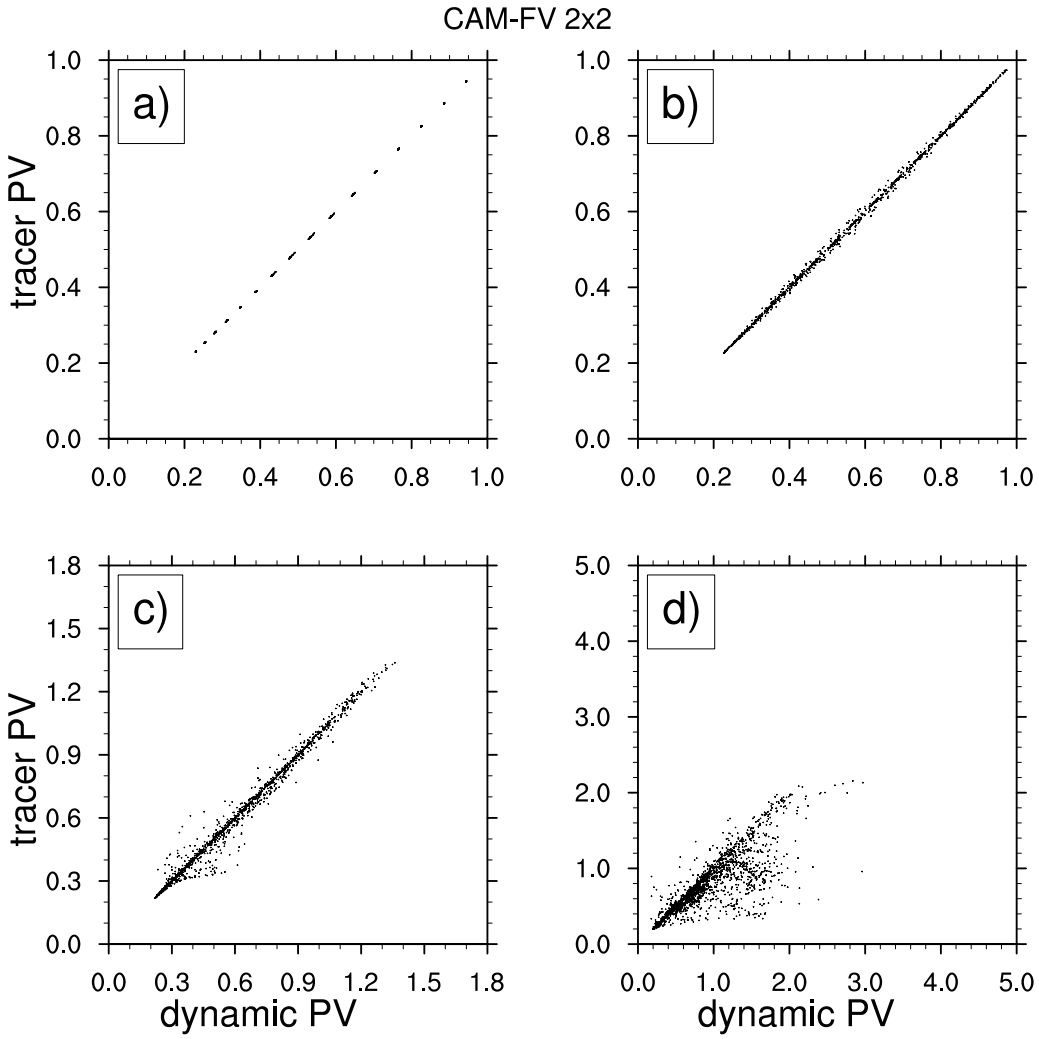

Figure 6.3: Scatter plots of the tracer and dynamic PV at days *a*) 1, *b*) 6, *c*) 8, and *d*) 12 for the model configurations given in Table 6.1. Any deviations from the line $y = x$ indicate differences between tracer PV and dynamic PV. Note the change in axis labels from days 1 and 6 to days 8 and 12.

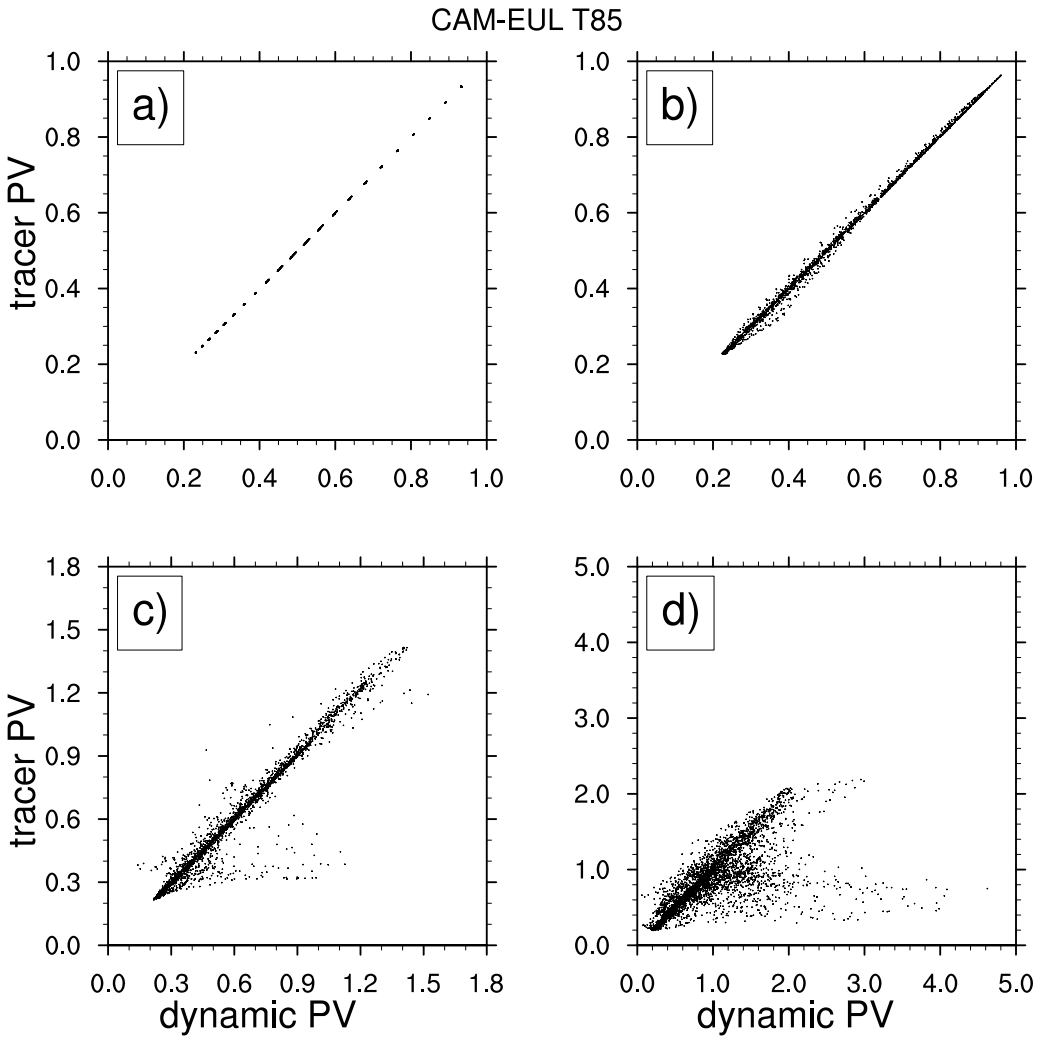

Figure 6.4: As Fig. 6.2 but for CAM-EUL at the model configuration given in Table 6.1.

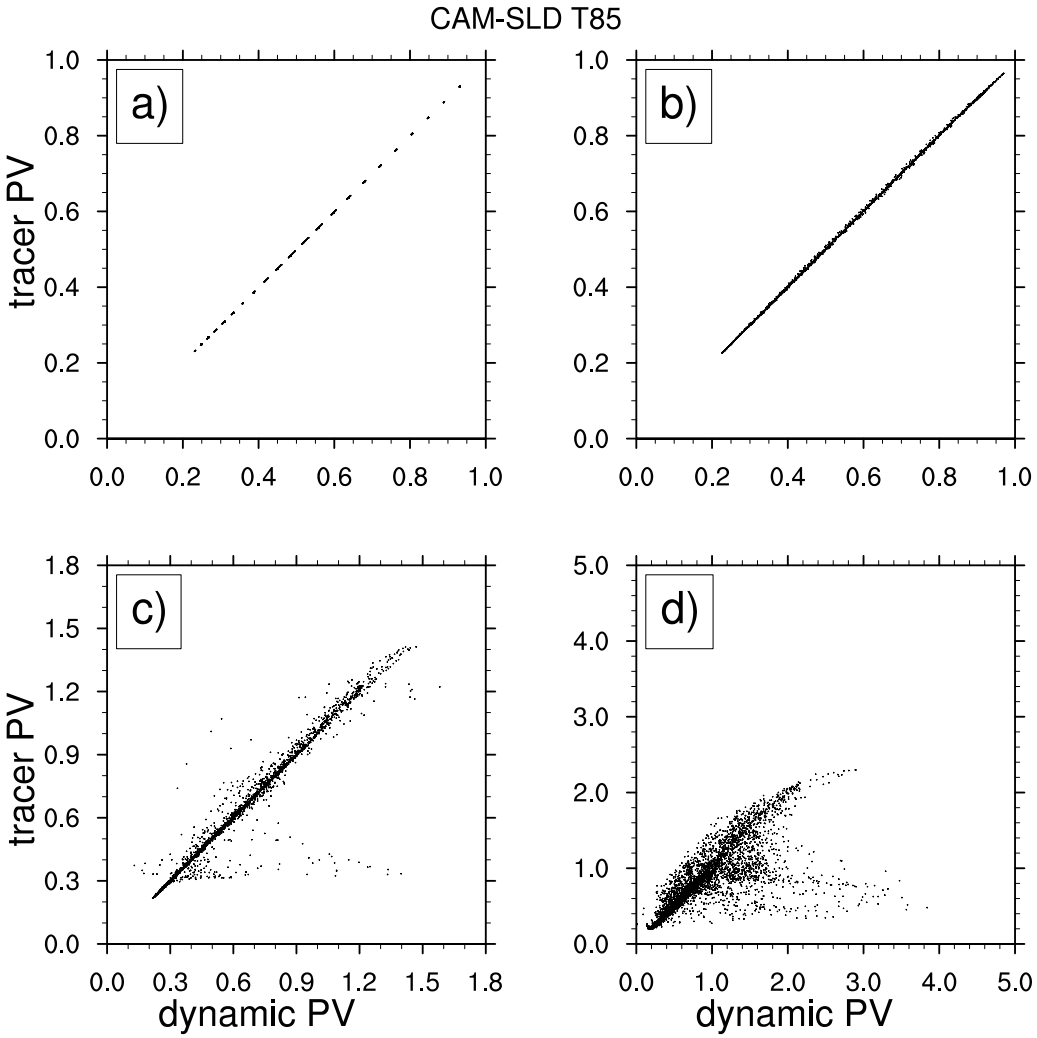

Figure 6.5: As Fig. 6.2 but for CAM-SLD at the model configuration given in Table 6.1.

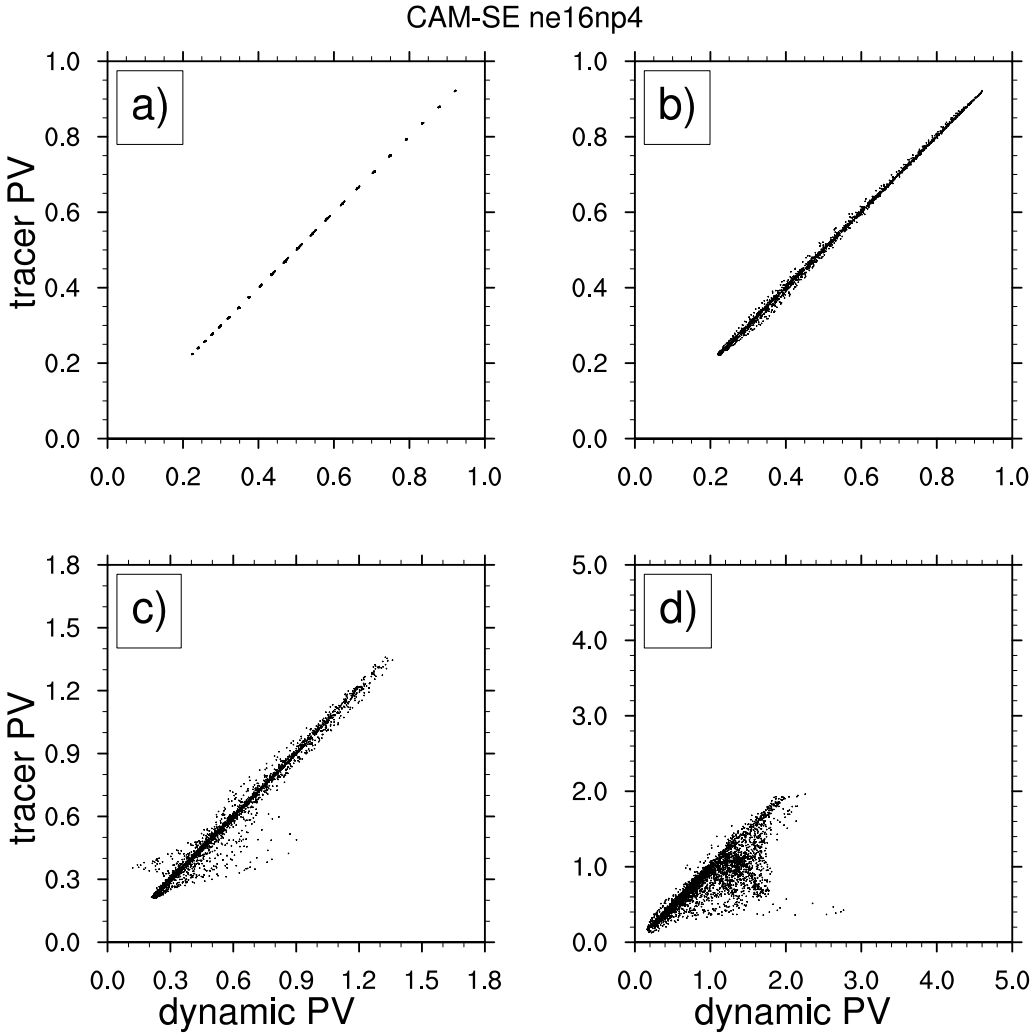

Figure 6.6: As Fig. 6.2 but for CAM-SE at the model configuration given in Table 6.1.

ence in CAM-EUL is more pronounced because the dynamics are maintained by the less diffusive spectral transform method, but the tracer is then advected with the diffusive semi-Lagrangian technique (with additional diffusion entering due to the dimensional splitting to follow vertical motion). Similar to CAM-EUL, the spectral transform spatial discretization in the dynamics of CAM-SLD allows dispersive errors to dominate despite the dissipative time-stepping used.

A fundamental reason for the extreme values of dynamic PV present in all four dynamical cores may lie in the inherent nonlinearity that the dynamic PV is representing. In the discretized version of (6.1), the nonlinear term and the corresponding interaction of scales will not be completely captured. Hence the large-scale flow may generate dynamic PV at a scale that falls below the resolution of the grid, and is represented as sharp gradients at the grid scale. This is part of the reasoning behind the proposed test in Gibbon and Holm (2010). In contrast the discretized equation for tracer PV, while truncating the smallest scales, remains linear implying that scale interactions are introduced through the flow field only and not in the tracer PV itself.

We observe that CAM-FV is significantly more consistent than CAM-EUL, and that the dynamic PV has more moderate extremes. This is most likely due to CAM-FV's monotonicity preserving model design, although the dimensional splitting allows for violations of the monotonicity constraint in two dimensions as shown in Kent et al. (2011). The interesting result of this analysis is how significant this difference is, the similarities between CAM-FV and CAM-SE, and that the consistency of CAM-SLD is highly dependent on the linearity (or lack thereof) of the flow.

Careful consideration of these scatter plots may yield some insights into the nature of the error observed in Fig. 6.2. One can see that by day 12 the scatter plots are skewed substantially toward large dynamic PV at small tracer PV values. This results

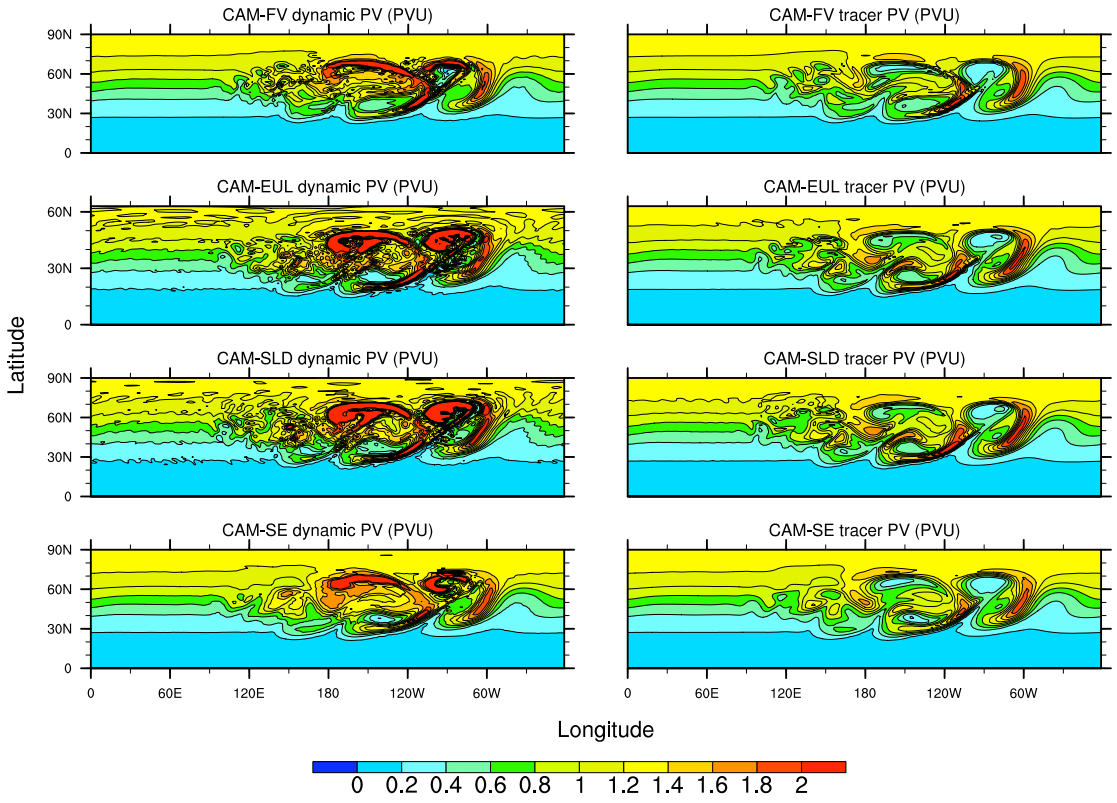

Figure 6.7: A snapshot at day 12 of the dynamic (left) and tracer (right) PV at 850 hPa for the four dynamical cores to illustrate the differences in their treatment of the dynamics and tracers. The models are run with the configuration described in Table 6.1.

in a substantial contribution to the error, and may be an indication of phase errors or intensification of extreme values in the dynamic computation, i.e. in regions where sharp gradients appear, large dynamic PV values can correspond to small tracer PV values via a small spatial shift. These scatter plots are not sufficient to draw definitive conclusions though.

Fig. 6.7 shows contour plots of the dynamic and tracer PV for all four dynamical cores. There are large dynamic PV values present in all four models, as well as the inherent noisy signatures in the CAM-EUL and CAM-SLD dynamic PV fields. One can see that minor phase errors in the PV fields would result in extreme differences as mentioned earlier. However, this does not appear to be the dominant reason for large dynamic PV and small tracer PV. Instead, one may observe that the regions near $68°N$, $170°W$ and $72°N$, $90°W$ have steep gradients in the tracer PV for all four models, and correspondingly extreme values in the dynamic PV. This effect appears consistently at other days as well, i.e. in localized regions where the tracer PV displays a steep gradient, dynamic PV tends to develop large values. This level of analysis does not indicate whether the tracer or dynamic PV is more physically relevant, but one can recognize that a flow that dictates such large dynamic PV values (proportional to large values of absolute vorticity) would lead to sharp gradients in a passively advected tracer. This does not explain however, why the tracer PV would not capture the same extreme values. As illustrated by the scatter plots described earlier this demonstrates that once the flow becomes nonlinear there is a fundamental difference in the treatment of dynamic and tracer PV that carries across any of the four numerical algorithms explored here. It is worth considering whether these differences are resolvable, i.e. is it possible to maintain consistency between dynamics and tracer advection as described in this Chapter, or is this a fundamental

issue of the discretization of all numerical models?

The significant differences in the dynamics observed in Fig. 6.7 are not unexpected, as at this low resolution a significant portion of the kinetic energy of the breaking wave will lie below the scale of the grid, and hence the dissipative sub-grid mechanisms of each model will have a strong influence on the flow's development. In this respect CAM-EUL and CAM-SLD have similar sub-grid dissipative methods, i.e. explicit hyper-diffusion applied following a spectral-transform integration of the equations. Although CAM-SE also uses hyper-diffusion to model the unresolved, sub-grid processes, both CAM-SE and CAM-FV treat have fundamentally different methods of discretization than the spectral transform dynamical cores. Fig. 6.7 illustrates the impact of these differences on the dynamical evolution of PV. An interesting observation gained from these comparisons is that despite the fundamental different treatments of the dynamic variables, the tracer advection schemes (right) give similar results. This might indicate the robustness of these models to produce statistically amenable results (at least for passive tracer fields) even in the presence of highly nonlinear flow.

From the argument presented above, it may be assumed that consistency between tracers and dynamics is not a necessary trait for dynamical cores, because in the end the tracer PV develops similarly. However Fig. 6.7 provides motivation for seeking consistency between the dynamic variables and tracer advection in a given dynamical core. Consider again the low in tracer PV present for all four models near $60°N$ and $160°W$. This low is not present in the dynamic PV for any of the models. The same phenomenon occurs at the same latitude, but at 90° west. In this case the dynamic PV of CAM-FV and CAM-SE retain a low, but it is barely visible due to the extreme values surrounding it. In CAM-EUL and CAM-SLD, this feature is dominated by the

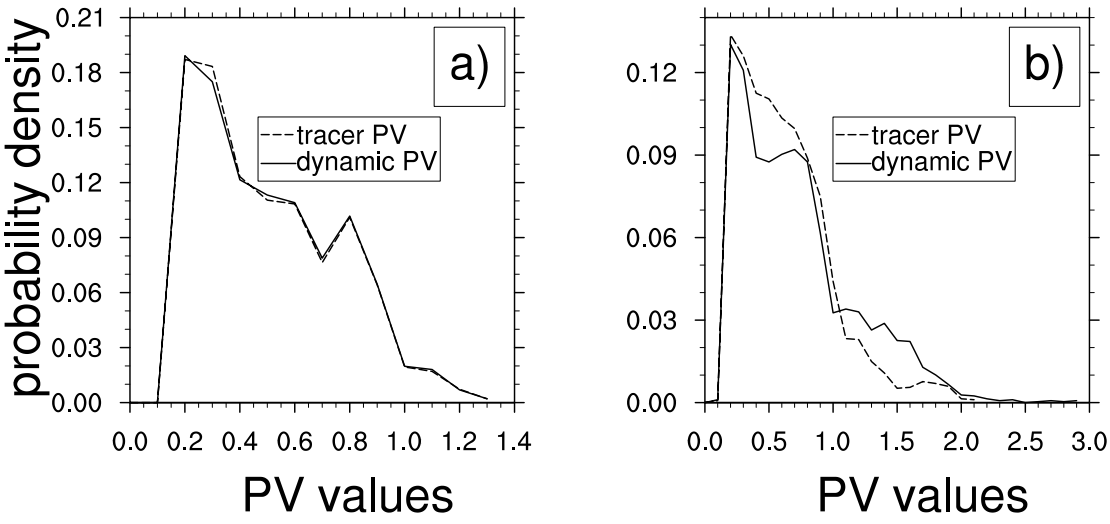

Figure 6.8: Probability Density Functions (pdf) for the dynamic and tracer PV at 850 hPa from a CAM-FV run as described in Table 6.1. This shows snapshots at days *a*) 8 and *b*) 12. The horizontal axis is in PVU.

extreme dynamic PV values. Such a drastic change between dynamics and tracers in these regions presents challenges for passively advected chemical constituents that should be correlated with PV.

6.4.3 Probability Density Functions

For a grid-independent graphical comparison between two fields, we construct a probability density function (pdf) for each. This provides a more generic comparison, and allows for minor phase errors that offset one simulation from another. However it may be argued that these phase errors have minor effects on climate. A pdf is constructed for the dynamic and tracer PV interpolated to 850 hPa in the latitudinal strip lying between 30° and 60°N by binning the PV into bins of size β. For the results shown here we choose $\beta = 0.1$. The pdf is constructed by computing the probability that the PV falls into each of these discrete bins.

Figure 6.8 shows the differences between the tracer and dynamic PV for the standard CAM-FV run. In linear flow, there is very little difference between the

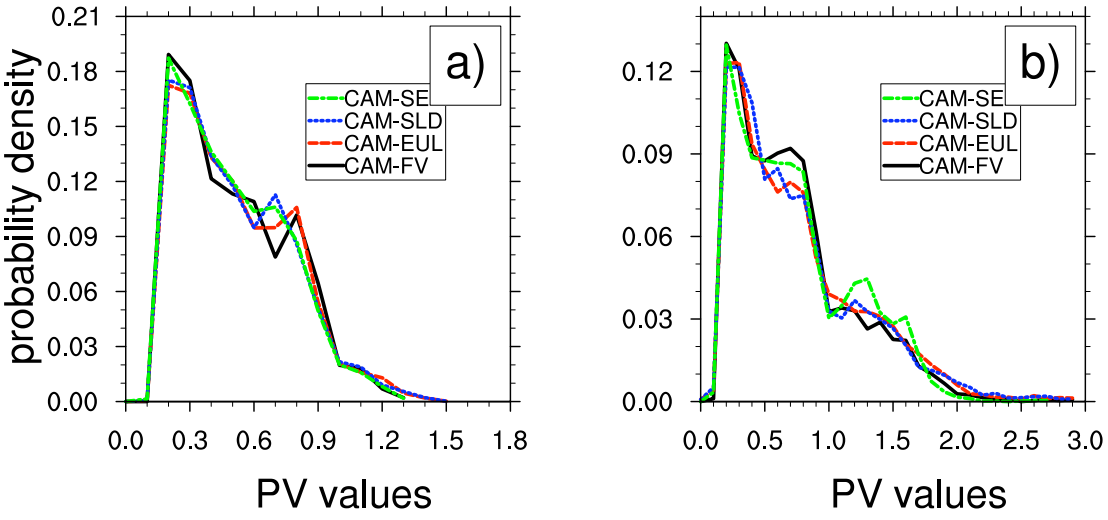

Figure 6.9: As in Fig. 6.8, but here a comparison of the dynamic PV for each of the four dynamical cores with configurations described in Table 6.1.

dynamics and the tracer, so we consider only the nonlinear regime. The snapshots here are at day 8 when the wave begins to break, and day 12 when the nonlinear term is in full effect. The same conclusions mined from the scatter plots, can be determined i.e., the tracer PV is significantly more likely to occur at smaller values, whereas the dynamic PV has a long tail toward the extreme. Note the smooth drop in the pdf for tracer PV at day 12, with only a small probability of PV greater than 1.0. In contrast, the dynamic PV maintains a reasonable probability of $1.0 \leq PV \leq 2.0$. Consulting Fig. 6.7, one can see that the dynamic PV has substantially more data points with these values near $60°N$, $160°W$ than the tracer PV, where a low with values near 0.5 occurs. This low in tracer PV corresponds to the greater probability seen in the pdf for PV near 0.5, indicating that these differences in the pdf for CAM-FV may be explained by disparities in this localized region.

Fig. 6.9 shows the dynamic PV of each model and Fig. 6.10 compares the tracer PV. The only significant difference between models at day 8 is the inclusion of a local minima for CAM-FV (for both the tracer and dynamic PV) near 0.7 that does

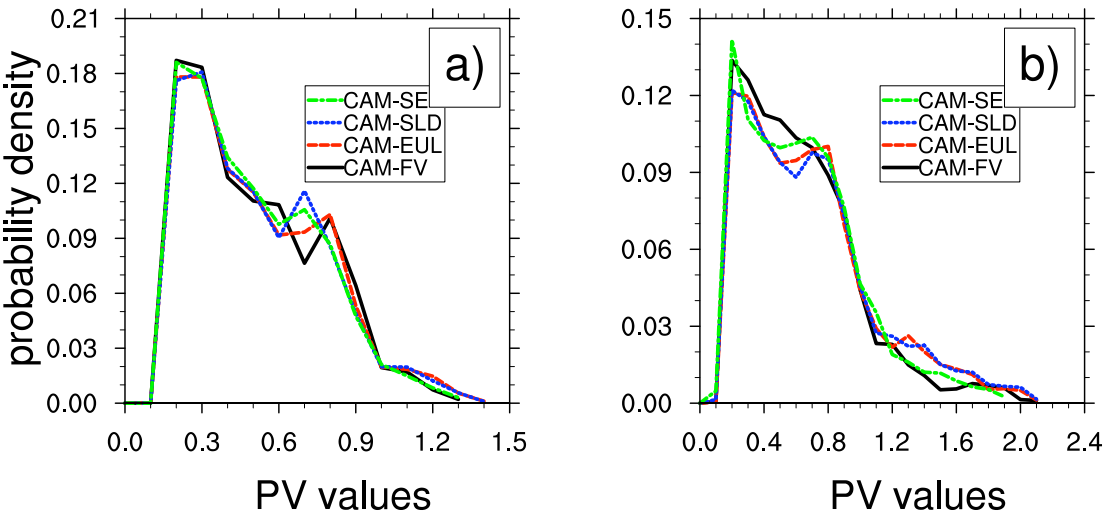

Figure 6.10: As in Fig. 6.9 except for tracer PV.

not appear for the other models. This offsets the local maxima that occur at this location for CAM-SE and CAM-EUL. This change in probability is not significant (only 3%), and overall it appears that the models compare favorably at this stage in the wave's development. The pdf of PV at day 12 (Figs. 6.9b and 6.10b) show that the general shape of the distributions is similar between models. For example the pdfs for dynamic PV appear to have the initial peak near 0.2 and then have a relatively agreeable slope that trails off to the higher values. A similar observation can be made for the tracer PV. Although it is apparent that the dynamic and tracer PV do not agree within each model.

All of the models maintain a high probability for PV at the smallest values and exhibit a sharp drop in probabilities thereafter. Smaller PV values are abundant in the initial state in the region of interest between $30° - 60°$ N at the 850 hPa level. Their high probabilities in Figs. 6.9 and 6.10 therefore reflect that the evolution of the dynamic PV field (Fig. 6.7) is still connected to its initial conditions. The drop in probability at the higher dynamic PV values in Fig. 6.9b is mimicked to a lesser degree by the PV tracer fields in Fig. 6.10b except the tracer distribution in

CAM-FV shows a gentler slope. We observe that the tracer PV for CAM-SE has a very high probability of occurring at the smallest values, but exhibits a significantly reduced probability in the larger PV range in comparison to the other dynamical cores. Even so, the pdf for tracer PV in CAM-SE and CAM-FV are quite similar, and tail off quickly at the higher PV values.

One feature that emerges from this comparison of the probability density for dynamic PV is the higher probability appearing in CAM-SE near 1.3 and 1.7. Returning to Fig. 6.7, we see again in the region near $60°N$, $160°W$, that CAM-SE has significantly more dynamic PV near these values than the other three models. CAM-EUL and CAM-SLD both have dynamic PV greater than 2 here, and CAM-FV has a noisy gradient that appears to vary rapidly with only a small portion near these PV values. This illustrates a significant point that can be made for all of the methods presented in this Chapter to measure the consistency of a model. Localized differences on PV fields can have a significant effect on the global measurements of inconsistency and error.

6.5 Dissipation, accuracy, and consistency

Figures 6.2 and 6.5 indicate that up to day 7 CAM-SLD is the most consistent of the four dynamical cores. One must recognize however that this is only one method of evaluating the model. In reality, for linear flow CAM-SLD is more diffusive than the other three dynamical core options explored here. This diffusion smoothes out the dynamics so that the tracer algorithm easily imitates the dynamical PV. Once the wave develops the implicit dissipation added via the semi-Lagrangian integration and the decentering mechanism with decentering coefficient $\epsilon = 0.2$ as explained in Jablonowski and Williamson (2011) cannot control the dispersive nature of the

spectral-transform method and as seen in Fig. 6.7, the dispersive errors dominate the dynamics. It can be argued that the increased dissipation for CAM-SLD in the linear flow, is good for the model's consistency, but this would not necessarily be good for the accuracy of the integration.

The effects of dissipation on consistency and accuracy are most easily explored via the CAM-FV model. A configuration that has extraordinarily good consistency, is to run CAM-FV with upwind (first-order) one-dimensional operators for the dynamics. This is extremely diffusive, effectively damping the baroclinic wave so much that the wave does not break until well after day 10, and then the nonlinearities are quickly dissipated out. This leads to a fundamentally different set of dynamics that are quasi-linear, allowing the tracer advection algorithm to perform very well. In this case the consistency of the model for any of the possbile tracer algorithms, is very good, but the scheme is highly inaccurate. From this example we can see the need to not only consider consistency, but also the accuracy of a model when evaluating its performance.

Another aspect to consider when evaluating the consistency of different dynamical cores is the characterization of their built-in dissipative mechanisms. The spatial discretization of CAM-EUL and CAM-SLD is prone to dispersive errors that are amplified through nonlinear dynamics. The dispersion is balanced in linear flow by an explicit hyper-diffusion term added to the momentum and thermodynamic equations, and in the case of CAM-SLD by the semi-Lagrangian time-stepping technique. Once the flow becomes nonlinear, smaller scale structures emerge in the sub-grid requiring a stronger, more localized dissipative method to remove dispersive waves. In CAM-SLD and CAM-EUL the dissipation is flow-independent in the sense that nonlinearities do not directly affect the magnitude of the dissipation. In contrast,

CAM-FV and CAM-SE both use monotonicity preserving limiters (in addition to explicit dissipative mechanisms like divergence damping for CAM-FV, and hyper-diffusion for CAM-SE) in the spatial discretization that are flow dependent, i.e. in regions of very steep gradients and the presence of small scale structures produced by nonlinearities the dissipation in CAM-SE and CAM-FV is strengthened. In light of the above argument that additional dissipation improves consistency, one can see why CAM-FV and CAM-SE have better consistency than CAM-EUL and CAM-SLD after the baroclinic wave breaks.

6.6 Conclusions

We have presented an explicit method for testing the consistency between the representation of dynamical variables and passive tracers in a dynamical core. By including tracer advection to the baroclinic wave test case of Jablonowski and Williamson (2006a), this Chapter proposes a test case that can be implemented easily. This provides ample opportunity to investigate the consistency of various models outside those implemented in NCAR's CESM framework, and we recommend other modeling groups to attempt the same comparison as performed here.

The results of this comparison among the four primary dynamical cores of CESM indicate that CAM-FV and CAM-SE are the most consistent while retaining reasonable accuracy. This is not unexpected as CAM-FV was built upon the premise that consistency was an important aspect of the algorithmic development (Rood, 2011; Lin and Rood, 1996, 1997). This does indicate that serious consideration of consistency issues must be included in the design and implementation of a dynamical core if consistency is a desired trait of the dynamical core.

This Chapter has primarily focused on the comparison between tracers and dy-

namics in a linear flow regime, when the dynamics are simpler, and well resolved. In reality climate models are meant to simulate nonlinear interactions on grids that cannot capture all of the scales present (either temporal or spatial). The predictions desired of climate models depends on the accurate representation of the effect of these small-scale nonlinear flows on the transport of various chemical and physical constituents that alter the greenhouse effect of the earth's atmosphere in addition to the accurate depiction of larger scale resolved flows. Hence it is important to accurately represent the consistency between the evolution of the winds, and the integration of passive tracers via those winds, otherwise the sub-grid effects that are not resolved will not be passed to the advection of the chemical constituents which will have significant effect on the climate dynamics.

An aspect of consistency even in the presence of strong nonlinearities deals with the difference between the nonlinear momentum equations, and the linear advection equation, as illustrated for two dimensions in Babiano and Provenzale (2007). For three dimensional, fully compressible (even hydrostatic) flow as utilized by most climate models, the passive tracer and dynamic variables are no longer guaranteed to agree once a discrete version of the equations is considered. When certain scales are truncated from the representation of the flow, the inter-scale interaction due to the nonlinear convective term in the momentum equation is not adquately captured, and so the discrete system will no longer maintain consistency, even in the ideal cases of extremely high resolution. Consideration of this nonlinear effect in the design and development of dynamical cores should be included in the future, as the climate is truly a nonlinear phenomenon involving interactions across scales.

The results of this Chapter are reported in Whitehead et al. (2011a).

CHAPTER VII

Conclusions and Discussion

To consider the effect of different boundary conditions on the turbulent transport of heat due to convection, we first considered an infinite Prandtl number fluid with an internal heat source, and isothermal vertical boundaries. For sticky side-walls (no-slip velocity boundary conditions) we used a framework developed in Doering et al. (2006) to bound the non-dimensional average temperature $\langle T \rangle$ from below by $\mathrm{R}^{-1/4}\log(\mathrm{R})^{1/4}$ where R is the heat Rayleigh number (see Sotin and Labrosse (1999)) proportional to the heating rate. This result is in agreement with a marginally stable boundary layer argument also presented in Chapter II. The logarithmic corrective factor is reminiscent of the result obtained in Doering et al. (2006) for boundary driven convective turbulence wherein bounds are sought on the Nusselt number, the non-dimensional measure of the enhancement of heat transport due to convection.

In Chapter III consideration of the internal heating driven convection problem is undertaken for finite Pr and in 2 dimensions. This particular problem has specific application to the convective motion that dominates the interior dynamics of stars (although in 3d in this case). Using an additional enstrophy constraint added to the traditional background method allows us to obtain the bound $\langle T \rangle \geq 0.7198\mathrm{R}^{-5/17}$ in this case. The same approach is adapted to traditional Rayleigh Bénard convection

where an imposed temperature gradient at the boundaries is the driving force (as opposed to an internal heat source). In agreement with a numerical investigation of the same problem (see Otero (2002)) performed a decade earlier, the Nusselt number is bounded above by $\mathrm{Ra}^{5/12}$ where Ra is now a measure of the strength of the imposed temperature gradient. This result is in direct opposition to a previously proposed theory (see Kraichnan (1962)) meant to understand the 'ultimate' regime of turbulent convection in which the scaling $\mathrm{Nu} \sim \mathrm{Ra}^{1/2}$ (modulo logarithmic corrections) was proposed. This result indicates the importance of considering the effect of boundaries on the turbulent transport of heat, and illustrates the effect that an under-resolved boundary may have on theoretical, experimental, and numerical considerations.

Finally, in Chapter IV we derive similar bounds as in Chapter III, but for 3 dimensional, infinite Prandtl number convection. The reason this is possible, is that the enstrophy balance is now implicitly maintained in the momentum equation where the velocity is slaved to the evolution of the temperature. The result for Rayleigh Bénard convection at infinite Prandtl number provides a rigorous argument for the conjecture given in Plasting and Ierley (2005); Ierley et al. (2006). These results in concert with those obtained in Chapter III indicate that the role of different velocity boundary conditions may have a significant impact on the transport of heat, even in three dimensional turbulence.

The final two Chapters address issues that arise at a modeling level when considering geophysical fluid dynamics. Chapter V provides a numerical linear stability analysis of an explicit dissipative mechanism incorporated in a specific type of climate model. The analysis is shown to be very sharp via some numerical examples, and the negative effects of a latitude-longitude grid on the sphere are illustrated including the inability of the damping to adequately remove certain spurious waves.

Chapter VI develops a test case that can be used to identify the consistency of an atmospheric model to maintain relationships between the dynamical wind components of the model, and any passive tracers. In the absence of frictional and diabatic forces, the potential vorticity (dot product of the gradient of potential temperature and vorticity) is conserved. This conservation property is utilized, as a tracer can be initialized analytically with the exact potential vorticity computable from analytic initial conditions for the dynamic variables. Integration of the model should then (ideally) conserve this relationship. Exploration of this in a simplified test problem indicate that the four dynamical cores of the National Center for Atmospheric Research's (NCAR) Community Atmosphere Model (CAM) do not adequately conserve this relationship. Quantification of this phenomenon via various metrics is proposed and the ability of any model to perform well in this area is questioned.

APPENDICES

APPENDIX A

Appendix A

A generalized Hardy-Rellich inequality

We will establish (2.32) for all functions $w(z)$ and $\theta(z)$ that satisfy (2.25) with the prescribed boundary conditions. Note that with the change of variables $z \to -z$ this is equivalent to casting the problem on the positive unit interval as

$$Re \int_0^1 \frac{\theta w^*}{z} dz \geq \frac{4}{\mathrm{R}} \int_0^1 \frac{|w|^2}{z^3} dz \tag{A.1}$$

where (2.25) is satisfied for $z \in [0,1]$ and $w(0) = w(1) = w'(0) = w'(1) = \theta(0) = \theta(1) = 0$. In this context, (A.1) is recognized as a factor of two improvement on the original proof Doering et al. (2006). As in the original proof we will prove the following proposition:

Proposition A.0.1. If $0 < c \leq d \leq \infty$, the smooth function $w(z)$ satisfies

$$w(c) = 0 = w(d),\ w'(c) = 0 = w'(d), \tag{A.2}$$

and $\theta(z)$ is defined by $w'''' - 2k^2 w'' + k^4 w = \mathrm{R} k^2 \theta$, then

$$Re \int_c^d \frac{\theta w^*}{z} dz \geq \frac{4}{\mathrm{R}} \int_c^d \frac{|w|^2}{z^3} dz. \tag{A.3}$$

In order to see the connection between (A.3) and Hardy-Rellich inequalities, make the change of variables $w(z) = z^{1/2}\zeta(z)$. It follows that $\zeta(z)$ also satisfies (A.2).

Inserting this change of variables into the fourth order term that results from the definition of $\theta(z)$, we see that

$$\int_c^d \frac{w''''w^*}{z}dz = \int_c^d |\zeta''|^2 dz - \frac{3}{2}\int_c^d \frac{|\zeta'|^2}{z^2}dz + \frac{45}{16}\int_c^d \frac{|\zeta|^2}{z^4}dz. \tag{A.4}$$

A similar calculation leads to

$$\int_c^d \frac{w''w^*}{z}dz = -\int_c^d |\zeta'|^2 dz + \frac{1}{4}\int_c^d \frac{|\zeta|^2}{z^2}dz. \tag{A.5}$$

Putting (A.4) and (A.5) together, we see that (A.3) can be restated as

Lemma A.1. *For smooth functions $\zeta(z)$ satisfying the boundary conditions* (A.2)*,*

$$\begin{aligned}\int_c^d \left(|\zeta''|^2 - \frac{3}{2}\frac{|\zeta'|^2}{z^2} + \frac{45}{16}\frac{|\zeta|^2}{z^4}\right)dz \quad &+ \quad k^2\int_c^d \left(2|\zeta'|^2 - \frac{1}{2}\frac{|\zeta|^2}{z^2}\right)dz + k^4\int_c^d |\zeta|^2 dz \geq \\ &\geq \quad 4k^2\int_c^d \frac{|\zeta|^2}{z^2}dz. \end{aligned} \tag{A.6}$$

Traditionally a Hardy-Rellich inequality is formulated in terms of the L^p norms of the operator $D^q = \frac{d^q}{dz^q}$ where $q = 1, 2$ and possibly higher orders (see Kufner and Persson (2003) for example). (A.6) is, with the appropriate integrations by parts, nothing else than the L^2 norm of the differential operator $D^2 - k^2$ acting on $\zeta(z)$. The inclusion of the wave number k here causes us to refer to this inequality as a generalized Hardy-Rellich inequality.

To prove the Lemma, consider the following one-parameter family of integrals,

$$0 \leq \int_c^d z^{2\nu}\left[\left(D^2 - k^2\right)\frac{\zeta}{z^\nu}\right]^2 dz, \tag{A.7}$$

where $\zeta(z)$ satisfies the homogeneous boundary conditions. Expanding (A.7) and integrating by parts multiple times leads to the following identity:

$$\begin{aligned}&\int_c^d |\zeta''|^2 dz + 2\nu(\nu-2)\int_c^d \frac{|\zeta'|^2}{z^2}dz \\ + \quad &2k^2\int_c^d |\zeta'|^2 dz + \nu(\nu + 6 + \nu^3 - 4\nu^2)\int_c^d \frac{|\zeta|^2}{z^4}dz \\ + \quad &k^4\int_c^d |\zeta|^2 dz \geq 2\nu^2 k^2 \int_c^d \frac{|\zeta|^2}{z^2}dz.\end{aligned}$$

Setting $\nu = \frac{3}{2}$ produces

$$\int_c^d |\zeta''|^2 dz - \frac{3}{2}\int_c^d \frac{|\zeta'|^2}{z^2} dz + \frac{45}{16}\int_c^d \frac{|\zeta|^2}{z^4} dz + 2k^2 \int_c^d |\zeta'|^2 dz$$
$$+ \quad k^4 \int_c^d |\zeta|^2 dz \geq \frac{9}{2} k^2 \int_c^d \frac{|\zeta|^2}{z^2} dz$$

which is easily rearranged to establish the Lemma.

The strictness of the inequality derived here can be verified by considering functions $\zeta(z)$ that saturate (A.7), that is those functions satisfying the boundary conditions together with

$$\left(D^2 - k^2\right) \frac{\zeta(z)}{z^\nu} = 0. \tag{A.8}$$

Solutions of (A.8) are linear combinations of modified Bessel functions:

$$\zeta(z) = z^{1/2+\nu} \left[C_1 K_q(kz) + C_2 I_q(kz)\right] \tag{A.9}$$

where $q = \sqrt{2\nu^2 + 2\nu + 1/4}$. Just as the original Hardy inequality (see Hardy (1920)) is not saturated for any nontrivial analytic functions, the functions (A.9) cannot satisfy all the boundary conditions simultaneously so there is no analytic solution to (A.8) that saturates (A.7). However, regularizing (A.9) appropriately at the boundaries will produce a sequence of functions that satisfy the boundary conditions and, in the unregularized limit, solve (A.8). Hence while (A.7) is never saturated, there can be no improvement on the prefactor derived by this method, i.e., the approach outlined here is not only robust and amenable to adaptation, but also produces sharp estimates.

This methodology lends itself immediately to extension to other operators, and possibly higher dimensions as well. The free parameter ν can be adjusted as desired, indicating a significant utility to this method of producing Hardy-Rellich type inequalities. Hardy-Rellich inequalities with remainder terms can also be computed

by optimizing over the wave-number k (for an example of other Hardy-Rellich type inequalities with remainder terms see the work of Evans and Lewis Evans and Lewis (2007)).

APPENDIX B

Appendix B

Incorporating the Polar Fourier Filter

We include the effect of the polar Fourier filter in the derivation of the amplification factors Γ_4 and Γ_2. The discretization provided in CAM 5 applies the filter only to the time tendencies of the winds, and not directly to the prognostic variables. For our analysis of the divergence equation this is equivalent to considering the update equation of the divergence (without any filtering) as

$$\frac{D_{i,j}^{n+1} - D_{i,j}^{n}}{\Delta t} = \beta_{i,j}^{n}$$

where β represents the 'tendency' of the divergence. For a von Neumann stability analysis, one considers the Fourier decomposition of the discrete equation, which for the tendency can be written as

$$\beta_{i,j}^{n} = \sum_{k_\lambda, k_\phi} \tilde{b}_{k_\lambda, k_\phi} e^{-\imath(k_\lambda \Delta\lambda + k_\phi \Delta\phi)}.$$

The stability of the scheme for a single wave number is then considered, i.e. for one $\tilde{b}_{k_\lambda, k_\phi}$.

The Fourier filter is applied directly to the tendency $\beta_{i,j}^{n}$, producing a filtered tendency $\hat{\beta}_{i,j}^{n}$ that is then used to update the divergence as

$$D_{i,j}^{n+1} = D_{i,j}^{n} + \Delta t \hat{\beta}_{i,j}^{n}.$$

To see how $\hat{\beta}^n_{i,j}$ is computed, we consider the purely zonal Fourier decomposition of the original tendency

$$\beta^n_{i,j} = \sum_{k_\lambda} \tilde{b}_{k_\lambda,j} e^{-\imath k_\lambda \Delta\lambda}$$

The filtered tendency is then given by

$$\hat{\beta}^n_{i,j} = \sum_{k_\lambda} d_{k_\lambda,j} \tilde{b}_{k_\lambda,j} e^{-\imath k_\lambda \Delta\lambda}$$

where

$$d_{k_\lambda,j} = \min\left\{1, \frac{\cos^2\phi_j}{\cos^2\phi_c} \frac{1}{\sin^2(k_\lambda \Delta\lambda/2)}\right\} \tag{B.1}$$

denotes the formulation of the Fourier damping coefficients following Fox-Rabinovitz et al. (1997) (their Eq. 9). ϕ_c is the critical latitude where the Fourier filter begins to take effect, which is dependent on the aspect ratio $\alpha = \Delta\lambda/\Delta\phi$ of the grid. In particular, CAM-FV uses the condition

$$\phi_c = \arccos\Big[\min\big(0.81, \Delta\phi/\Delta\lambda\big)\Big]. \tag{B.2}$$

For $\alpha = 1$ as generally considered in our dynamical core simulations, the critical latitude is $\phi_c \sim 36°$, whereas for the CAM-FV default aspect ratio $\alpha \sim 1.33$ the threshold lies around $\phi_c \sim 41°$. The damping is not applied to the zero mode (which represents purely meridional motion) or the largest represented wave (smallest wave number). This restricts the filter from directly affecting purely meridional motion.

To incorporate the effect of this filter into the stability analysis, we only need to consider the meridionally Fourier-transformed term $d_{k_\lambda,j}\tilde{b}_{k_\lambda,j}$. Invoking the assumption that $\cos\phi$ does not change at the grid level, we can view $d_{k_\lambda,j}$ as constant. Using the linearity of the Fourier transform, we see that the filtered tendencies of a single wave-number are given by

$$d_{k_\lambda,j}\tilde{b}_{k_\lambda,k_\phi}. \tag{B.3}$$

Hence, when including the effect of the Fourier filter into the stability analysis, we only need to multiply the tendency terms by $d_{k_\lambda,j}$. To see how this affects the stability, consider latitudes poleward of the critical latitude ϕ_c and wave numbers that involve some zonal component (not the zeroth mode, or the largest represented zonal wave). This implies

$$\Gamma_2 = 1 - 4\,C_2\,\frac{\cos^r\phi}{\cos^2\phi_c}\,\left\{\alpha\cos^2\phi\,\frac{\sin^2\left(k_\phi\Delta\phi/2\right)}{\sin^2\left(k_\lambda\Delta\lambda/2\right)} + \frac{1}{\alpha}\right\} \tag{B.4}$$

$$\Gamma_4 = 1 - 16\,C_4\,\frac{\cos^r\phi}{\cos^2\phi_c}\,\left\{\alpha\cos\phi\,\frac{\sin^2\left(k_\phi\Delta\phi/2\right)}{\sin\left(k_\lambda\Delta\lambda/2\right)} + \frac{1}{\alpha\cos\phi}\sin\left(\frac{k_\lambda\Delta\lambda}{2}\right)\right\}^2. \tag{B.5}$$

These equations show that the Fourier filter removes any instability present in the second-order divergence damping so long as $r \geq 0$. However, even with application of the polar filter to the fourth order divergence damping, the purely zonal wave-numbers have an amplification factor that scales as $\cos^{r-2}\phi$ which can be controlled near the poles only for $r \geq 2$ which corresponds to the default value chosen for CAM5.0.

APPENDIX C

Appendix C

Analytic calculation of initial PV

Details of the initial conditions for the baroclinic wave test case are given in Jablonowski and Williamson (2006a). Here we will review only partially those details necessary to compute the potential vorticity. Note that although the tests considered in this work are on a latitude-longitude grid, the formulation provided here can be used to initialize the PV tracer on any choice of grid. The definition of Ertel's potential vorticity on pressure levels is

$$q = g\left\{\frac{1}{a\cos\phi}\frac{\partial v}{\partial p}\left(\frac{\partial\theta}{\partial\lambda}\right)_p - \frac{1}{a}\frac{\partial u}{\partial p}\left(\frac{\partial\theta}{\partial\phi}\right)_p + (f+\zeta_p)\left(-\frac{\partial\theta}{\partial p}\right)\right\} \tag{C.1}$$

where g is the gravitational constant, $f = 2\Omega\sin\phi$ the Coriolis parameter, a the radius of the earth, u and v the zonal and meridional components of the horizontal velocity respectively, θ the potential temperature, ζ_p the horizontal vorticity computed at constant pressure, and λ, ϕ represent the longitudinal and latitudinal location respectively. The subscript p denotes that these derivatives are taken at constant pressure levels. We consider the analytic initial conditions described in Jablonowski and Williamson (2006a).

The total velocity components for the test case are given by

$$u(\lambda,\phi,\eta) = u_0 \cos^{3/2}\eta_v \sin^2(2\phi) + u_p \exp\left(-\left(\frac{r}{R}\right)^2\right) \tag{C.2}$$

$$v(\lambda,\phi,\eta) = 0 \tag{C.3}$$

where

$$r = a \arccos\left(\sin\phi_c \sin\phi + \cos\phi_c \cos\phi \cos(\lambda - \lambda_c)\right) \tag{C.4}$$

and $R = a/10$ ($a = 6.371229\times10^6$ m being the radius of the earth), $u_p = 1\ ms^{-1},\ u_0 = 35\ ms^{-1},\ \lambda_c = \pi/9,\ \phi_c = 2\pi/9,\ \eta_v = (\eta - \eta_0)\frac{\pi}{2}$ and $\eta_0 = 0.252$ are all constants, and $\eta = \frac{p}{p_0}$ is the normalized vertical pressure coordinate for the initial data.

This immediately leads to the relative vorticity in the outward direction (perpendicular to the pressure surfaces in this case) being given by:

$$\zeta(\lambda,\phi,\eta) = -4\frac{u_0}{a}\cos^{3/2}\eta_v \sin\phi\cos\phi(2 - 5\sin^2\phi) + \frac{u_p}{a}\exp\left(-\left(\frac{a}{R}\right)^2\right) \tag{C.5}$$

$$\times\left\{\tan\phi - 2\left(\frac{r}{R}\right)^2 \arccos(X)\frac{\sin\phi_c\cos\phi - \cos\phi_c\sin\phi\cos(\lambda-\lambda_c)}{\sqrt{1-X^2}}\right\} \tag{C.6}$$

where $X = \sin\phi_c\sin\phi + \cos\phi_c\cos\phi\cos(\lambda - \lambda_c)$. All of this leads to

$$\frac{\partial u}{\partial \eta} = -u_0 \sin^2(2\phi)\frac{3}{2}\frac{\pi}{2}\cos^{1/2}\eta_v \sin\eta_v \tag{C.7}$$

where we use the identity

The temperature is given by

$$T(\lambda,\phi,\eta) = \overline{T}(\eta) + \frac{3}{4}\frac{\eta\pi u_0}{R_d}\sin\eta_v \cos^{1/2}\eta_v \tag{C.8}$$

(C.9)

$$\times\left\{\left(-2\sin^6\phi\left[\cos^2\phi + \frac{1}{3}\right] + \frac{10}{63}\right)2u_0\cos^{3/2}\eta_v + \left(\frac{8}{5}\cos^3\phi\left[\sin^2\phi + \frac{2}{3}\right] - \frac{\pi}{4}\right)a\Omega\right\}$$

where $\Omega = 7.29212 \times 10^{-5} s^{-1}$ is the Earth's angular velocity, and the mean temperature (model level dependent) profile is described by

$$\overline{T}(\eta) = T_0 \eta^{R_d \Gamma / g} \text{ for } \eta_s \geq \eta \geq \eta_t \tag{C.10}$$

$$\overline{T}(\eta) = T_0 \eta^{R_d \Gamma / g} + \Delta T (\eta_t - \eta)^5 \text{ for } \eta_t > \eta \tag{C.11}$$

where $\eta_s = 1,\ \eta_t = 0.2,\ T_0 = 288\ K,\ \Gamma = 0.005\ Km^{-1},\ \Delta T = 4.8 \times 10^5\ K,\ R_d = 287.04\ J(kgK)^{-1},\ g = 9.80616\ ms^{-2}$ are all constants.

This leads to the initial distribution of potential temperature

$$\theta(\lambda, \phi, \eta) = \overline{T}(\eta) \eta^{-R_d/c_p} + \frac{3}{4} \frac{\pi u_0}{R_d} \eta^{1 - R_d/c_p} \sin \eta_v \cos^{1/2} \eta_v$$
$$\times \left\{ \left(-2 \sin^6 \phi \left[\cos^2 \phi + \frac{1}{3} \right] + \frac{10}{63} \right) 2 u_0 \cos^{3/2} \eta_v + \left(\frac{8}{5} \cos^3 \phi \left[\sin^2 \phi + \frac{2}{3} \right] - \frac{\pi}{4} \right) a \Omega \right\}$$

with vertical derivative calculated as:

$$\frac{\partial \theta}{\partial \eta} = \frac{\partial \overline{\theta}}{\partial \eta} + \frac{3}{4} \frac{\pi u_0}{R_d} \left(1 - \frac{R_d}{c_p} \right) \eta^{-R_d/c_p} \sin \eta_v \cos^{1/2} \eta_v Y + \frac{3}{8} \frac{\pi^2 u_0}{R_d} \eta^{1 - R_d/c_p} \cos^{3/2} \eta_v Y$$
$$- \frac{3}{16} \frac{\pi^2 u_0}{R_d} \eta^{1 - R_d/c_p} \sin^2 \eta_v \cos^{-1/2} \eta_v Y$$
$$- \frac{9}{8} \frac{\pi^2 u_0^2}{R_d} \eta^{1 - R_d/c_p} \sin^2 \eta_v \cos \eta_v \left(-2 \sin^6 \phi \left[\cos^2 \phi + \frac{1}{3} \right] + \frac{10}{63} \right)$$

where

$$Y = \left(-2 \sin^6 \phi \left[\cos^2 \phi + \frac{1}{3} \right] + \frac{10}{63} \right) 2 u_0 \cos^{3/2} \eta_v + \left(\frac{8}{5} \cos^3 \phi \left[\sin^2 \phi + \frac{2}{3} \right] - \frac{\pi}{4} \right) a \Omega \tag{C.12}$$

and

$$\frac{\partial \overline{\theta}}{\partial \eta} = \begin{cases} T_0 R_d \left(\frac{\Gamma}{g} - \frac{1}{c_p} \right) \eta^{R_d(\Gamma/g - 1/c_p) - 1} & \text{for } \eta_s \geq \eta \geq \eta_t \\ T_0 R_d \left(\frac{\Gamma}{g} - \frac{1}{c_p} \right) \eta^{R_d(\Gamma/g - 1/c_p) - 1} & \\ \quad - \Delta T \left(5(\eta_t - \eta)^4 \eta^{-R_d/c_p} + \frac{R_d}{c_p} (\eta_t - \eta)^5 \eta^{-R_d/c_p - 1} \right) & \text{for } \eta_t > \eta \end{cases}.$$

The derivative of potential temperature with respect to the latitudinal direction is also given by

$$\frac{\partial\theta}{\partial\phi} = \frac{3}{4}\frac{\pi u_0}{aR_d}\eta^{1-R_d/c_p}\sin\eta_v\cos^{1/2}\eta_v$$
$$\times\left\{2u_0\cos^{3/2}\eta_v\left(-12\cos\phi\sin^5\phi\left[\cos^2\phi+\frac{1}{3}\right]+4\cos\phi\sin^7\phi\right)\right.$$
$$\left.+\,a\Omega\left(-\frac{24}{5}\sin\phi\cos^2\phi\left[\sin^2\phi+\frac{2}{3}\right]+\frac{16}{5}\cos^4\phi\sin\phi\right)\right\}.$$

Combining all of these terms as illustrated in (C.1) we can define the initial PV distribution exactly. The PV is positive in the northern hemisphere, and negative in the southern hemisphere. To avoid model errors arising from negative tracer constituents, the tracer PV is initialized as the absolute value of the computed PV.

APPENDIX D

Appendix D

Calculation of PV from dynamic variables

In the CAM-FV and CAM-EUL dynamical cores the vertical discretization follows a hybrid vertical coordinate (see Neale et al. (2010)). In order to avoid the cascade of interpolation errors, the potential vorticity is first computed on these hybrid model levels, and then interpolated to pressure levels (typically 850 hPa). This allows us to distinguish between the errors caused by the computation of the potential vorticity, and the error due to the interpolation to pressure levels. This appendix describes the computation of the potential vorticity on the hybrid model levels, and in particular describes the method of computing the vertical derivative of the potential temperature. The latter can be an extreme source of error in part due to the limited number of vertical levels typically used for climate runs. Justification for this approach is also provided, and the inherent errors due to the different discrete portions of the calculation are addressed.

The typical definition of Ertel's potential vorticity on pressure levels is given by (C.1). In CAM the model levels are pressure dependent, so to compute q on model

level $k = k(p)$ we make the adjustment

$$q = g \left\{ \frac{1}{a \cos\phi} \frac{\partial v}{\partial k} \frac{\partial k}{\partial p} \left(\frac{\partial \theta}{\partial \lambda} \right)_k - \frac{1}{a} \frac{\partial u}{\partial k} \frac{\partial k}{\partial p} \left(\frac{\partial \theta}{\partial \phi} \right)_k \right. \tag{D.1}$$

$$\left. + (f + \zeta_k) \left(-\frac{\partial \theta}{\partial k} \right) \frac{\partial k}{\partial p} \right\} \tag{D.2}$$

where

$$\frac{\partial k}{\partial p} = \frac{1}{\frac{\partial A(k)}{\partial k} p_0 + \frac{\partial B(k)}{\partial k} p_s(\lambda, \phi)}, \tag{D.3}$$

$p_s(\lambda, \phi)$ being the surface pressure, p_0 a reference pressure (typically $p_0 = 1000$ hPa) and $\frac{\partial A(k)}{\partial k}$ and $\frac{\partial B(k)}{\partial k}$ are computed by using $A(k)$ and $B(k)$ at the intermediate, interface model levels. (D.3) is computed using the definition of pressure from the hybrid model levels (see Neale et al. (2010) for details):

$$p = A(k) p_0 + B(k) p_s(\lambda, \phi). \tag{D.4}$$

Using (D.3) leads to the following definition of the potential vorticity

$$q = \frac{g \left\{ \frac{1}{a \cos\phi} \frac{\partial v}{\partial k} \left(\frac{\partial \theta}{\partial \lambda} \right)_k - \frac{1}{a} \frac{\partial u}{\partial k} \left(\frac{\partial \theta}{\partial \phi} \right)_k - (f + \zeta_k) \frac{\partial \theta}{\partial k} \right\}}{\frac{\partial A(k)}{\partial k} p_0 + \frac{\partial B(k)}{\partial k} p_s(\lambda, \phi)}. \tag{D.5}$$

The difficulty in calculating (D.5) in a discrete setting is primarily due to the final term which involves the vertical derivative of the potential temperature θ. This is issue is well known, and is the primary reason that PV has not been utilized more frequently in the analysis of model output (see Brunet et al. (1995)). This is due in part to the low vertical resolution used in default CAM configurations, and because the potential temperature has a mean exponential vertical profile which is very difficult to discretize. With this in mind, discretization of this term is treated with extreme care.

This leads to another caution when comparing computations of PV. Due to the exponential nature of the potential temperature profile, and the restricting boundaries at the model top and surface, care should be taken near these boundaries. For

this reason all of the data discussed in these results are linearly interpolated (in pressure coordinates) to 850 hPa. This is far enough from the surface to avoid errors due to the bottom boundary, yet far enough from the model top that extreme errors due to the vertical derivative will not adversely affect the results. The interpolation to a pressure level was made so that intercomparison with models using different vertical coordinates might be enabled.

It was found that reconstructing $\theta(k)$ with a natural cubic spline (see Bartels et al. (1998)), and then differentiating the resultant spline led to the most accurate results. This can be verified directly by applying this method to the initial data and comparing directly with the analytic formula produced in Appendix C. The cubic spline is also preferable because it immediately lends itself to a sparse tri-diagonal solver that can be implemented with limited overhead in the post-processing.

Table D.1 shows the l^4 error norms (difference from the analytic prescription derived in Appendix C) at 850 hPa (see Section 6.4 for a discussion of this choice of error norm) of the cubic spline based computation of the initial PV for several vertical resolutions with a fixed horizontal resolution of $2^\circ \times 2^\circ$. Also shown is the error when a simple centered finite difference method is used to calculate $\frac{\partial \theta}{\partial k}$. Note the significant increase in accuracy due to the change to the cubic spline algorithm. The decrease from 52 to 104 vertical levels is likely due to the exact placing of each level (52 levels happens to have one model level very close to 850 hPa). We note that although the cubic spline is formally third-order, and centered finite differencing is second-order, the cubic spline appears to perform much better. Speculation for this significant increase in accuracy despite only a single formal order of accuracy improvement may lend insight into the nature of the potential temperature profile or may only be a by-product of this test case. Another important feature this highlights

is the lack of error in the horizontal discretization, since the vertically 'converged' solution with 208 levels has errors less than 0.02 percent at such a coarse horizontal resolution.

Table D.1: Percentage of the normalized l_4 error norms at 850 hPa for the computation of initial PV.

Number of vertical model levels	26	52	104	208
cubic spline	0.1722096	0.0226977	0.023411	0.019693
centered finite difference	3.2168	0.69699	0.145722	0.021527

BIBLIOGRAPHY

BIBLIOGRAPHY

Ahlers, G., 2009: Turbulent Convection. *Physics*, **2 (74)**, 7 pp.

Ahlers, G., S. Grossmann, and D. Lohse, 2009: Heat transfer and large scale dynamics in turbulent Rayleigh-Bénard convection. *Review of Modern Physics*, **81**, 503–537.

Anderson, J., T. Hoar, K. Raeder, H. Liu, N. Collins, R. Torn, and A. Avellano, 2009: The data assimilation research testbed: a community facility. *Bulletin of the American Meteorological Society*, **90 (9)**, 1283–1296.

Andrews, D. G. and M. E. McIntyre, 1978: An exact theory of nonlinear waves on a Lagrangian-mean flow. *Journal of Fluid Mechanics*, **89 (4)**, 609–646.

Arakawa, A. and V. R. Lamb, 1977: Computational design of the basic dynamical process of the UCLA general circulation model. *Methods in Computational Physics*, J. Chang, Ed., Academic Press, 173–265.

Babiano, A. and A. Provenzale, 2007: Coherent vortices and tracer cascades in two-dimensional turbulence. *Journal of Fluid Mechanics*, **574**, 429–448.

Bala, G., R. Rood, D. Bader, A. Mirin, D. Ivanova, and C. Drui, 2008: Simulated climate near steep topography: Sensitivity to numerical methods for atmospheric transport. *Geophysical Research Letters*, **35**, 5 pp.

Bartels, R. H., J. C. Beatty, and B. A. Barsky, 1998: Hermite and cubic spline interpolation. *Introduction to Splines for Use in Computer Graphics and Geometric Modeling*, Morgan Kaufmann, chap. 3, 9–17.

Bates, J. R., S. Moorthi, and R. W. Higgins, 1993: A global multilevel atmospheric model using a vector semi-Lagrangian finite difference scheme. Part I: Adiabatic formulation. *Monthly Weather Review*, **121**, 244–263.

Boville, B. A., 1991: Sensitivity of simulated climate to model resolution. *Journal of Climate*, **4**, 469–485.

Brunet, G., R. Vautard, B. Legras, and S. Edouard, 1995: Potential vorticity on isentropic surfaces: Climatology and diagnostics. *Monthly Weather Review*, **123**, 1037–1058.

Busse, F. H., 1969: On Howard's upper bound for heat transport by turbulent convection. *Journal of Fluid Mechanics*, **37**, 457–477.

Calzavarini, E., C. R. Doering, J. D. Gibbon, D. Lohse, A. Tanabe, and F. Toschi, 2006: Exponentially growing solutions in homogeneous Rayleigh-Bénard convection. *Physical Review E*, **73**, 035 301(R) (4pp).

Charney, J. G., 1948: On the scale of atmospheric motions. *Geophysical Publications*, **17 (2)**, 17 pages.

Charney, J. G., 1949: On a physical basis for numerical prediction of large-scale motions in the atmosphere. *Journal of Meteorology*, **6 (6)**, 371–385.

Charney, J. G., R. Fjortoft, and J. von Neumann, 1950: Numerical Integration of the Barotropic Vorticity Equation. *Tellus*, **2**, 237–254.

Cloutier, B., B. K. Muite, and J. P. Whitehead, 2011: Convection driven by internal heating.

Colella, P. and P. R. Woodward, 1984: The Piecewise Parabolic Method (PPM) for gas-dynamical simulations. *Journal of Computational Physics*, **54**, 174–201.

Collins, W. D., et al., 2004: Description of the NCAR Community Atmosphere Model (CAM3.0). NCAR Tech. Note NCAR/TN-464+STR, National Center for Atmospheric Research, Boulder, Colorado. 226 pp.

Courant, R., K. O. Friedrichs, and H. Lewy, 1928: Über die partiellen Differenzengleichungen der mathematischen Physik. *Mathematische Annalen*, **100 (1)**, 32–74.

DeLuca, E. E., J. Werne, R. Rosner, and F. Cattaneo, 1990: Numerical simulations of soft and hard turbulence: Preliminary results for two-dimensional convection. *Physical Review Letters*, **64**, 23702373.

Delworth, T., et al., 2006: GFDL's CM2 global coupled climate models. Part I: Formulation and simulation characteristics. *Journal of Climate*, **19 (5)**, 643–674.

Dey, C., 1978: Noise suppression in a primitive equation prediction model. *Monthly Weather Review*, **106**, 159–173.

Doering, C. R. and P. Constantin, 1992: Energy dissipation in shear driven turbulence. *Physical Review Letters*, **69 (11)**, 1648–1651.

Doering, C. R. and P. Constantin, 1994: Variational bounds on energy dissipation in incompressible flows: Shear flow. *Physical Review E.*, **49**, 4087–4099.

Doering, C. R. and P. Constantin, 1996: Variational bounds on energy dissipation in incompressible flows. III. Convection. *Physical Review E.*, **53 (6)**, 5957–5981.

Doering, C. R. and P. Constantin, 2001: On upper bounds for infinte Prandtl number convection with or without rotation. *Journal of Mathematical Physics*, **45 (2)**, 784–795.

Doering, C. R. and J. D. Gibbon, 1995: *Applied Analysis of the Navier-Stokes Equations.* Cambridge University Press.

Doering, C. R., F. Otto, and M. G. Reznikoff, 2006: Bounds on vertical heat transport for infinite-Prandtl-number Rayleigh-Bénard convection. *Journal of Fluid Mechanics*, **560**, 229–241.

Durran, D. R., 1999: *Numerical Methods for Wave Equations in Geophysical Fluid Dynamics.* Springer, ISBN 0-387-98376-7, 465 pp.

Emmanuel, K., 1994: *Atmospheric Convection.* Oxford University Press.

Ertel, H., 1942: Ein Neuer hydrodynamischer Wirbelsatz. *Meteorologische Zeitschrift*, **59**, 271–281.

Evans, W. D. and R. T. Lewis, 2007: Hardy and Rellich inequalities with remainders. *Journal of Mathematical Inequalities*, **1 (4)**, 473–490.

Fefferman, C. L., 2002: Existence and smoothness of the Navier-Stokes equation. $www.claymath.org/milleninium/Navier - Stokes_Equations/$, 6 pp.

Fox-Rabinovitz, M. S., G. L. Stenchikov, M. J. Suarez, and L. L. Takacs, 1997: A finite-difference GCM dynamical core with a variable-resolution stretched grid. *Monthly Weather Review*, **125**, 2943–2968.

Garaud, P., G. I. Ogilvie, N. Mille, and S. Stellmach, 2010: A model of the entropy flux and Reynolds stress in turbulent convection. *Monthly Notices of the Royal Astronomical Society*, **407**, 2451–2467.

Gassman, A. and H. J. Herzog, 2008: Towards a consistent numerical compressible non-hydrostatic model using generalized Hamiltonian tools. *Quarterly Journal of the Royal Meteorological Society*, **134 (635)**, 1597–1613.

Gibbon, J. D. and D. D. Holm, 2010: Stretching & folding diagnostics in solutions of the three-dimensional Euler & Navier-Stokes equations. *arXiv*, **(1012.359v1)**.

Goluskin, D., 2011: personal communication.

Grossman, S. and D. Lohse, 2000: Scaling in thermal convection: a unifying theory. *Journal of Fluid Mechanics*, **407**, 27–56.

Haltiner, G. J. and R. T. Williams, 1980: *Numerical Prediction and Dynamic Meteorology*. John Wiley & Sons, ISBN 0-471-05971-4, 477 pp.

Hardy, G. H., 1920: Note on a theorem of Hilbert. *Mathematische Zeitschrift*, **6 (3)**, 314–317.

Haynes, P. H. and M. E. McIntyre, 1987: On the evolution of vorticity and potential vorticity in the presence of diabatic heating and frictional or other forces. *Journal of Atmospheric Science*, **44 (5)**, 828–841.

Holton, J. R., 2004: *An Introduction to Dynamic Meteorology*. 4th ed., Elsevier Academic Press, ISBN-13 978-0-12-354015-7, 535 pp.

Hopf, E., 1940: Ein allgemeiner Endlichkeitssatz der Hydrodynamik. *Mathematische Annalen*, **117**, 764–775.

Hoskins, B. J., M. E. McIntyre, and A. W. Robertson, 1985: On the use and significance of isentropic potential vorticity maps. *Quarterly Journal of the Royal Meteorological Society*, **111**, 877–946.

Howard, L. N., 1963: Heat transport by turbulent convection. *Journal of Fluid Mechanics*, **17**, 405–432.

Ierley, G. R., R. R. Kerswell, and S. C. Plasting, 2006: Infinite-Prandtl-number convection. Part 2. A singular limit of upper bound theory. *Journal of Fluid Mechanics*, **560**, 159–227.

Ierley, G. R. and R. A. Worthing, 2001: Bound to improve: a variational approach to convective heat transport. *Journal of Fluid Mechanics*, **441**, 223–253.

Jablonowski, C., P. H. Lauritzen, R. D. Nair, and M. A. Taylor, 2008a: Idealized test cases for the dynamical cores of Atmospheric General Circulation Models: A proposal for the NCAR ASP 2008 summer colloquium. Tech. rep., NCAR, 77 pp.

Jablonowski, C., P. H. Lauritzen, M. A. Taylor, and R. D. Nair, 2008b: An intercomparison of 10 atmospheric model dynamical cores. *Eos Transactions American Geophysical Union*, **89 (53)**, Abstract A33A–0214, Fall Meet. Suppl.

Jablonowski, C. and D. L. Williamson, 2006a: A baroclinic instability test case for atmospheric model dynamical cores. *Quarterly Journal of the Royal Meteorological Society*, **132 (621)**, 2943–2975.

Jablonowski, C. and D. L. Williamson, 2006b: A baroclinic wave test case for dynamical cores of General Circulation Models: Model intercomparisons. NCAR Tech. Note NCAR/TN-469+STR, National Center for Atmospheric Research, Boulder, Colorado. 89 pp.

Jablonowski, C. and D. L. Williamson, 2011: The pros and cons of diffusion, filters, and fixers in atmospheric general circulation models. *Numerical Techniques for Global Atmospheric Models*, P. H. Lauritzen, C. Jablonowski, M. A. Taylor, and R. D. Nair, Eds., Springer, Lecture Notes in Science and Engineering, Vol. 80, 389–504.

Joeckel, P., R. von Kuhlmann, M. G. Lawrence, B. Steil, C. A. M. Brenninkmeijer, P. J. Crutzen, P. J. Rasch, and B. Eaton, 2001: On a fundamental problem in implementing flux-form advection schemes for tracer transport in 3-dimensional general circulation and chemistry transport models. *Quarterly Journal of the Royal Meteorological Society*, **127**, 1035–1052.

Johnston, H. and C. R. Doering, 2009: Comparison of turbulent thermal convection between conditions of constant temperature and constant flux. *Physical Review Letters*, **102**, 064 501, p1–p4.

Julien, K., S. Legg, J. McWilliams, and J. Werne, 1995: Hard turbulence in rotating Rayleigh-Bénard convection. *Physical Review E*, **53 (6)**, R5557–R5560.

Kent, J., C. Jablonowski, J. P. Whitehead, and R. B. Rood, 2011: Assessing tracer transport algorithms and the impact of vertical resolution in a finite-volume dynamical core (in press). *Monthly Weather Review*.

Konor, C. S. and A. Arakawa, 1997: Design of an atmospheric model based on a generalized vertical coordinate. *Monthly Weather Review*, **125 (7)**, 1649–1673.

Kraichnan, R. H., 1962: Turbulent thermal convection at arbitrary Prandtl number. *Physics of Fluids*, **5**, 1374–1389.

Kufner, A. and L.-E. Persson, 2003: *Weighted inequalities of Hardy type*. World Scientific Publishing Co. Pte. Ltd.

Lamarque, J. E., D. E. Kinnison, P. G. Hess, and F. M. Vitt, 2008: Simulated lower stratospheric trends between 1970 and 2005: Identifying the role of climate and composition changes. *Journal of Geophyiscal Research*, **113**, 1–19.

Lander, J. and B. J. Hoskins, 1997: Believable scales and parameterizations in a spectral transform model. *Monthly Weather Review*, **125**, 292–303.

Lauritzen, P. H., 2007: A stability analysis of finite-volume advection schemes permitting long time steps. *Monthly Weather Review*, **135 (7)**, 2658–2673.

Lauritzen, P. H., A. A. Mirin, J. Truesdale, K. Raeder, J. L. Anderson, J. Bacmeister, and R. B. Neale, 2011a: Implementation of new diffusion/filtering operators in the CAM-FV dynamical core. *International Journal of High Performance Computing Applications*, dOI::10.1177/1094342011410088.

Lauritzen, P. H., P. A. Ullrich, and R. D. Nair, 2011b: Atmospheric transport schemes: Desirable properties and a semi-Lagrangian view on finite-volume discretizations. *Numerical Techniques for Global Atmospheric Models*, P. H. Lauritzen, C. Jablonowski, M. A. Taylor, and R. D. Nair, Eds., Springer, Lecture Notes in Science and Engineering, Vol. 80, 187–248.

Lee, S. M., S. C. Yoon, and D. W. Byun, 2004: The effect of mass inconsistency of the meteorological field generated by a common meteorological model on air quality modeling. *Atmospheric Environment.*, **38 (18)**, 2917–2926.

Lin, S.-J., 2004: A "vertically Lagrangian" finite-volume dynamical core for global models. *Monthly Weather Review*, **132**, 2293–2307.

Lin, S.-J. and R. B. Rood, 1996: Multidimensional flux-form semi-Lagrangian transport scheme. *Monthly Weather Review*, **124**, 2046–2070.

Lin, S.-J. and R. B. Rood, 1997: An explicit flux-form semi-Lagrangian shallow water model on the sphere. *Quarterly Journal of the Royal Meteorological Society*, **123**, 2477–2498.

Lindborg, E., 1999: Can the atmospheric kinetic energy spectrum be explained by two-dimensional turbulence? *Journal of Fluid Mechanics*, **388**, 259–288.

Lohse, D. and F. Toschi, 2003: Ultimate state of thermal convection. *Physical Review Letters*, **90**, 034 502 (3pp).

Lorenz, E. N., 1963: Deterministic nonperiodic flow. *Journal of Atmospheric Science*, **20**, 130–141.

Lu, L., C. R. Doering, and F. H. Busse, 2004: Bounds on convection driven by internal heating. *Journal of Mathematical Physics*, **45 (7)**, 2967–2986.

Lynch, P., 2008: The origins of computer weather prediction and climate modeling. *Journal of Computational Physics*, **227 (7)**, 3431–3444.

Malkus, W. V. R., 1954: The heat transport and spectrum of thermal turbulence. *Proceedings of the Royal Society of London A*, **225**, 196–212.

Malkus, W. V. R. and G. Veronis, 1958: Finite amplitude cellular convection. *Journal of Fluid Mechanics*, **4**, 225–260.

McIntyre, M. E. and T. N. Palmer, 1983: Breaking planetary waves in the stratosphere. *Nature*, **305**, 593–600.

Moeller, J. D. and M. T. Montgomery, 2000: Tropical cyclone evolution via potential vorticity anomalies in a three-dimensional balance model. *Journal of Atmospheric Science*, **57**, 3366–3387.

Nair, R. D. and P. H. Lauritzen, 2010: A class of deformational flow test-cases for the advection problems on the sphere. *Journal of Computational Physics*, **229**, 8868–8887.

Nair, R. D., M. N. Levy, and P. H. Lauritzen, 2011: Emerging Numerical Methods for Atmospheric Modeling. *Numerical Techniques for Global Atmospheric Models*, P. H. Lauritzen, C. Jablonowski, M. A. Taylor, and R. D. Nair, Eds., Springer, Lecture Notes in Science and Engineering, Vol. 80, 251–311.

Nastrom, G. D. and K. S. Gage, 1985: A climatology of atmospheric wavenumber spectra of wind and temperature observed by commercial aircraft. *Journal of Atmospheric Science*, **42**, 950 960.

Neale, R. B., et al., 2010: Description of the NCAR Community Atmosphere Model (CAM 5.0). NCAR Technical Note NCAR/TN-486+STR, National Center for Atmospheric Research, Boulder, Colorado.

Newell, A. C. and J. A. Whitehead, 1969: Finite bandwidth, finite amplitude convection. *Journal of Fluid Mechanics*, **38**, 279–303.

Nicodemus, R., S. Grossmann, and M. Holthaus, 1997: Improved variational principle for bounds on energy dissipation in turbulent shear flow. *Physica D.*, **101**, 178–190.

Ohkitani, K., 1991: Wave number space dynamics of enstrophy cascade in a forced 2-dimensional turbulence. *Physics of Fluids A*, **3**, 1598–1611.

Otero, J., 2002: Bounds for the heat transport in turbulent convection. Ph.D. thesis, University of Michigan, MI, Department of Mathematics, 137 pp.

Otero, J., R. W. Wittenberg, R. A. Worthing, and C. R. Doering, 2002: Bounds on Rayleigh-Bénard convection with an imposed heat flux. *Journal of Fluid Mechanics*, **473**, 191–199.

Ottino, J., 1989: *The Kinematics of Mixing: Stretching, Chaos, and Transport*. Cambridge University Press.

Pedlosky, J., 1987: *Geophysical Fluid Dynamics*. Springer-Verlag.

Plasting, S. C. and G. R. Ierley, 2005: Estimates of heat transport in infinite Prandtl number convection. Part 1. Conservative bounds. *Journal of Fluid Mechanics*, **542**, 343–363.

Plasting, S. C. and R. R. Kerswell, 2003: Improved upper bound on the energy dissipation rate in Plane Couette flow: the full solutions to Busse's problem and the Constantin-Doering-Hopf problem with one-dimensional background fields. *Journal of Fluid Mechanics*, **477**, 363–379.

Putman, W. M. and S.-J. Lin, 2009: A finite-volume dynamical core on the cubed-sphere grid. *Numerical Modeling of Space Plasma Flows: Astronum-2008*, Astronomical Society of the Pacific Conference Series, Vol. 406, 268–276.

Rasch, P. J., D. B. Coleman, N. Mahowald, D. L. Williamson, S.-J. Lin, B. A. Boville, and P. Hess, 2006: Characteristics of atmospheric transport using three numerical formulations for atmospheric dynamics in a single GCM framework. *Journal of Climate*, **19**, 2243–2266.

Rayleigh, L., 1916: On convection currents in a horizontal layer of fluid, when the higher temperature is on the under side. *Philosophical Magazine and Journal of Science*, **32 (192)**, 529–546.

Richardson, L. F., 1922: *Weather Prediction by Numerical Process*. Cambridge University Press, 250 pp., reprinted NY, Dover 1965.

Rienecker, M. M., et al., 2008: The GEOS-5 data assimilation system – Documentation of versions 5.0.1 and 5.1.0. Technical Report Series on Global Modeling and Data Assimilation NASA/TM-2007-104606, NASA Goddard Space Flight Center. Pp. 92, online documentation at http://gmao.gsfc.nasa.gov/systems/geos5/.

Ringler, T. D., 2011: Momentum, Vorticity and Transport: Considerations in the Design of a Finite-Volume Dynamical Core. *Numerical Techniques for Global Atmospheric Models*, P. H. Lauritzen, C. Jablonowski, M. A. Taylor, and R. D. Nair, Eds., Springer, Lecture Notes in Science and Engineering, Vol. 80, 143–183.

Roberts, P. H., 1967: Convection in horizontal layers with internal heat generation. theory. *Journal of Fluid Mechanics*, **30**, 33–49.

Roche, P.-E., F. Gauthier, R. Kaiser, and J. Salort, 2010: On the triggering of the ultimate regime of convection. *New Journal of Physics*, **12**, 085 014 (26pp).

Rood, R. B., 1987: Numerical advection algorithms and their role in atmospheric transport and chemistry models. *Review of Geophysics*, **25**.

Rood, R. B., 2011: A perspective on the role of the dynamical core in the development of weather and climate models. *Numerical Techniques for Global Atmospheric Models*, P. H. Lauritzen, C. Jablonowski, M. A. Taylor, and R. D. Nair, Eds., Springer, Lecture Notes in Science and Engineering, Vol. 80, 523–544.

Sadourny, R., 1972: Conservative finite-difference approximations of the primitive equations on quasi-uniform spherical grids. *Monthly Weather Review*, **100**, 136–144.

Sadourny, R., 1975: The dynamics of finite-difference models of the shallow-water equations. *Journal of Atmospheric Science*, **32**, 680–689.

Sadourny, R., A. Arakawa, and Y. Mintz, 1968: Integration of the nondivergent barotropic vorticity equation with an icosahedral-hexagonal grid for the sphere. *Monthly Weather Review*, **96**, 351–356.

Salmon, R., 1998: *Lectures on Geophysical Fluid Dynamics*. Oxford University Press, 378 pages.

Shepherd, T. G., K. Semeniuk, and J. N. Koshyk, 1996: Sponge layer feedbacks in middle-atmosphere models. *Journal of Geophysical Research*, **101**, 23 447–23 464, doi: 10.1029/96JD01994.

Skamarock, W. C., 2004: Evaluating mesoscale NWP models using kinetic energy spectra. *Monthly Weather Review*, **132**, 3019–3032.

Skamarock, W. C., 2008: A linear analysis of the NCAR CCSM finite-volume dynamical core. *Monthly Weather Review*, **136 (6)**, 2112–2119.

Sotin, C. and S. Labrosse, 1999: Three-dimensional thermal convection in an iso-viscous, infinite Prandtl number fluid heated from within and from below: applications to the transfer of heat through planetary mantles. *Physics of Earth and Planetary Interiors*, **112**, 171–190.

Sparrow, E. M., R. J. Goldstein, and V. K. Jonsson, 1963: Thermal instability in a horizontal fluid layer: effect of boundary conditions and non-linear temperature profiles. *Journal of Fluid Mechanics*, **18**, 513–528.

Spiegel, E. A., 1971: Convection in stars. 1. Basic Boussinesq convection. *Annual Review of Astronomy and Astrophysics*, **9**, 323–352.

Takahashi, Y. O., K. Hamilton, and W. Ohfuchi, 2006: Explicit global simulation of the mesoscale spectrum of atmospheric motions. *Geophysical Research Letters*, **33**, L12 812.

Taylor, M. A., 2011: Conservation of Mass and Energy for the Moist Atmospheric Primitive Equations on Unstructured Grids. *Numerical Techniques for Global Atmospheric Models*, P. H. Lauritzen, C. Jablonowski, M. A. Taylor, and R. D. Nair, Eds., Springer, Lecture Notes in Science and Engineering, Vol. 80, 357–380.

Taylor, M. A., J. Edwards, S. Thomas, and R. D. Nair, 2007: A mass and energy conserving spectral element atmospheric dynamical core on the cubed-sphere grid. *Journal of Physics: Conference Series*, **78 (012074)**.

Taylor, M. A., J. Tribbia, and M. Iskandarani, 1997: The spectral element method for the shallow water equations on the sphere. *Journal of Computational Physics*, **130**, 92–108.

Thuburn, J., 2011a: Some Basic Dynamics Relevant to the Design of Amospheric Model Dynamical Cores. *Numerical Techniques for Global Atmospheric Models*, P. H. Lauritzen, C. Jablonowski, M. A. Taylor, and R. D. Nair, Eds., Springer, Lecture Notes in Science and Engineering, Vol. 80, 3–27.

Thuburn, J., 2011b: Vertical Discretizations: Some Basic Ideas. *Numerical Techniques for Global Atmospheric Models*, P. H. Lauritzen, C. Jablonowski, M. A. Taylor, and R. D. Nair, Eds., Springer, Lecture Notes in Science and Engineering, Vol. 80, 59–74.

van Leer, B., 1974: Towards the ultimate conservative difference scheme, II. Monotonicity and conservation combined in a second order scheme. *Journal of Computational Physics*, **14**, 361–370.

van Leer, B., 1977: Towards the ultimate conservative difference scheme, III. Upstream centered finite-difference schemes for ideal compressible flow. *Journal of Computational Physics*, **23**, 263–275.

Vatteville, J., P. E. van Keken, A. Limare, and A. Davaille, 2009: Starting laminar plumes: Comparison of laboratory and numerical modeling. *Geochemistry, Geophysics, Geosystems*, **10**.

Vitanov, N. K. and F. H. Busse, 1997: Bounds on the heat transport in a horizontal fluid layer with stress-free boundaries. *Zeitschrift Angewende Mathematische Physik.*, **48**, 310–324.

Wang, X., 2004: Infinite Prandtl number limit of Rayleigh-Bénard convection. *Communications in Pure and Applied Mathematics*, **57**, 1265–1285.

White, A. A., B. J. Hoskins, I. Roulstone, and A. Staniforth, 2005: Consistent approximate models of the global atmosphere: shallow, deep, hydrostatic, quasi-hydrostatic and non-hydrostatic. *Quarterly Journal of the Royal Meteorological Society*, **131**, 2081–2107.

Whitehead, J. P. and C. R. Doering, 2011a: Internal heating driven convection at infinite Prandtl number. *Journal of Mathematical Physics*, **52 (093101)**, 11 pages.

Whitehead, J. P. and C. R. Doering, 2011b: Rigid rigorous bounds on heat transport in a slippery container. *(in submission) Journal of Fluid Mechanics*.

Whitehead, J. P. and C. R. Doering, 2011c: The ultimate regime of two-dimensional Rayleigh-Bénard convection with stress-free boundaries. *Physical Review Letters*, **106**, 244 501,p1–p4.

Whitehead, J. P., C. Jablonowski, J. Kent, and R. B. Rood, 2011a: Potential Vorticity: a diagnostic tool for general circulation models (in preparation). *to submit to Quarterly Journal of the Royal Meteorological Society*.

Whitehead, J. P., C. Jablonowski, R. B. Rood, and P. H. Lauritzen, 2011b: A stability analysis of divergence damping on a latitude-longitude grid. *Monthly Weather Review*, **139 (9)**, 2976–2993.

Williamson, D. L., 1968: Integration of the barotropic vorticity equations on a spherical geodesic grid. *Tellus*, **20**, 642–653.

Williamson, D. L., 2007: The evolution of dynamical cores for global atmospheric models. *Journal of the Meteorological Society of Japan*, **85B**, 241–269.

Williamson, D. L., J. G. Olson, and C. Jablonowski, 2009: Two dynamical core formulation flaws exposed by a baroclinic instability test case. *Monthly Weather Review*, **137**, 790–796.

Wittenberg, R., 2010: Bounds on Rayleigh-Bénard convection with imperfectly conducting plates. *Journal of Fluid Mechanics*, **665**, 158–198.

Zapotocny, T. H., A. J. Lenzen, D. R. Johnson, F. M. Reames, P. A. Poitowicz, and T. K. Schaak, 1996: Joint distributions of potential vorticity and inert trace constituent in CCM2 and UW $\theta - \sigma$ model simulations. *Geophysical Research Letters*, **23 (18)**, 2525–2528.

Zhang, K., H. Wan, B. Wang, and M. Zhang, 2008: Consistency problem with tracer advection in the atmospheric model GAMIL. *Advances in Atmospheric Science*, **25 (2)**.

Ziv, B. and P. Alpert, 1994: Isobaric to isentropic interpolation errors and implication to potential vorticity analysis. *Journal of Applied Meteorology*, **33**, 694–703.